



**Universiteit
Leiden**
The Netherlands

Interference effects with surface plasmons

Kuzmin, N.V.

Citation

Kuzmin, N. V. (2008, January 10). *Interference effects with surface plasmons. Casimir PhD Series*. LION, Quantum Optics Group, Faculty of Science, Leiden University. Retrieved from <https://hdl.handle.net/1887/12551>

Version: Corrected Publisher's Version

License: [Licence agreement concerning inclusion of doctoral thesis in the Institutional Repository of the University of Leiden](#)

Downloaded from: <https://hdl.handle.net/1887/12551>

Note: To cite this publication please use the final published version (if applicable).

**Interference Effects
with
Surface Plasmons**

Nikolay Victorovich Kuzmin

Interference Effects with Surface Plasmons

Proefschrift

ter verkrijging van
de graad van Doctor aan de Universiteit Leiden,
op gezag van Rector Magnificus prof.mr. P.F. van der Heijden,
volgens besluit van het College voor Promoties
te verdedigen op donderdag 10 januari 2008
klokke 15:00 uur

door

Nikolay Victorovich Kuzmin

geboren te Troitsk, Rusland
in 1980

Promotiecommissie:

Promotor:	Prof. Dr. G.W. 't Hooft	(Philips Research / Universiteit Leiden)
Copromotor:	Dr. E.R. Eliel	(Universiteit Leiden)
Referent:	Dr. J. Gómez Rivas	(AMOLF / Philips Research)
Leden:	Prof. Dr. L. Kuipers	(AMOLF / Universiteit Twente)
	Prof. Dr. H.P. Urbach	(Technische Universiteit Delft)
	Prof. Dr. M.W. Beijersbergen	(Cosine / Universiteit Leiden)
	Dr. M.P. van Exter	(Universiteit Leiden)
	Prof. Dr. J.P. Woerdman	(Universiteit Leiden)
	Prof. Dr. J.M. van Ruitenbeek	(Universiteit Leiden)

The work presented in this thesis is part of the scientific program of the “Stichting voor Fundamenteel Onderzoek der Materie (FOM)” and has been made possible by financial support from the “Nederlandse Organisatie voor Wetenschappelijk Onderzoek (NWO)”.

Casimir PhD Series, Delft-Leiden, 2008-01
ISBN/EAN: 978-90-9022593-7

Моим родителям и моей сестре
Aan mijn ouders en mijn zuster

Contents

1	Introduction	1
1.1	Basic properties of metals	1
1.2	Surface plasmons	2
1.2.1	What is a surface plasmon?	2
1.2.2	Surface plasmon dispersion and attenuation	5
1.2.3	Surface-plasmon excitation	6
1.3	Outline of thesis	9
2	Plasmon-assisted two-slit transmission: Young's experiment revisited	13
2.1	Introduction	14
2.2	Idea	14
2.3	Experiment	14
2.4	Results	15
2.5	Theoretical calculation	19
2.6	Conclusions	21
2.7	Appendix: Erasing the interference	22
3	Enhanced spatial coherence by surface plasmons	27
3.1	Introduction	28
3.2	Experiment	29
3.3	Results	29
3.4	Conclusions	33

4	Bouncing surface plasmons	35
4.1	Introduction	36
4.2	Experiment	37
4.3	Results	39
4.4	Discussion	41
4.5	Conclusions	47
4.6	Appendix: Slowed-down surface plasmons	48
5	Phase factors in light-plasmon scattering	51
5.1	Introduction	52
5.2	Heuristic models	54
5.2.1	Two-slit system	55
5.2.2	Three-slit system	55
5.3	Experimental setup	58
5.4	Results and Discussion	59
5.4.1	Signal modulation along the slanted slit	60
5.4.2	Coupling phase slip	62
5.4.3	Plasmon tunneling	64
5.4.4	Slanted slit as a source of surface plasmons	65
5.5	Conclusions	67
5.6	Appendix: Towards a complete picture of surface-plasmon scattering	68
6	Retardation effects in sub-wavelength slits in thin metal films near cut-off	73
6.1	Introduction	74
6.2	Experiment	77
6.3	Experimental results	78
6.3.1	Transmission of purely TE/TM polarized incident light.	79
6.3.2	Polarization analysis of transmitted light	80
6.4	Discussion	83
6.5	Conclusions	87
7	Short-wavelength surface plasmons	89
7.1	Introduction	90
7.2	Dispersion and Damping	90
7.3	Experiment	91
7.4	Results and Discussion	93
7.5	Conclusions	98

Bibliography	99
Samenvatting	109
Интерференционные эффекты с поверхностными плазмонами (in Russian)	117
Волны в природе	117
Поверхностные плазмоны	118
Тема и содержание диссертации	122
Curriculum Vitae	135
Acknowledgements	137
List of publications	139

CHAPTER 1

Introduction

1.1 Basic properties of metals

Since ancient times people have been intrigued by the sparkling properties of crystals and the shimmering of shiny metals like gold and silver. These precious metals were valued by many cultures and used as coinage, for ornaments and jewelry.

Polished silver surfaces were also used as mirrors and legend has it that, during the second Punic war, Archimedes used a large number of mirrors to set afire a hostile Roman fleet anchored off the bay of Syracuse, by focusing the light of the sun on the ships [1, 2]. Gold was also used to make stained glass, well known from the windows of many cathedrals around Europe and, much earlier, to make the base glass of the well-known Lycurgus cup [3]. An understanding of the physics of these phenomena came much later, in the 19th and 20th centuries, when scientists came up with a theoretical description of the optics of metals.

In one of these models, the so-called free-electron model, a metal is described as a collection of ions, that are fixed in space, and a gas of free conduction electrons that interact with themselves and with the ions through the Coulomb force [4, 5]. The interacting system of ions and electrons is basically a plasma where the ions have much larger inertia than the electrons. When this plasma interacts with an electromagnetic field, the electrons will execute a forced oscillation relative to the ions. The amplitude and phase of this oscillation relative to that of the driving electromagnetic field depends on the frequency of the latter relative to the eigen oscillation frequency of the plasma, the so-called *plasma frequency* ω_p :

$$\omega_p^2 = \frac{ne^2}{\epsilon_0 m^*}, \quad (1.1)$$

which follows directly from a simple harmonic oscillator description of the response of the electrons [4]. Here n is the electron density, e and m^* are the charge and effective mass of the electron. The quantum of this oscillation is called a *plasmon*, or, since the electrons are oscillating in the metal volume, a *bulk plasmon*. For gold and silver $\omega_p \sim 10^{16}$ rad/s.

The plasma oscillation is damped, for instance, due to the scattering of the electrons off impurities, lattice defects, etc. Phenomenologically, this is taken into account by introducing a damping constant γ , and in the Drude model [4] the relative dielectric function is expressed as:

$$\tilde{\epsilon}(\omega) = 1 - \frac{\omega_p^2}{\omega(\omega + i\gamma)}. \quad (1.2)$$

Here γ represents the collision rate of the electrons and determines the damping of the plasma oscillation. The Drude model is a simple and convenient model that explains, for instance, the high reflectivity of metals in the visible and infrared, i.e. below the plasma frequency. In that spectral regime the real part of the dielectric function is negative $\epsilon'(\omega) \equiv \text{Re}(\tilde{\epsilon}) < 0$ and the incident electromagnetic radiation is back reflected by the plasma, penetrating into the metal only over a distance of the order of $\lambda/2\pi\sqrt{|\epsilon'_m|}$, which is $\simeq 25$ nm for case of gold at $\lambda = 0.8 \mu\text{m}$. In the UV range, i.e., above the plasma frequency, $\epsilon'(\omega)$ is positive and the metal is transparent for incident electromagnetic radiation.

1.2 Surface plasmons

In 1957 Ritchie theoretically showed [6] that, when a metal is in the form of a thin foil, a second type of plasma resonance can occur at $\omega = \omega_p/\sqrt{2}$. Here the charge oscillations take place at the top and bottom interfaces of the metal film. This prediction was confirmed in an experiment by Powell and Swan [7].

1.2.1 What is a surface plasmon?

This collective oscillation of the electron gas on the interface between a metal and a dielectric has become known as the *surface plasmon* (SP). Theoretically, surface plasmons simply arise as a purely 2D solution of Maxwell's equations that propagates as a transverse magnetic wave along the metallo-dielectric interface [8]. This wave is evanescent in both the dielectric and the metal. This characteristic nature of the surface plasmon follows from the requirement that the interface is “active”, i.e., that the real parts of the dielectric functions $\epsilon'(\omega)$ of the media on either side of the interface have opposite signs.

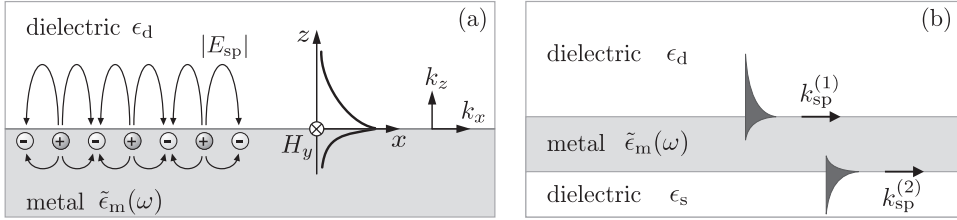


Figure 1.1. (a) Schematic picture of the charge distribution of a surface plasmon and the associated electromagnetic wave. (b) Metal film, sandwiched between two dielectrics, carrying surface plasmons at each interface. When the metal film is thin ($\lesssim 50$ nm) the plasmons of both interfaces can couple via their evanescent fields.

In the recent literature [9] a distinction is made between surface plasmons, that *propagate* on essentially extended interfaces (length scale much larger than the optical wavelength), called *surface-plasmon polaritons*, and *localized* surface plasmons which are associated with metal objects or protrusions that are much smaller than the wavelength [10, 11]. The latter are referred to as “particle plasmons” and are responsible, e.g., for the optical properties of the Lycurgus cup mentioned earlier.

The boundary conditions for the electromagnetic field require that the magnetic field of a surface plasmon, propagating along a smooth and flat interface, is parallel to the metal surface. With the SP, propagating in the x -direction as a transverse magnetic wave, we have $H_x = H_z = 0$. The propagation constant of the SP is complex:

$$\tilde{k}_x \equiv k_{\text{sp}} + ik'_x = \frac{\omega}{c} \sqrt{\frac{\tilde{\epsilon}_m \epsilon_d}{\tilde{\epsilon}_m + \epsilon_d}}, \quad (1.3)$$

with $\tilde{\epsilon}_m$ and ϵ_d the dielectric functions of the metal and of the dielectric, respectively. Note that $\tilde{\epsilon}_m$ is complex: $\tilde{\epsilon}_m = \epsilon'_m + i\epsilon''_m$ with $\epsilon'_m < 0$.

The magnetic component of the surface-plasmon field can be written as

$$\vec{H}_{\text{sp}} = \hat{y} H_y f(z) \exp[i(\tilde{k}_x x - \omega t)], \quad (1.4)$$

with

$$f(z) = \begin{cases} \exp(-q_d z) & \text{for } z > 0, \\ \exp(+q_m z) & \text{for } z < 0, \end{cases} \quad (1.5)$$

where $\tilde{k}_x^2 - q_i^2 = \epsilon_i(\omega/c)^2$, $i = \text{m, d}$. In the limit that $|\epsilon'_m| \gg \epsilon_d$ one has

$$\begin{aligned} q_d &\simeq \frac{\omega}{c} \frac{\epsilon_d}{\sqrt{|\epsilon'_m|}}, \\ q_m &\simeq \frac{\omega}{c} \sqrt{|\epsilon'_m|}, \end{aligned} \tag{1.6}$$

showing that the surface plasmon field decays in the z -direction over a length roughly equal to $\lambda\sqrt{|\epsilon'_m|}/2\pi\epsilon_d$ in the dielectric and $\lambda/2\pi\sqrt{|\epsilon'_m|}$ in the metal. For large values of $|\epsilon'_m|$ the field extends well into the dielectric (microns) and only marginally into the metal (nanometers). The fact that the electromagnetic field of a surface plasmon is confined to the metallo-dielectric interface makes SP into a highly sensitive probe of such interfaces [12, 13].

The electric field of the surface plasmon has both a longitudinal (x) and transverse (z) components with ratio

$$\begin{aligned} \frac{E_x}{E_z} &= -i \frac{q_d}{k_{\text{sp}}} \quad \text{for } z > 0, \\ \frac{E_x}{E_z} &= +i \frac{q_m}{k_{\text{sp}}} \quad \text{for } z < 0, \end{aligned} \tag{1.7}$$

so that fields in both media are ‘‘elliptically’’ polarized.

An important property of the surface plasmon is that it is attenuated during propagation, basically due to dissipation in the metal — the electrons are inelastically scattered. The field attenuation length, i.e. the length over which the SP field amplitude decays by factor e in the x direction, is given by $L_{\text{sp}} = 1/k_x''$. For gold and silver L_{sp} spans from millimeters in the mid-infrared range to less than a micron in the blue part of the visible spectrum (see Fig. 1.3b). A second cause of surface plasmon damping is surface roughness [8, 14].

When the metal does not form a half space, but is shaped as a thin film on top of a dielectric, surface plasmons can propagate along both interfaces of that film (see Fig.1.1b), and, if the film is sufficiently thin, i.e., $\lesssim 50$ nm, these SPs can couple [15]. For a symmetrically-embedded metal film the interaction between the evanescent SP fields in the metal gives rise to symmetric and asymmetric modes, which have very different attenuation lengths [16]. The asymmetric mode can propagate for a much longer distance than its symmetric counterpart, and its propagation length is considerably larger than that of a plasmon on a semi-infinite interface. The SPs with long propagation length are called *long-range surface plasmons* [17]. In the present thesis, however, the focus is on surface plasmons propagating along a *single* interface.

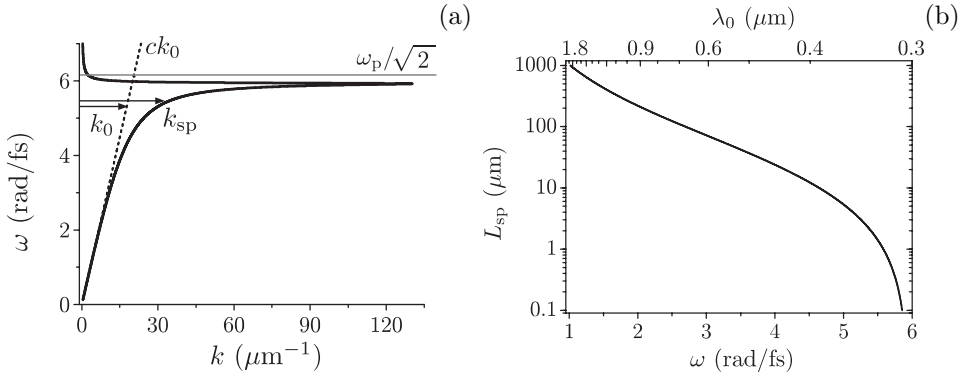


Figure 1.2. (a) Dispersion of the surface plasmon on the sodium-vacuum interface (solid black line). The dashed line shows the light line ($\omega = ck_0$). Arrows show that the SP wavenumber k_{sp} exceeds the free radiation wavenumber k_0 . (b) Surface plasmon propagation length L_{sp} on the sodium-air interface.

1.2.2 Surface plasmon dispersion and attenuation

The dispersion of the surface plasmon, i.e., the dependence of the SP frequency ω on its wave number k_{sp} shows how the properties of the surface plasmon change in various frequency ranges, and determines the value of both the phase and group velocities. To gain a conceptual understanding of the dispersive properties of a surface plasmon we return to the Drude model (see Eq.(1.2)) for the dielectric function of the metal, and assume the dielectric to be dispersionless. Metallic sodium behaves very much like a Drude metal, i.e., the dispersion of its dielectric function can accurately be fitted with the Drude model yielding $\omega_p = 8.7$ rad/fs and $\gamma = 0.042$ fs $^{-1}$ [18]. The results for the SP dispersion and the damping on the sodium-vacuum interface are shown in Fig. 1.2.

At low frequencies (near IR and IR, $\omega < 2$ rad/fs) the SP on the Na-vacuum interface has a photon-like nature, i.e., its phase velocity is very close to the speed of light: it extends mainly in the vacuum rather than in the metal. At optical frequencies the dispersion curve $\omega(k_{\text{sp}})$ starts to bend over, which results in a decrease of the SP group velocity $v_{\text{gr}} = \partial\omega/\partial k_{\text{sp}}$ and higher damping due to deeper penetration of the SP into the metal. In the limit that $\omega \rightarrow \omega_p/\sqrt{2}$ the SP becomes a localized excitation, since $v_{\text{gr}} \rightarrow 0$. At the largest value of k_{sp} ($k_{\text{sp}} \sim 130$ μm^{-1}) the dispersion curve is seen to fold back. Along this branch the group velocity is negative, a notion that has spawned quite a few papers [19–21]. In this spectral region the SP is, however, so

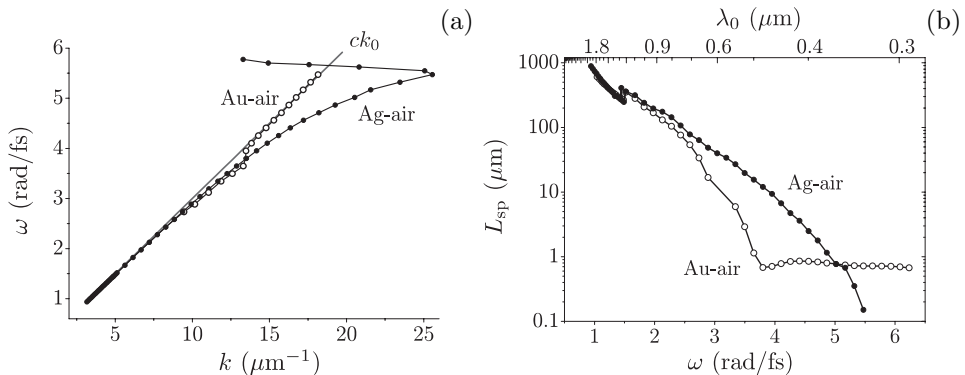


Figure 1.3. The dispersion (a) and damping (b) of a surface plasmon on gold-air (○) and silver-air (●) interfaces. Data are based on tabulated values for the dielectric functions of metals [22].

strongly damped that the concept of a propagating wave loses its meaning.

Figure 1.2b shows how the attenuation length L_{sp} varies as a function of the frequency of the surface plasmon. While for frequencies $\omega < 4.7$ rad/fs the relationship between L_{sp} and ω is almost exponential, for higher frequencies L_{sp} drops even much more rapidly.

In most practical cases it is convenient to use metals that are less reactive than sodium, e.g. gold or silver. The dispersion and damping of a surface plasmon on a gold-air or silver-air interfaces are shown in Fig. 1.3. Clearly, silver behaves much better than gold insofar that the wavenumber of the surface plasmon on the silver-air interface deviates much more from the light line than on the gold-air interface. Additionally silver shows a lower SP attenuation compared to gold. However, gold doesn't oxidize in air, which makes it easy to study surface plasmons on the gold-air interface while thin silver layers are prone to chemical attack in air [23]. Note that it is still possible to study SPs on the silver-dielectric interface when the silver layer is buried or freshly applied.

1.2.3 Surface-plasmon excitation

The value of the SP wave number k_{sp} is larger than that of light in free space k_0 (see Fig. 1.2a). Consequently, there is a wave-vector mismatch between the surface plasmon and free-space radiation, and it is therefore not possible to directly excite the SP by shining light on a smooth metal surface [8]. Various schemes have been used [24] to add the missing momentum to the incident photon (see Fig. 1.4). Prism coupling schemes, shown in Fig. 1.4a–c, as pro-

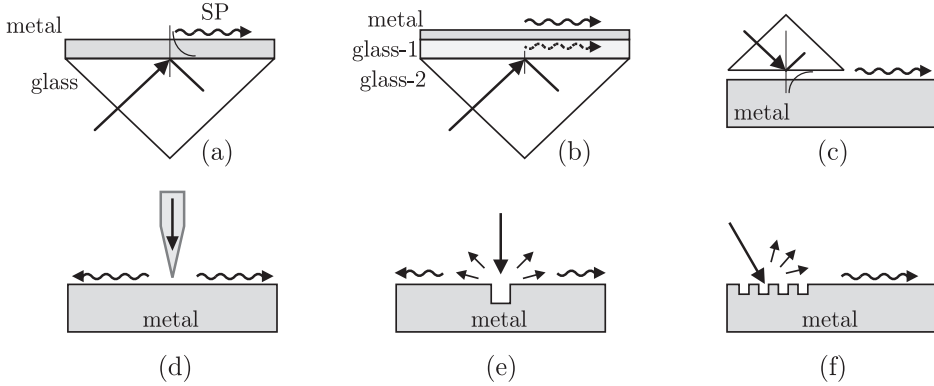


Figure 1.4. Surface-plasmon excitation schemes: a) Kretschmann configuration; b) double-layer Kretschmann configuration; c) Otto configuration; d) excitation with a SNOM probe; e) light diffraction on a single surface feature; f) excitation by means of a diffraction grating.

posed by Kretschmann and Otto [25, 26], are still widely used, especially in surface-plasmon spectroscopy [27, 28]. These schemes require careful angular tuning of the setup to couple to the surface plasmons. A scanning near-field optical microscope (SNOM) tip (Fig. 1.4d) is also a widely used powerful tool for both local excitation and probing of the surface plasmons [29–33]. Finally, a surface feature like a protrusion, grating, or surface roughness can be employed to excite and de-excite SPs (Fig. 1.4e–f). In all cases the polarization of the incident radiation has to be chosen so as to optimally couple with a surface plasmon. In the present thesis, where we use one, two or three slits to launch and detect surface plasmons, the incident light has to be polarized perpendicular to the slit axis.

Obviously, the detailed shape of the surface feature has a major impact on the excitation probability of a surface plasmon. Naively, one can say that for normally incident light the excitation probability is determined by the square of the Fourier transform of the surface feature at the wave vector of the surface plasmon. For a rectangular bump of width a the Fourier spectrum is shown in Fig. 1.5. It is seen to rapidly drop off and to become zero when $k = 2\pi/a$. This suggests that, in order to efficiently excite surface plasmons one should have $k_{\text{sp}} \ll 2\pi/a$, i.e. $a \ll \lambda$. In that case the SP excitation probability only weakly depends on λ .

In the work described in this thesis sub-wavelength slits are employed as both source and probe of surface plasmons [34, 35], the main reason being the simplicity of the structure and the intuitiveness of the physics. As an example,

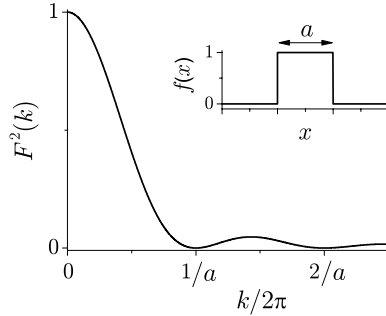


Figure 1.5. Fourier spectrum of a step function.

one of the studied structures is shown in Fig. 1.6 together with the light pattern behind it, observed under two illumination conditions. The sample is a 200 nm thick gold film, deposited on top of 0.5 mm thick glass plate with a 10 nm Ti adhesion layer between the gold and the glass. The gold film is perforated by two parallel, 0.2 μm wide and 50 μm long slits, that are 25 μm apart. One of the two slits is illuminated by a tightly focused laser beam with a spot size of order 5 μm , much smaller than the slit separation. The laser is tuned to a wavelength of 800 nm where the SP on the Au-air interface is weakly damped ($L_{\text{sp}} \simeq 90 \mu\text{m}$). The polarization of light can be chosen to be either TE or TM, i.e. parallel or perpendicular to the length of the slits. The dark side of the sample is imaged on a CCD camera by means of a microscope objective (40/0.65). Figures 1.6b and c show the case for TE and TM illumination, respectively. Under TM illumination the non-illuminated slit is bright being “fed” by the SP launched by the illuminated slit at left.

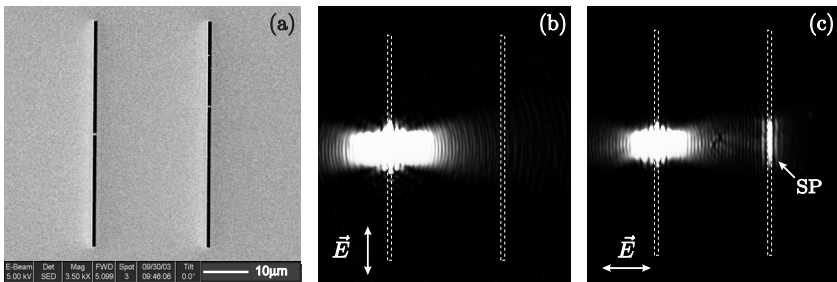


Figure 1.6. (a) SEM image of the sample; (b) Source slit is illuminated with TE polarized light and probe slit remains dark as surface plasmons are not excited; (c) Source slit is illuminated with TM polarized light and probe slit becomes bright, scattering the incident SP to propagating light. The positions of the slits are indicated by dashed lines.

1.3 Outline of thesis

The work in this thesis describes a series of interlinked experiments on surface plasmons propagating along a metallo-dielectric interface. The metal is either gold or silver applied as a thin (≈ 200 nm thick) film on top of a transparent substrate with a binding layer in between. That film is perforated by a number of long, sub-wavelength slits, separated by many optical wavelengths (see Fig. 1.6). The common idea behind all the experiments is that each of the slits has a number of functions:

1. It transmits part of the incident light.
2. It scatters part of the incident light into a surface plasmon that propagates along the interface.
3. It scatters part of an incident surface plasmon into light, being visible at both the front and rear sides of the sample.

This list is not complete; however, it enumerates the effects that dominate the experimental results described in this thesis.

In the second Chapter we study a sample consisting of a 200 nm thick gold film on top of a glass substrate with a titanium adhesion layer between the gold and the glass. The metal film is perforated by a series of double slits, each of the slits being $\approx 50 \mu\text{m}$ long and 200 nm wide. There are five sets of double slits, each with a different inter-slit distance, namely 5, 10, 15, 20 and 25 μm . When illuminated by a spatially coherent, narrow-band source, each slit pair will give rise to the well-known double-slit interference pattern, described in any textbook on optics or wave phenomena. Here we do not study this well-known interference phenomenon; instead we look at the *total* amount of light transmitted by the double slit. We vary the wavelength of the incident light and observe a periodic modulation of the transmitted power, the modulation period being inversely proportional to the slit separation. The visibility of this interference phenomenon is strongly affected by the slit width so that the effect is most pronounced when very narrow slits are used. We attribute this modulation to an interference effect, namely between light directly transmitted by one of the slits and light that transiently traveled as a surface plasmon, having been launched by the other slit. The slits experience cross talk due to the surface plasmons.

We have included some experiments on a 200 nm thick titanium film, a material that exhibits extremely strong surface-plasmon damping. This sample does not exhibit any spectral modulation of the transmittivity, in line with our description in terms of surface-plasmon cross talk. Similarly, the

spectral modulation is also not observed if the incident light is TE-polarized, i.e., is polarized parallel to the slits.

In Chapter 3 we use the same configuration as in Chapter 2 but we focus the incident radiation on just *one* slit. When looking at the unilluminated side of the sample one observes that *both* slits transmit light, one much stronger than the other (the non-irradiated slit). In this second system exhibiting plasmonic cross talk we study the nature of the far-field interference pattern, specifically how the interference orders move when the wavelength of the incident radiation is changed. In a second experiment, we illuminate both slits, the light incident on slit 1 being totally incoherent with the light incident on slit 2. Nevertheless, the far field behind the double slit shows clear interference features indicating that the light exiting the slit is in part *coherent*. Here the cross-coupling due to the surface plasmons acts as a source of coherence.

The spectral fringes that one observes in the experiment described in Chapter 2 are slightly non-sinusoidal, indicating that the effect is possibly more than a two-beam interference effect. That suggests a picture of a resonator, with the surface plasmon bouncing between mirrors, in our case the slits. In Chapter 4 we explore this picture of a bouncing surface plasmon using a time-domain approach. In this Chapter we use pairs of slits separated by 25, 50, 75 or 90 μm . We are able to observe the surface plasmon making two full round trips through the cavity. This experiment allows us to determine the surface-plasmon power reflection coefficient, obtain information on the phase shift in various scattering processes, and directly measure the surface-plasmon group velocity at the wavelength of the incident radiation.

In Chapter 5 we use a sample containing not two but three slits, two of which are parallel, the third one intersecting the other two at a rather acute angle. The surface plasmons now give rise to an intricate interference pattern in each of the slits unless the polarization of the incident radiation is chosen so that a specific slit does not directly transmit the incident light or does not launch surface plasmons. By judiciously selecting the polarization of the incident light and the dimensions of the sample we are able to observe the standing surface-plasmon wave launched by the two parallel slits. By comparing the light transmitted by various parts of the structure we are able to obtain information on the scattering phase acquired when light is scattered into a plasmon an back-scattered into light, and on the amplitude and phase acquired by the surface plasmon as it “transits” a sub-wavelength slit.

The experimental study of the structures studied in Chapters 2 and 3 brought to light that our sub-wavelength slits milled through our thin metal layers are much less polarization selective (in terms of their direct transmis-

sion) than one would naively think. Moreover, when the incident light is linearly polarized at an angle of 45° relative to the slit the transmitted light is circularly polarized, indicating that such a slit is highly birefringent.

However, it is widely assumed that a slit with width $\approx \lambda/4$ has a very much smaller transmission for incident light that is TE-polarized as compared to light that is TM-polarized and our initial results were therefore quite puzzling. In Chapter 6 we investigate this by studying the width dependence of the transmission of a single slit. We compare our experimental data with the results of a numerical calculation and obtain excellent agreement. The strong birefringence of certain slits is explained in terms of the difference in phase evolution between a propagating and an evanescent mode.

In Chapter 7 we apply the spectral modulation method of Chapter 2 to the study of surface-plasmons propagating along a buried interface, namely the silver-glass interface. From a plasmonic point of view, silver is much to be preferred over gold being a much less lossy metal, particularly at higher photon energies (in the blue spectral region). However, silver has a disadvantage in that it rapidly tarnishes in air, requiring the plasmon-supporting interface to be buried. There are two interesting aspects to studying surface plasmons on such a buried interface: the surface-plasmon wavelength $\lambda_{\text{sp}} = 2\pi/k_{\text{sp}}$ is reduced by, roughly, the refractive index of the dielectric n_{d} , and the damping is increased by a factor of order n_{d}^3 . On this sample we are able to observe plasmonic interference up to photon energies of 2.6 eV (vacuum wavelength $\lambda_0 = 477$ nm), corresponding to a plasmonic wavelength of 260 nm, one of the shortest reported values to date.

CHAPTER 2

Plasmon-assisted two-slit transmission: Young's experiment revisited¹

We present an experimental and theoretical study of the optical transmission of a thin metal screen perforated by two sub-wavelength slits, separated by many optical wavelengths. The total intensity of the far-field double-slit pattern is shown to be reduced or enhanced as a function of the wavelength of the incident light beam. This modulation is attributed to an interference phenomenon at each of the slits, instead of at the detector. The interference arises as a consequence of the excitation of surface plasmons propagating from one slit to the other.

¹) H.F. Schouten, N.V. Kuzmin, G. Dubois, T.D. Visser, G. Gbur, P.F.A. Alkemade, H. Blok, G.W.'t Hooft, D. Lenstra, and E.R. Eliel, *Plasmon-assisted two-slit transmission: Young's experiment revisited*, Phys. Rev. Lett. **94**, p. 053901 (2005)

2.1 Introduction

Recently, there has been a surge of interest in the phenomenon of light transmission through sub-wavelength apertures in metal plates. This followed the observation of enhanced transmission through a two-dimensional hole array by Ebbesen *et al.* [36], who found that the transmission of such an array could be much larger than predicted by conventional diffraction theory [37]. This discovery has rekindled the interest in a similar but simpler problem, viz. the transmission of a one-dimensional array of sub-wavelength *slits* in a metal film, i.e., of a metal grating [36, 38–51]. In many cases the enhanced transmission of hole or slit arrays has been explained in terms of the excitation of (coupled) surface plasmons on the metal film [38–40, 42], an explanation that has recently been challenged [51]. It has been shown that, for slit arrays, Fabry-Pérot-type waveguide resonances can also give rise to considerably enhanced transmission [40, 41, 44, 45, 47].

2.2 Idea

In this chapter we study an even more fundamental system than the metallic grating, namely a thin metal layer perforated by just *two* parallel sub-wavelength slits. In contrast to the systems that have recently attracted so much attention, our slits are separated by *many* optical wavelengths. Thus we study the light transmission of a setup that lies at the heart of wave physics, namely that of Thomas Young. We do, however, not focus on the well-known interference pattern named after him, but on the angle-integrated power transmission coefficient of the perforated screen, i.e. the transmission integrated over many interference orders. We show that this transmission coefficient is strongly modulated as a function of the wavelength of the incident light for the case that that light is TM-polarized, i.e., with the electric field aligned perpendicular to the slits. In contrast, there is no such modulation when the incident light is TE-polarized, or when the “wrong” metal is chosen. All our observations can be explained in terms of a model involving the coherent transport of electromagnetic energy between the slits by surface plasmons.

2.3 Experiment

Our samples consist of a 200 nm thick gold film, evaporated on top of a 0.5 mm thick fused-quartz substrate with a 10 nm thick titanium adhesion layer between the gold and the glass. In such a sample a two-slit pattern is

written using a focussed ion beam [52], each slit being $50\ \mu\text{m}$ long and $0.2\ \mu\text{m}$ wide. The centers of the slits are separated by a distance, as measured with a scanning electron microscope, of 4.9, 9.9, 14.8, 19.8 or $24.5\ \mu\text{m}$, respectively. Such a two-slit pattern, with the metallized side facing the laser, is illuminated at normal incidence with the well-collimated output beam ($\approx 2\ \text{mm}$ diameter) of a narrow-band CW Ti:sapphire laser, tunable between 740 and 830 nm. We detect in transmission, integrating the double-slit pattern over a large number of interference orders. The zeroth order peak is considerably stronger than the other orders, presumably as a result of non-negligible leakage through the bulk metal, and is therefore fully blocked by an opaque screen. We choose the polarization of the incident light to be either parallel (TE) or perpendicular (TM) to the long axis of the pair of slits.

2.4 Results

The results for the case of TM-polarization are shown in Fig. 2.1. The transmission is seen to be approximately sinusoidally modulated as a function of wave number, the modulation period being inversely proportional to the slit separation. The visibility of the fringes is of order 0.2, roughly independent of the slit separation. Note that the fringes are superposed on an offset that gradually decreases as a function of wavelength.

When, instead, a TE-polarized beam is used to illuminate the double slit ($24.5\ \mu\text{m}$ slit distance) the detected signal shows no modulation whatsoever (see bottom frame of Fig. 2.1). Equally, no modulation is observed when the experiment is performed using a 200 nm thick titanium layer instead of gold, independent of the polarization of the incident radiation.

The observed strong polarization anisotropy and the dependence on the material of the screen both suggest that surface plasmons propagating along the gold/air interface lie at the heart of the observed phenomena. Alternative explanations in terms of waveguide modes within the slit [40, 41, 44, 45, 47] or diffractive evanescent waves [51] are excluded by the observed *dependence* of the spectral modulation period, and the *independence* of the modulation depth on the slit separation.

The surface plasmons cannot be excited on a smooth interface by the normally incident beam, because of translational invariance. In the present case the slits brake the translational symmetry of the surface and can provide the missing momentum along the interface. Thus, when the incident light is TM-polarized it excites, at each of the slits, a surface plasmon propagating along the interface between the metal and the dielectric. The propagation

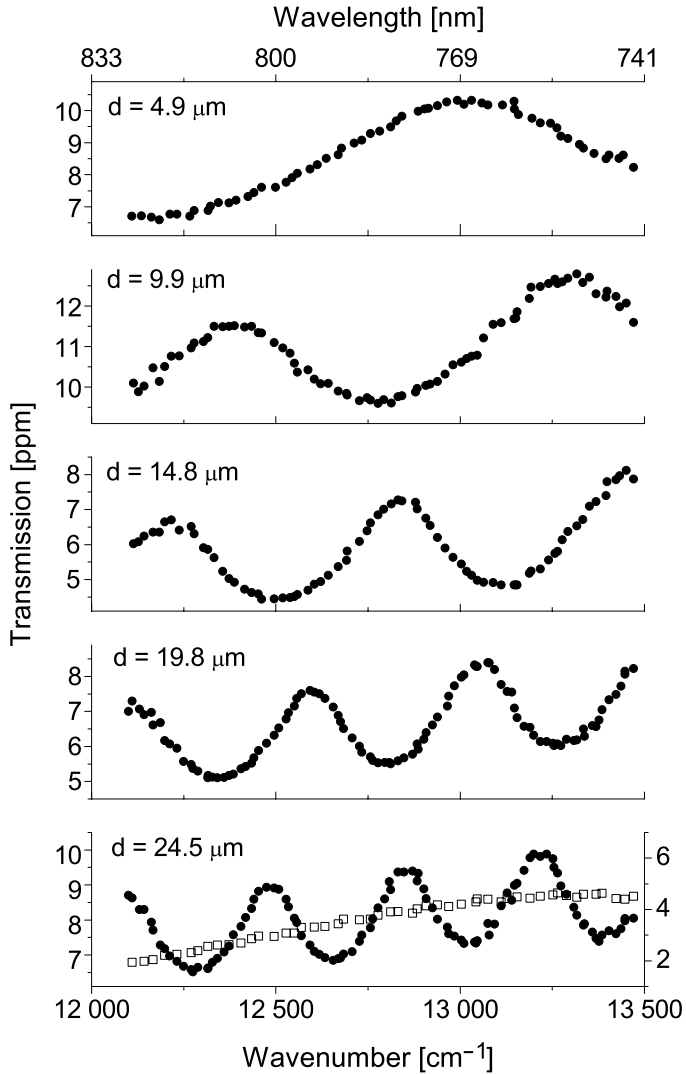


Figure 2.1. Experimental angle-integrated transmission spectra for a TM-polarized input beam (polarization perpendicular to the long axis of the 200 nm wide slits). The value of the slit separation d is indicated in each of the frames. In the frame at the bottom ($d = 24.5 \mu\text{m}$) the results for TE-polarized incident light (open squares) are included; the scale at the right applies to this choice of polarization.



Figure 2.2. Two interfering paths leading to light emission from the leftmost slit. A similar set of paths gives rise to emission from the slit on the right-hand side. The dashed line indicates the propagating surface plasmon.

constant k_{sp} of such a surface plasmon is given by [8]:

$$k_{\text{sp}} = k_0 \sqrt{\frac{\epsilon_m \epsilon_d}{\epsilon_m + \epsilon_d}}, \quad (2.1)$$

where ϵ_m and ϵ_d are the complex (relative) dielectric constants of the metal and dielectric, respectively, and $k_0 = 2\pi/\lambda$ the free-space wave number. The surface-plasmon wavelength is related to the real part of k_{sp} by $\lambda_{\text{sp}} = 2\pi/\text{Re}(k_{\text{sp}}) \equiv \lambda_0/n_{\text{sp}}$, while its (amplitude) decay length is given by $1/\text{Im}(k_{\text{sp}})$. For the gold/air interface at $\lambda_0 = 800$ nm $n_{\text{sp}} = 1.02$ and $1/\text{Im}(k_{\text{sp}}) \approx 80$ μm [53], considerably larger than the separation of the slits. Consequently, surface plasmons propagating along this interface can easily cover the distance between the slits. In contrast, the amplitude decay length for the Ti/air interface at $\lambda_0 = 800$ nm is only ≈ 7 μm [54], considerably shorter than the separation of most of our double slits. Surface plasmons launched on this interface simply do not survive long enough, as is confirmed by our experiments.

Since the gold film is sandwiched between glass ($\epsilon_d \approx 2.1$) and air ($\epsilon_d = 1$), the surface plasmons living on the Au/air and Au/glass interfaces have different (complex) propagation constants (see Eq. (2.1)). Moreover, a 10 nm film of Ti lies between the glass substrate and the gold film, resulting in a much reduced decay length of the surface plasmons on that interface. Consequently, of all the interfaces that we probe in the experiment, only the Au/air variety supports surface plasmons propagating over distances comparable to the separation of the slits.

A surface plasmon on this interface, excited at one of the two slits and traveling towards its partner slit, can scatter there, being converted to free-space radiation. Each propagating surface plasmon therefore generates an additional path for light transmission through the slit (see Fig. 2.2). The plasmon-mediated amplitude at the second slit interferes with the amplitude of the light that is directly transmitted by that slit. Consequently, the field amplitude at the second slit's dark side can be written as

$$E_{\text{slit}}^{(2)} = E_0(\lambda_0)(1 + \alpha(k_{\text{sp}}) \exp[i(k_{\text{sp}}d + \Phi)]), \quad (2.2)$$

where d is the slit separation, $\alpha(k_{\text{sp}})$ the relative strength of the plasmon contribution and Φ a phase factor, assumed to be wavelength-independent. The field amplitude $E_{\text{slit}}^{(2)}$ behind the second slit is thus enhanced or suppressed, depending on the argument of the complex phase factor in Eq. (2.2). Because our laser beam is normally incident on the sample and symmetrically illuminates the two slits, the field amplitude behind the first slit is given by $E_{\text{slit}}^{(1)} = E_{\text{slit}}^{(2)}$.

In the present experiment the far-field two-slit pattern arises as a consequence of the interference of *four* paths, two of which are partially plasmonic, while the other two are photonic all the way. Although the number of interfering channels is four in the present experiment, the far-field pattern that arises behind the sample is simply that of Young's experiment, i.e. a pattern of *two* interfering sources. The novel aspect is that the strength of each of these sources is enhanced or reduced due to the interference of a photonic and a plasmonic channel.

We collect a large number of interference orders on our detector thereby effectively erasing the far-field two-slit pattern. Hence, the signal S picked up by our detector is simply proportional to the total power radiated into the acceptance angle of the detector, i.e., to twice the power radiated by each slit separately,

$$S \propto 2E_0^2(\lambda_0) [1 + \alpha^2(k_{\text{sp}}) + 2\alpha(k_{\text{sp}}) \cos(k_{\text{sp}}d + \Phi)]. \quad (2.3)$$

From the experiment we estimate that, across the wavelength range probed, the parameter $\alpha(k_{\text{sp}}) \approx 0.1$ and is independent of the wavelength of the incident radiation. Further, in order to reliably fit our experimental transmission spectra with the expression given by Eq. (2.3) and the measured values for the slit separation we need to take the dispersion of the surface plasmon's propagation constant into account. This provides additional support for our claim that the effect observed here is to be attributed to communication between the slits by propagating surface plasmons.

Surface plasmons can also be excited when the incident light is TE-polarized, in this case at the sub- μm top and bottom edges of the $50 \mu\text{m}$ long slits. These surface excitations do not effectively couple to the other slit, being predominantly emitted in the wrong direction. In the absence of plasmon-mediated inter-slit coupling the angular-integrated double-slit spectrum is expected to be smooth, and this is in line with our experimental findings (see Fig. 2.1).

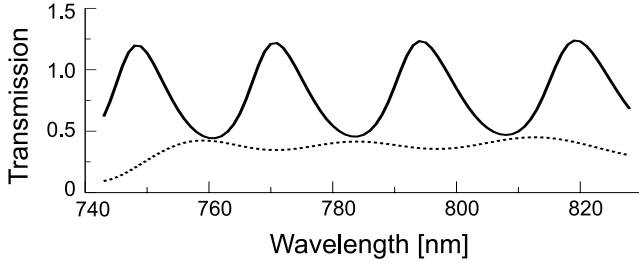


Figure 2.3. The calculated transmission coefficient T of a double slit in a 200 nm thick gold film as a function of the wavelength of the incident light. The slits are 200 nm wide and separated by 25.0 μm . The full line displays the results for TM polarization, while the dotted line (magnified 10 times) shows the results for the case of TE polarization. The transmission coefficient is normalized to the area of the slits.

Note that for this polarization the incident light is beyond cut-off for each slit separately.

2.5 Theoretical calculation

Theoretically, we calculate the transmission of the double-slit system using a rigorous scattering model based on a Green's function approach. We write the total electric field, \mathbf{E} , as the sum of the incident field, $\mathbf{E}^{(\text{inc})}$, taken to be monochromatic and propagating perpendicular to the plate, and the scattered field, $\mathbf{E}^{(\text{sca})}$. The former is the solution of the scattering problem (including multiple reflections) in the absence of the slits, while the latter is the field due to their presence. The total electric field can be written as [55, 56]

$$\mathbf{E} = \mathbf{E}^{(\text{inc})} - i\omega\Delta\epsilon \int_{\text{slits}} \mathbf{G} \cdot \mathbf{E} d^2r, \quad (2.4)$$

where $\Delta\epsilon = \epsilon_0 - \epsilon_m$ is the difference in permittivity of the slits (vacuum) and the metal plate, and \mathbf{G} is the electric Green's tensor pertaining to the plate without the slits. We have suppressed the time-dependent part of the field given by $\exp(-i\omega t)$, where ω denotes the angular frequency. Note that, for simplicity, we here assume that the metal film is embedded in air on both sides. For points within the slit Eq. (2.3) is a Fredholm equation of the second kind for \mathbf{E} , which is solved numerically by the collocation method with piecewise-constant basis functions [57]. To quantify the transmission process, a normalized transmission coefficient is used, where the geometrical optical transmission through the two slits is taken as the normalization factor [56].

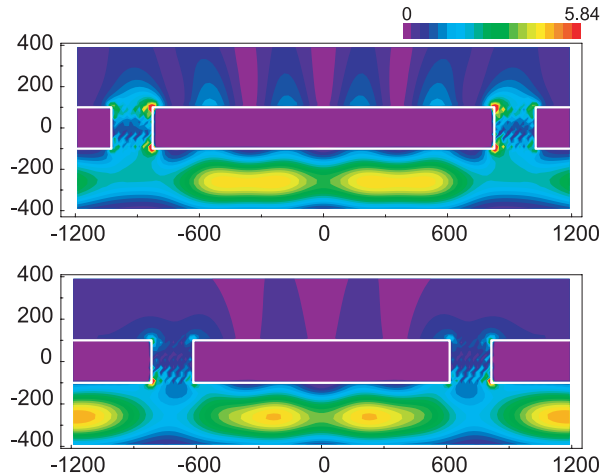


Figure 2.4. Intensity distribution in the immediate vicinity of the double-slit system for TM-polarized incident radiation when the transmission is maximum (top frame, slit separation equal to $5\lambda_{\text{sp}}/2$), and minimum (bottom frame, slit separation equal to $4\lambda_{\text{sp}}/2$). The field is incident from below. All lengths are in nm.

The wavelength dependence of the dielectric constant of the gold film is fully taken into account [53].

In Fig. 2.3 the total transmission of the two-slit configuration is shown as a function of the wavelength of the incident radiation. When the incident field is TE polarized, the transmission of the double slit is small and weakly modulated as a function of wavelength. In contrast, for a TM-polarized incident field, the transmission shows a strong modulation as a function of wavelength with a visibility $\mathcal{V} \approx 0.45$. Overall the agreement between the experiment and the results of the Green's function model is seen to be good, the theoretical data having a somewhat larger visibility than the experimental ones ($\mathcal{V} \approx 0.2$). This difference can be attributed to the different embedding of the gold film in the experiment and in the calculation. While in the experiment the gold film is asymmetrically encapsulated, in the calculation the materials at either side of the film are identical, greatly enhancing the plasmonic effects.

Using the theoretical model outlined above we have also calculated the intensity distribution, i.e. the value of $|E|^2$, on both sides of a free-standing perforated gold film (see Fig. 2.4). For calculational convenience we have taken values of the slit separation that are considerably smaller than those of the experiment, viz. $5\lambda_{\text{sp}}/2$, where the transmission is maximum, and $4\lambda_{\text{sp}}/2$, where the transmission is minimum. In the first case (maximum transmission)

one can distinguish at the dark side of the metal film a well-developed standing wave pattern along the interface, having six antinodes, two of which coincide with the slits themselves. In contrast, when the transmission is minimum the antinodes of the standing-wave pattern do not coincide with the slits; at these locations one rather finds a node of the standing-wave pattern. In both cases the intensity is seen to rapidly decay away from the air-metal interface.

2.6 Conclusions

In this Chapter we have shown that Young's double slit experiment, often seen as proof of the wave nature of light, can provide powerful evidence for the role of propagating surface plasmons in the transmission of perforated metal screens. The transport of electromagnetic energy by the surface plasmons over distances of many optical wavelengths gives rise to an interference phenomenon in the slits that enhances or reduces the intensity of the far-field pattern.

2.7 Appendix: Erasing the interference (unpublished)

In Chapter 2 we studied the transmission spectrum of a metallic film containing two close-lying sub-wavelength wide slits at normal incidence. The observed spectral modulation is explained in terms of plasmonic cross-talk, i.e., a coherent energy transport from one slit to the other by means of surface plasmons. Due to this process a fraction of the light incident on slit A emerges from slit B where it interferes with a fraction of the light incident on that same slit. This interference effect takes place in both slits and at normal incidence the relative phases of the two interfering channels in the two slits $\Delta\phi_A$ and $\Delta\phi_B$ are equal.

Here we study the transmission spectrum of such a double slit at non-normal incidence.

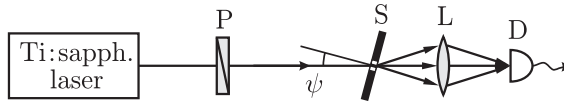


Figure 2.5. Experimental setup for measuring the transmission spectrum of a double slit.

The experimental arrangement is shown in Fig. 2.5. The TM-polarized collimated output beam from a wavelength-tunable Ti-sapphire laser ($743 < \lambda < 827$ nm) is incident on our sample at near-normal incidence, with a beam diameter of ≈ 2 mm. The transmitted light is collected and imaged on a Si-photodetector. We scan the wavelength of the laser and measure the photodetector signal. The latter is normalized by means of the signal from a second photodetector that monitors the laser output power. Our sample consists of a 200 nm thick gold film on top of a 0.5 mm thick glass substrate with a 10 nm thick titanium adhesion layer in between. Two 50 μm long, 0.2 μm wide, parallel slits with a separation of $d = 24.5$ μm , have been ion-beam-milled in the gold film. We record the normalized transmission spectrum of this double-slit system for various angles of incidence. The experimental results are shown in Fig. 2.6a, for angles of incidence of $0^\circ, 0.5^\circ, 1^\circ, 3^\circ$ and 5° (from top to bottom). A couple of features are noteworthy. First, when comparing the spectra at 0° and 1° angles of incidence one notices that they seem to have flipped: where one spectrum shows a maximum, the other shows a minimum, and vice versa. Second, some of the spectra appear to be featureless in certain spectral regions, for instance the spectrum at 3° angle of incidence for $743 < \lambda < 762$ nm.

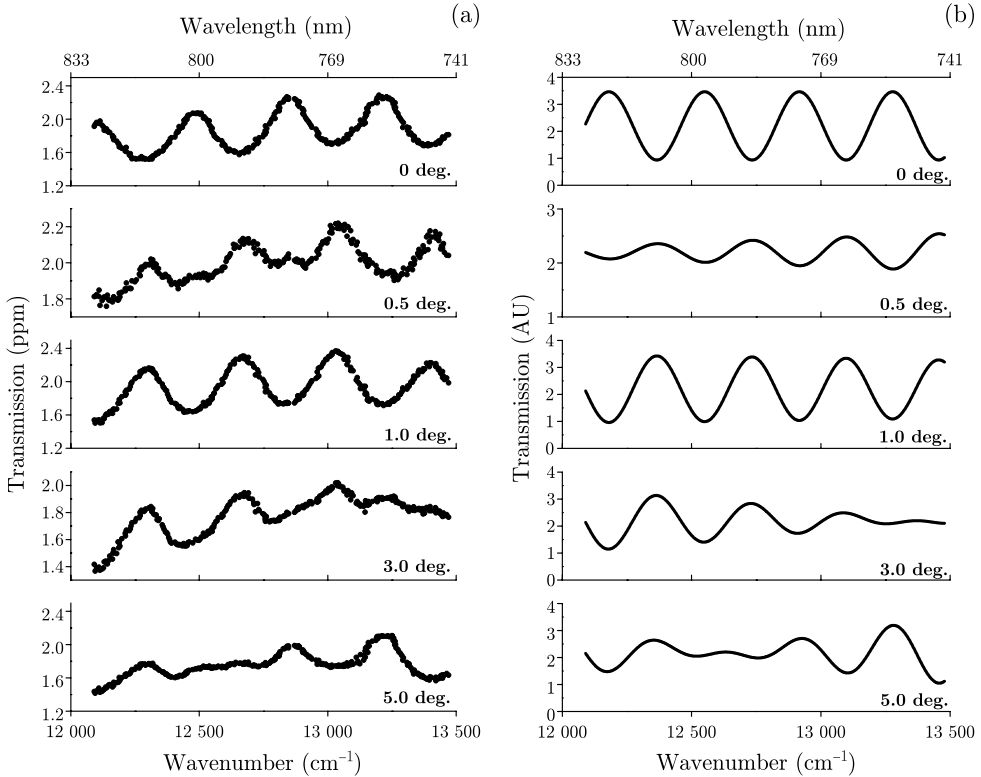


Figure 2.6. Experimental (a) and calculated (b) two-slit transmission spectra for angles of incidence of 0°, 0.5°, 1°, 3° and 5° (from top to bottom).

These observations can be explained by realizing that, at non-normal incidence, the relative phases $\Delta\phi_A$ and $\Delta\phi_B$ of the interfering channels in slits A and B are no longer equal (see Fig. 2.7). The fields in the two slits can be written as:

$$E_A = E_0[1 + \alpha \exp\{i(k_{\text{sp}}d + \Phi)\} \exp\{i\Delta\phi\}], \quad (2.5)$$

$$E_B = E_0[\exp\{i\Delta\phi\} + \alpha \exp\{i(k_{\text{sp}}d + \Phi)\}], \quad (2.6)$$

where α is the surface-plasmon coupling coefficient and Φ a coupling phase, both of which are introduced in Chapter 2, and $\Delta\phi = k_0d \sin \psi$ is the extra phase accrued by the light when traveling to slit B, with k_0 the wave vector of free space.

The detector signal $S(\lambda)$ can now be calculated¹ by evaluating $|E_A|^2 + |E_B|^2$,

$$S(\lambda) = S_0[1 + \alpha^2 + 2\alpha \cos(k_{\text{sp}}d + \Phi) \cos(k_0d \sin \psi)]. \quad (2.7)$$

It is seen that the term $2\alpha \cos(k_{\text{sp}}d + \Phi)$, describing the spectral modulation, is itself amplitude modulated by the term $\cos(k_0d \sin \psi)$. Whenever the latter term goes to zero, the plasmon-induced spectral modulation is suppressed. Figure 2.6b shows the spectra according to Eq. (2.7) for $\alpha = 0.2$ and $\Phi = \pi$ (see Chapter 5).

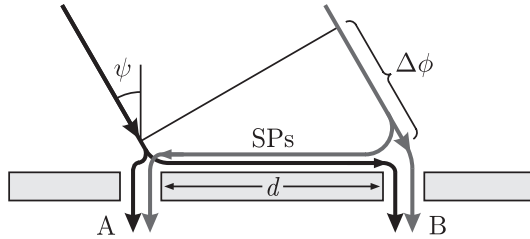


Figure 2.7. Pathways of light and surface plasmons when the sample is illuminated at an angle of incidence equal to ψ .

We find good agreement between the calculated and observed modulation spectra. Note that the spectral modulation at an angle of incidence of 0.5° is calculated to be almost erased. This can be understood by evaluating the quantity $k_0d \sin \psi$, which varies between 0.52π and 0.58π across the wavelength range studied so that $\cos(k_0d \sin \psi) \approx 0$. The observed phase shift of the modulation pattern upon changing the angle of incidence from 0° to 1° is due to the fact that $k_0d \sin \psi$ goes from 0 to $\approx \pi$.

Another way to look at the erasure phenomenon is by realizing that the spectral modulation originates in an interference phenomenon in each of the slits. The modulation being erased implies that, at the detector, the interference is made to vanish. By writing the signals from slits A and B as:

$$S_A = S_0[1 + \alpha^2 + 2\alpha \cos(k_{\text{sp}}d + \Phi + \Delta\phi)], \quad (2.8)$$

$$S_B = S_0[1 + \alpha^2 + 2\alpha \cos(k_{\text{sp}}d + \Phi - \Delta\phi)], \quad (2.9)$$

we realize that the spectral modulation in S_A is π out of phase with that in S_B whenever $\Delta\phi = \pi/2 + m\pi$, with m an integer.

¹A bucket detector is used to collect most of the interference orders such that the spatial information is effectively erased.

Clearly, the plasmon-induced modulation of the two-slit transmission spectrum is quite sensitive to the angle of incidence of the illuminating light. That implies that one has to be quite careful when illuminating the sample with a focussed beam, as such a beam can be described as a superposition of plane waves at different angles of incidence. With a strongly focussed beam it is quite possible to wash away most of the modulation features in the transmission spectrum of the double slit.

CHAPTER 3

Enhanced spatial coherence by surface plasmons¹

We report on a method to generate a stationary interference pattern from two independent optical sources, each illuminating a single slit in Young's interference experiment. The pattern arises as a result of the action of surface plasmons travelling between sub-wavelength slits milled in a metal film. The visibility of the interference pattern can be manipulated by tuning the wavelength of one of the optical sources.

¹) N.V. Kuzmin, G. Gbur, H.F. Schouten, T.D. Visser, G.W.'t Hooft and E.R. Eliel, *Enhanced spatial coherence by surface plasmons*, Opt. Lett. **32**, p. 445 (2007)

3.1 Introduction

It is well known that the visibility of the interference fringe pattern observable in Young's double-slit experiment is determined by the spatial and temporal coherence properties of the light incident on the slits [58]. For a stationary light field, these properties are described by the mutual coherence [58–60] function

$$\Gamma(P_1, P_2, \tau) = \langle E^*(P_1, t) E(P_2, t + \tau) \rangle, \quad (3.1)$$

with E the complex amplitude of the field, assumed here to be scalar; P_1 and P_2 denote the positions of the slits, τ a delay time, and the brackets a time average. For our purpose it useful to employ the normalized mutual coherence function (the so-called complex degree of coherence), defined as

$$\gamma(P_1, P_2, \tau) = \frac{\Gamma(P_1, P_2, \tau)}{\sqrt{I(P_1)I(P_2)}}, \quad (3.2)$$

where $I(P_i)$ is the averaged intensity at slit i . Under typical circumstances, the visibility \mathcal{V} of the interference fringes near a point P in the far zone is equal to the modulus of the complex degree of coherence, i.e.

$$\mathcal{V} = |\gamma(P_1, P_2, \tau)|, \quad (3.3)$$

with τ equal to the time difference $(\overline{P_1P} - \overline{P_2P})/c$, c being the speed of light in air. If one slit is illuminated by a light source radiating at frequency ω_1 while the other slit is illuminated by a separate source, radiating at frequency ω_2 , it is easily seen that then $\gamma(P_1, P_2, \tau) = 0$. Under these illumination conditions the fringe visibility should thus be zero across the entire interference pattern for sufficiently long integration times.

In this line of reasoning it is assumed that the radiative field *emerging from a slit* is simply, up to some factor, equal to the radiative field *incident on that slit*. When surface plasmons propagate between the two slits this assumption is no longer valid [61,62]. Consequently, a stationary interference pattern should be observed even if the frequencies of the lasers illuminating the individual slits are very different. Here we confirm this idea in an experiment where the two lasers run at frequencies differing by as much as 1.8 THz. Furthermore, we show that an interference pattern is also observed when only *one* slit is illuminated. When the polarization of the incident light is chosen such that no surface plasmons can be excited, the stationary interference pattern is observed to be absent.

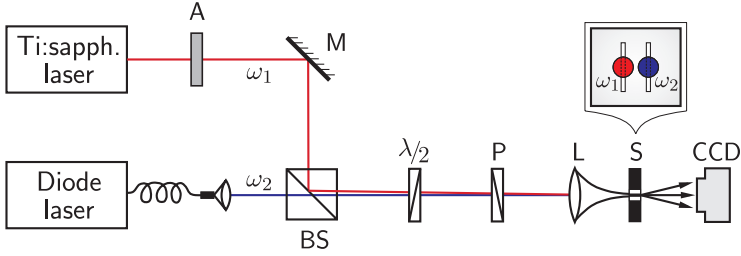


Figure 3.1. Sketch of the experimental setup. The outputs of a fiber-coupled diode and a Ti:sapphire laser are individually focussed on one of a pair of 200 nm wide slits, separated by $\approx 25 \mu\text{m}$, in a thin gold film. The light diffracted at the two parallel slits is imaged onto a CCD camera. A = attenuator, M = mirror, BS = beam splitter, $\lambda/2$ = half-wave plate, P = polarizer, L = lens, and S = gold sample. The inset shows the illumination of the double slit.

3.2 Experiment

The experimental setup is shown in Fig. 3.1. Two separate lasers, a tunable narrow-band Ti:sapphire laser and a semiconductor diode laser operating at 812 nm, each illuminate a single sub-wavelength slit in a 200 nm thick gold film. Each laser is focused to a spot of approximately $5 \mu\text{m}$ FWHM. The two parallel slits, $\sim 25 \mu\text{m}$ apart, are $50 \mu\text{m}$ long and $0.2 \mu\text{m}$ wide. The gold film is evaporated on top of a 0.5 mm thick fused-quartz substrate with a 10 nm thick titanium adhesion layer between the gold and the quartz. A CCD camera is used to record the far-field pattern.

3.3 Results

When the polarization of the two beams is parallel to the two slits (TE polarization), the resulting far-field pattern exhibits no fringes (see Fig. 3.2a), thereby confirming that the fields emerging from the two slits are completely uncorrelated ($\gamma(P_1, P_2, \tau) = 0$). However, when the polarization is changed to be perpendicular to the slits (TM polarization), a stationary interference pattern is obtained: $\gamma(P_1, P_2, \tau) \neq 0$. This is shown in the bottom part of Fig. 3.2, with a fringe visibility $\mathcal{V} = 20\%$. The fact that the appearance of interference depends on the polarization of the incident beams demonstrates that the interference phenomenon can not be attributed to one or both of the input beams illuminating the two slits to some extent.

Because the frequency difference between the two laser beams is so large

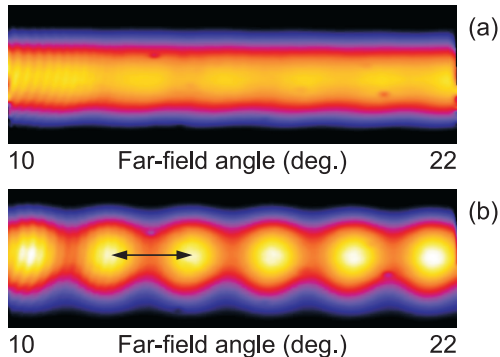


Figure 3.2. (a) The far-field pattern for the case that both laser beams are TE-polarized (polarization parallel to the slits). The semiconductor laser emits at 812 nm while the Ti:sapphire laser is tuned to 808 nm. (b) The experimental far-field pattern when the polarization of both laser beams is perpendicular to the two slits (TM polarization). Large-period fringes with a visibility $\mathcal{V} \approx 20\%$ are easily discerned. The arrow indicates the period of the fringes.

the mutual coherence (Eq. (3.1)) of the light fields *incident on* slit 1 and slit 2 is identical to zero, independent of the polarization. The fact that we, nevertheless, observe interference fringes for the case of TM-polarized illumination indicates that the fields *emerging from* slits 1 and 2 must, in that case, be at least partially mutually coherent. This mutual coherence is acquired by traversing the sample and, in view of the wavelength range of our study and the separation of the slits, we attribute it to the action of surface plasmons [8, 63]. Only when the incident light is TM polarized can they be excited at the slits. In the geometry of our sample they travel from one slit to the other with little loss, the slit separation ($\sim 25\mu\text{m}$) being smaller than their attenuation length ($\sim 40\mu\text{m}$) [64]. At the second slit the surface plasmons are partially converted back into a propagating light field [34, 61]. The consequence is that, while we illuminate slit 1 with a laser operating at frequency ω_1 and slit 2 with a laser operating at frequency ω_2 , *both slits will scatter at frequencies ω_1 and ω_2* . Moreover, since the processes of scattering free-space radiation into a surface plasmon and vice versa are phase coherent, the plasmon-mediated emission at frequency ω_2 from slit 1 is fully coherent with the direct emission by slit 2 at that frequency. Similarly, the plasmon-mediated emission by slit 2 and the direct emission by slit 1 at frequency ω_1 are fully coherent. Therefore, each frequency generates its own interference pattern with nonzero visibility.

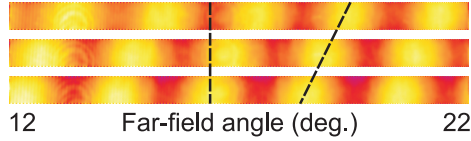


Figure 3.3. Interference patterns recorded with only a single slit illuminated by the TM-polarized output of the Ti:sapphire laser for, from top to bottom, $\lambda = 767$ nm, $\lambda = 775$ nm and $\lambda = 784$ nm.

To corroborate the proposed explanation we have switched off one of the lasers so that only *a single slit is illuminated* (by a single laser). One then expects to again observe an interference pattern when the incident light is TM-polarized and none when it is TE-polarized. This is confirmed by the experiment, with Fig. 3.3 showing the results for the case of TM-polarized illumination. Here, the fringe visibility, of order 0.2, does not provide a measure for the phase correlation between the fields emitted by the two slits; it rather reflects the unbalance of the intensities of the fields emerging from the two slits (ratio ≈ 170). This unbalance can be tuned by adjusting the widths of the individual slits. High-visibility fringes are observed only when sub-wavelength slits as narrow as the ones of the current experiment (200 nm) are used.

Additional support for our interpretation in terms of surface-plasmon-enhanced spatial coherence comes from measuring the shift of the interference pattern upon changing the wavelength of the incident radiation. As shown in Fig. 3.3 we record the interference pattern for far-field angles ranging between 12° and 22° , at the right side of the z -axis. If the left slit is illuminated and the wavelength is increased from 767 nm to 784 nm, the fringes shift to the left by approximately half a fringe, as shown in the figure. Actually, all the fringes that can be recorded shift to the left. However, when the right slit is illuminated, one observes that all the fringes shift to the right. This is not possible in a traditional Young's-type experiment where the interference arises as a result of *both* slits being illuminated by a *single* source. In that case the pattern expands symmetrically around the z -axis.

Because the surface plasmon has to propagate from one slit to the other, the field emitted by the non-illuminated slit is delayed relative to that of the directly illuminated slit, the phase delay $\Delta\phi(\omega)$ being equal to

$$\Delta\phi(\omega) = k_{\text{sp}}(\omega)d + \psi. \quad (3.4)$$

Here $k_{\text{sp}}(\omega)$ is the surface-plasmon propagation constant, d the slit separation, and ψ a scattering-induced phase jump. The angular position of an interfer-

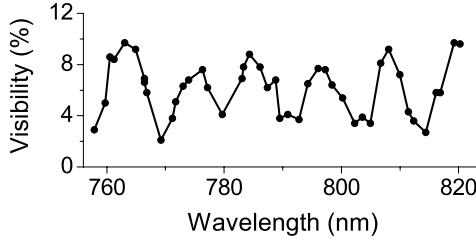


Figure 3.4. The fringe visibility of the recorded pattern (for TM-polarization) as a function of the wavelength of the Ti:sapphire lasers.

ence maximum is then given by

$$k_0 d \sin \theta \pm \Delta\phi(\omega) = 2\pi m, \quad (3.5)$$

the sign depending on which slit is being illuminated. Here k_0 represents the free-space wave number of the incident radiation, and m is an integer. From this expression one calculates that the pattern shifts by half a fringe spacing for a wavelength change of 17 nm, in excellent agreement with the experimental result shown in Fig. 3.3.

In the case that both slits are illuminated (as in Fig. 3.2), albeit at different frequencies, we expect to observe an *incoherent superposition of two fringe patterns*. If ω_1 and ω_2 are not vastly different, as in the present experiment, these patterns have very similar fringe spacings. However, because of the frequency-dependent phase delay of Eq. (3.4), these interference patterns can be aligned in different ways. In the case that the two patterns are perfectly aligned the observed interference pattern will have good visibility, while the visibility of the observed pattern can become close to zero when the two wavelengths are chosen so that the nodes of the pattern at one frequency overlap with the antinodes of the pattern at the other frequency. Consequently, one expects the visibility of the fringe pattern to go up and down when tuning, for instance, ω_1 . Figure 3.4 shows our experimental results, taken in a setup using two synchronously tuned Ti:sapphire laser beams, that confirm this picture.

A peculiar situation arises when the frequencies of the two incident beams are almost equal. Let us suppose that, at this frequency, $\Delta\phi(\omega) \approx (2m + 1)\pi$, so that the fringe pattern at each of the frequencies shows a minimum in the center ($\theta = 0$). One then would observe an intensity *minimum* at the center of the fringe pattern. However, when the two lasers have equal frequencies and are phase-locked one should observe an intensity *maximum* at the center, as explained in any textbook on optics [59].

3.4 Conclusions

In conclusion, we have demonstrated that interference fringes can arise in Young's double-slit experiment under conditions where they are not usually found. In particular, we have shown that such fringes can appear when the illumination of one of the slits is completely spatially incoherent with that of the other. We attribute this effect to the action of surface plasmons generated at, and traveling between the two slits. Using a variety of experimental approaches we have shown this picture of surface-plasmon enhanced coherence to be consistent. Whereas the vast majority of recent work on surface plasmons focuses on enhancement of the field or its transmission, i.e. on an effect involving the intensity of the light field, our work demonstrates that surface plasmons also have a profound influence on its coherence properties leaving much territory to be explored [62].

CHAPTER 4

Bouncing surface plasmons¹

Employing an interferometric cavity ring-down technique we study the launching, propagation and reflection of surface plasmons on a smooth gold-air interface that is intersected by two parallel, sub-wavelength wide slits. Inside the low-finesse optical cavity defined by these slits the surface plasmon is observed to make multiple bounces. Our experimental data allow us to determine the surface-plasmon group velocity ($v_{\text{group}} = 2.7 \pm 0.3 \times 10^{-8}$ m/s at $\lambda = 770$ nm) and the reflection coefficient ($R \approx 0.04$) of each of our slits for an incident surface plasmon. Moreover, we find that the phase jump upon reflection off a slit is equal to the scattering phase acquired when light is converted into a plasmon at one slit and back-converted to light at the other slit. This allows us to explain fine details in the transmission spectrum of our double slits.

¹) N.V. Kuzmin, P.F.A. Alkemade, G.W. 't Hooft and E.R. Eliel, *Bouncing surface plasmons*, Opt. Exp. **15**, p. 13757 (2007)

4.1 Introduction

The observation by Ebbesen *et al.* [36] that a metal film that is perforated by a regular array of sub-wavelength holes transmits much more light than what is predicted by classical theory [37] has sparked a wide-ranging research effort into the physics of electromagnetic fields interacting with structured metal films. It is now broadly understood that surface plasmons (SPs) play a very important role in this transmission enhancement and this understanding has birthed a novel field of research commonly called “plasmonics”. Possible applications of plasmonics can be found in microscopy [65], bio-sensing [66,67], nano-optics [68,69], nonlinear optics [70], cavity-QED [71] etc.

Although the transmission enhancement by surface plasmons in a metal hole array is dramatic, this 2D system is not optimal for studying the basic physics of scattering of EM radiation by perforations in metal films. Single sub-wavelength holes or slits in thin metal films provide more fundamental systems and their transmission has therefore received considerable attention, both theoretically and experimentally [72]. An elegant extension to these basic systems is provided by the double slit, well known from Thomas Young’s landmark experiment; it has recently been shown that surface plasmons can give rise to a modulation of the transmission spectrum of the double slit [34, 35, 61, 73]. Furthermore, it has been reported that the spatial coherence of the light field behind such a double slit can be modified by the surface plasmons [74, 75]. In this type of experiments the sub-wavelength slit acts as an antenna — it scatters the incident radiation field into (Fig. 4.1a): i) a forward propagating field with emission angles ranging from $-\pi/2$ to $+\pi/2$; ii) a surface plasmon field travelling away from the slit along the metal-dielectric interface; iii) evanescent modes. A second, nearby slit can act as a receiver for the surface plasmon field and scatter it into, e.g., free space or into a backward-travelling/transmitted plasmon (Fig. 4.1b).

Incident light, that is coherently scattered into a plasmonic mode by one of the slits, can be re-radiated by the other slit, with a well-defined phase relationship with the light that is forward scattered by the latter slit; this explains the observed wavelength modulation of the transmission spectrum of the double slit [61].

A different perspective on this modulation is that it represents the eigenmode spectrum of the metallic resonator bounded by the two slits [76]. The near vicinity of metallic regions at the other side of each slit will have an effect on this spectrum; in a way they “dress” the resonator. The measured spectrum is then actually the extinction spectrum of the dressed inter-slit metallic 2D cavity [77]. This spectrum arises due to the multiple interference of waves

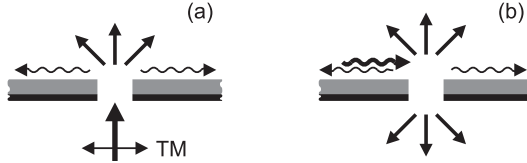


Figure 4.1. (a) The coupling of incident TM-polarized light into surface plasmons propagating along the metal-dielectric interface on top, accompanied by direct transmission; (b) Incident surface plasmon out-coupling to free-propagating light, back-reflection and tunneling through the slit. Bottom interface is covered with metal (Ti) that suppresses surface plasmon propagation.

that travel up and down the cavity, displaying sharp structure when the waves make many round trips through the resonator, and shallow features when the number of round trips is small (of order 1). In conventional optical resonators this number depends on the loss per round trip [78]. There are two contributions to this loss: internal loss due to extinction during propagation through the resonator (usually small or negligible in conventional optical resonators), and loss due to the finite mirror reflectivity or to diffractive losses at the edges of the mirror [78]. Both types of loss apply to our metallic resonator.

Here we report on time-domain measurements of the decay of the surface plasmon as it travels up and down a mesoscopic metallic resonator defined by sub-wavelength slits. These measurements yield data on the surface-plasmon group velocity, the reflection coefficient of a surface plasmon for a sub-wavelength slit, and on phase jumps upon scattering and reflection.

4.2 Experiment

A conventional optical resonator is characterized by two parameters, namely the cavity round-trip time $t_{\text{ax}} = L/v_{\text{group}}$ and the cavity decay time $\tau_{\text{cav}} = -t_{\text{ax}}/\ln(R)$, with R the mirror reflectivity. The former measures the time it takes a pulse to make a round trip through the cavity of length L , while the latter equals the $1/e$ decay time of the intracavity power. The equivalent parameters in the frequency domain are the free spectral range $\omega_{\text{ax}} = 2\pi/t_{\text{ax}}$ and the *finesse* \mathcal{F} ; the finesse measures the ratio of the free spectral range and the cavity linewidth. Round-trip losses are the dominant factor that determine the finesse, and in conventional stable optical resonators the round-trip loss is usually determined by the reflectivity of the mirrors.

In the system under study, i.e., a resonator for surface plasmons, the round-

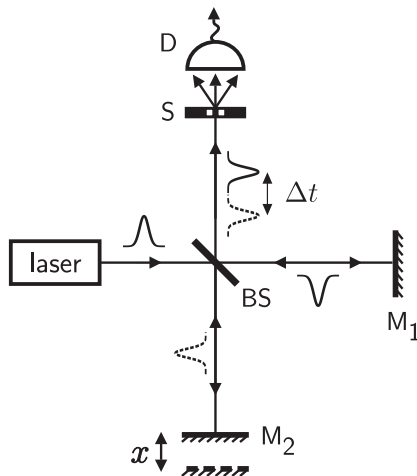


Figure 4.2. Experimental interferometer setup. The output of a wave-length tunable ultrashort pulsed Ti:sapphire laser, $\lambda = 770\text{--}800$ nm, is incident on a 50/50 beamsplitter (BS). The light reflects from two broadband dielectric mirrors (M_1, M_2) and is recombined at the beamsplitter. Behind the sample (S) the light is detected by a Si photodiode detector (D). The pump-probe delay is varied by moving mirror M_2 .

trip losses are not only determined by the slit reflectivity but also by damping of the surface plasmon as it travels between the slits, due to the finite conductivity of the metal film. By a judicious choice of the cavity length L we can tune the ratio of these two loss mechanisms. Measurements of the spectrum of a surface-plasmon resonator consisting of a smooth metal film bounded by two sub-wavelength slits demonstrate that its finesse is small ($\mathcal{F} \approx 2$) [61]. In that limit the finesse of a resonator is not a sensitive measure of the reflectivity as opposed to the case that the finesse is high, and requires experimental data with good signal-to-noise ratio. Note that if the finesse of a cavity is low it is not given by the well-known approximate expression $\mathcal{F} = \pi R^{1/2}/(1 - R)$, but by $\mathcal{F} = \pi/\{\arccos[2R/(1 + R^2)]\} \approx 2(1 + 4R/\pi)$. We therefore have chosen to measure in the time domain, essentially using a cavity ring-down technique [79].

While a surface plasmon in the near-infrared spectral region ($\lambda \approx 800$ nm) propagates along a flat and unstructured air-gold interface its amplitude decays over a length of order $100 \mu\text{m}$ [8, 53]. Unless a gain medium is present [80], a SP cavity should have a length that is, at most, of that same order and, therefore, the cavity round-trip time will not be larger than a few hundred femtoseconds. For modest values of the cavity finesse, the SP cavity ring-down

time will be of that same order of magnitude. Because of this ultra-short time scale traditional cavity ring-down techniques, where the power leaking through one of the cavity mirrors is monitored in real time [79], are not suited to the case of a SP cavity. Upconversion and autocorrelation techniques [81] provide alternatives here; the latter is used in the present work.

As a sample we use a 200 nm thick plane gold film attached to a fused-quartz substrate by a 10 nm thick titanium adhesion layer. The film is perforated by two 50 μm long and 100 nm wide slits, separated by distances ranging from 25 to 90 μm . The titanium adhesion layer is strongly dissipative to surface plasmons [61]; consequently the SPs that we study here are those of the gold-air interface.

We illuminate the sample by the output of a Michelson interferometer which, in turn, is illuminated by a short-coherence-length femtosecond tunable Ti:sapphire laser (Fig. 4.2). We choose the polarization of the incident light to be perpendicular to the long axis of the slits (TM-polarization). The laser is operated at wavelengths around 770–800 nm, with a spectral width of $\approx 30\text{--}40$ nm, yielding a coherence length $\ell_{\text{coh}} \approx 16\text{--}20$ μm . The Michelson interferometer serves to generate a time-delayed copy of the laser pulse and, together, these two pulses illuminate both slits of our sample. We image the double-slit output on a low-noise detector (New Focus model 2001-FS) and measure its output as a function of the delay Δt between the two pulses incident on the sample. We collect the data on a computer using a 24-bit A/D converter (National Instruments PCI 5911) while slowly changing Δt using a motorized translation stage (Newport model CMA-25CCCL). Note that our experimental approach is slightly unusual in that we send *both* the original pulse, henceforth called pump, *and* its copy, called probe, onto our sample, instead of illuminating the sample with just one of the pulses [82]. We have made this choice because of the large angular spread of the output of the sample, its low transmission (typically 10^{-6} for a spot size of 50 μm diameter) and considerations of signal to noise.

4.3 Results

Experimental interferograms recorded with the laser operating at $\lambda = 770$ nm are shown in Fig. 4.3. The upper frame shows the autocorrelation trace obtained in the absence of a sample, yielding information on the instrumental response function of our setup. At a pump-probe delay of ≈ 50 fs the signal is essentially constant and remains so when the delay is increased. The lower frame shows the measured interferogram as recorded in the presence of our

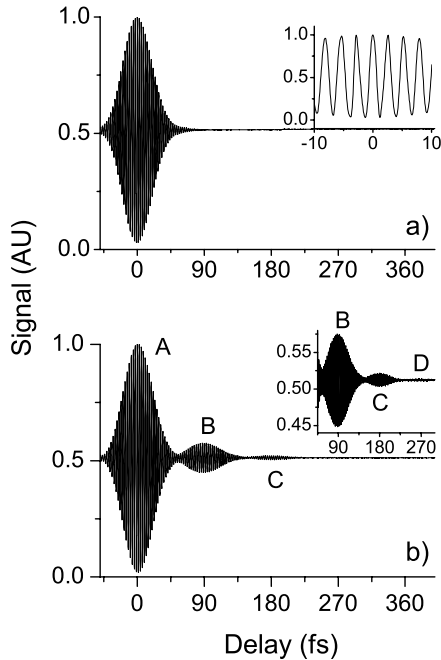


Figure 4.3. Experimental interferograms measured without sample (a) and with a sample containing a sub-wavelength slit pair with $25 \mu\text{m}$ slit separation (b). The insets show details of the interference signal.

sample, using a double slit with a slit separation of $25 \mu\text{m}$ and TM-polarized incident light. The interference fringes show a quite different behavior here: most noticeably one observes the signal to partially recover after the initial collapse (peak B, Fig. 4.3b). This “echo” has an amplitude of order 10% of the initial signal. Upon careful observation one notices that the signal goes through an additional cycle of collapse and recovery (peak C). When the polarization of the incident light is chosen to be TE, we observe no revivals; the signal is indistinguishable from that measured with the double slit absent (Fig. 4.3a).

As we will argue below, the first echo (B) comes about because surface plasmons are launched at the slits, travel from one slit to the other, to arrive there after a delay Δt ; the second, weaker, echo (C) arises because a surface plasmon that is launched at one of the slits, can be back-scattered by the other slit to return to its place of birth with a delay equal to $2\Delta t$.

More detailed information on the sequence of echo’s can be obtained by demodulating the signal of Fig. 4.3b to obtain its carrier envelope; the latter we

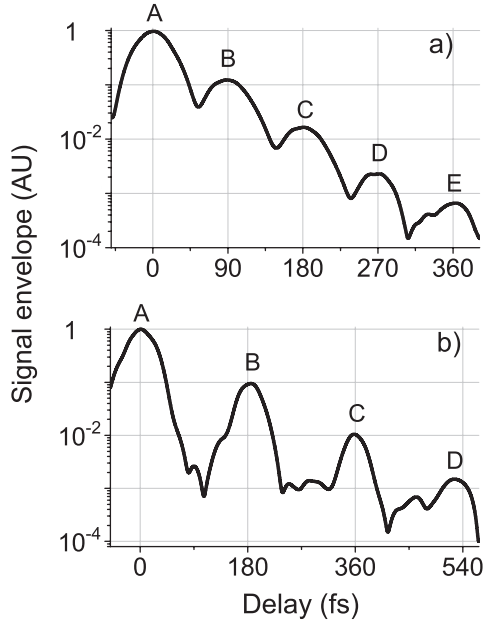


Figure 4.4. Carrier envelopes of the demodulated experimental signal for samples with slit separation equal to $25 \mu\text{m}$ (a) and $50 \mu\text{m}$ (b), respectively.

plot, on a logarithmic scale, in Fig. 4.4a. Here we see that the signal contains *five* interference maxima (peaks A–E), spanning four decades of signal. The interference maxima are equidistant with a peak-to-peak separation of 93 fs. The two additional peaks that show up in the carrier envelope (D,E) are then identified with the case that a surface plasmon is back-scattered *twice* and *three times*, respectively. Altogether, the surface plasmon is seen to make two full round trips through the cavity. Figure 4.4b shows the carrier envelope for the case that a double slit with a slit separation of $50 \mu\text{m}$ is studied. Here we observe essentially the same features as before, except that, naturally, the subsidiary maxima are farther apart and thus better resolved.

4.4 Discussion

The experimental data of Fig. 4.4 give direct access to some important experimental parameters, i.e., the SP group velocity v_{group} , the complex SP coupling factor α , and the (complex) SP amplitude reflection coefficient r . When the subsequent peaks in the interferogram are well separated and the

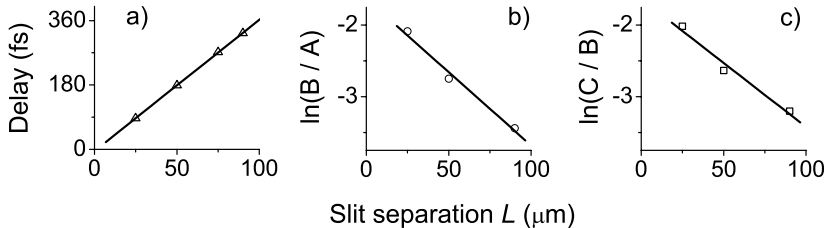


Figure 4.5. (a) Delay between peaks A (direct transmission) and B (representing the surface plasmon wavepacket) for different slit separations L . The slope of the line through the points determines the value of $1/v_{\text{group}}$; (b) Ratio of the second to first peaks (B/A) as a function of the slit separation L ; (c) Ratio of the third to second peaks (C/B) for different values of the slit spacing.

group-velocity dispersion of the SP is small or negligible, the group velocity can be determined directly from the separation between subsequent peaks in the signal envelope. Both v_{group} and its dispersion can be calculated from the dispersion relation of the SP travelling along the plane interface between a metal and a dielectric [8],

$$k_{\text{sp}}(\omega) = \frac{\omega}{c} \sqrt{\frac{\epsilon_{\text{m}}(\omega)\epsilon_{\text{d}}(\omega)}{\epsilon_{\text{m}}(\omega) + \epsilon_{\text{d}}(\omega)}}, \quad (4.1)$$

with $\epsilon_{\text{m}}(\omega)$ and $\epsilon_{\text{d}}(\omega)$ the dielectric coefficients of the metal and the dielectric, respectively. We use the tabulated values for $\epsilon_{\text{m}}(\omega)$ [53] and set $\epsilon_{\text{d}}(\omega) = 1$, the dielectric being air. At $\lambda = 770$ nm we calculate $v_{\text{group}} = d\omega/dk_{\text{sp}} \simeq 2.72 \times 10^8$ m/s and a value for the group velocity dispersion $d^2k_{\text{sp}}/d\omega^2 \simeq 0.76$ fs²/μm equivalent to a group delay dispersion $d(v_{\text{group}}^{-1})/d\lambda \simeq -2.4$ as/nm·μm. For the experiment with a slit separation of 50 μm and the pulse spectral width $\Delta\lambda = 27$ nm (corresponding to a Fourier-limited \cosh^{-1} pulse duration of 32 fs) the group delay dispersion leads to a pulse broadening of only 5 fs and can therefore be neglected. It is therefore perfectly allowed to extract an experimental value of the SP group velocity directly from the separation between successive peaks in the interferogram (Fig. 4.5a), provided that they are well separated, as in the case of 50 μm slit separation. This yields $v_{\text{group}} = 2.70 \pm 0.03 \times 10^8$ m/s. This result is in excellent agreement with the calculated value and with [73], in contrast to the findings of Bai *et al.* [83]. An experimental indication that effects of group velocity dispersion are indeed small comes from the observation that all peaks in the interferogram have the same width.

The height of the various peaks in the interferogram provides information

on both the absolute value of the light \rightarrow SP \rightarrow light coupling coefficient α and of the SP reflection coefficient r . The peak-height ratio (B/A) of the first echo and the peak at zero delay is given by $|\alpha| \exp(-k''_{\text{sp}}L)$, while that of the second and first echo's (C/B) is given by $|r| \exp(-k''_{\text{sp}}L)$. By determining these peak-height ratio's from measurements performed on double-slit systems with different inter-slit separations L , and plotting these ratio's on a logarithmic scale versus L , as shown in Fig. 4.5, we can extract $|\alpha|$ and $|r|$ from the line intercepts and k''_{sp} from the slope of the lines. This yields $|\alpha| = 0.19 \pm 0.02$, $|r| = 0.18 \pm 0.01$ and $k''_{\text{sp}} = 0.02 \mu\text{m}^{-1}$. The damping constant is approximately twice the value that one calculates from the surface-plasmon dispersion relation (Eq. (4.1)) using Palik's data for the dielectric coefficient of gold [53]. We attribute the additional damping to the fact that our gold film has deteriorated over a period of a year of use, giving rise to scattering loss in the film. The value for α is in good agreement with the prediction by Lalanne *et al.* [34]. The intensity reflection coefficient $R = |r|^2$ of the slit is quite small ($R \approx 0.04$); consequently the cavity finesse is very small: $\mathcal{F} = 2.1$. Similar values for the reflection coefficients from edges and subwavelength-wide groves and barriers have been reported [84–89].

The interferogram is also sensitive to the phase of both α and r , and to illustrate that point we return to the resonator picture discussed earlier. The output of the “resonator” consists of a sequence of pulses, the first one (A) simply being the light directly transmitted through the slits, the second (B) due to the SP being excited at one slit and scattered back into light at the other slit, the third (C) due to the reflected SP being back-scattered into light at the first slit, etc. The transfer function $G(\omega)$ of the double slit can thus be written as:

$$G(\omega) = 1 + \alpha \exp[ikL] + ar \exp[2ikL] + ar^2 \exp[3ikL] + \dots, \quad (4.2)$$

$$= 1 + \frac{\alpha \exp[ikL]}{1 - r \exp[ikL]}, \quad (4.3)$$

with $k = k_{\text{sp}}(\omega)$ the complex surface-plasmon wave vector (see Eq. (4.1)); here the coefficients α and r are assumed to be frequency independent. In the limit that $r = 0$ this transfer function gives rise to a sinusoidally modulated two-slit spectrum [61], showing maxima whenever $kL + \arg(\alpha) = 2\pi m$, with m integer. Various theoretical studies suggest that $\arg(\alpha) = \pi$ [34, 61, 90].

Note that the transfer function of Eq. (4.2) is very similar to that describing the amplitude reflectivity of a conventional Fabry-Pérot resonator [59]:

$$\mathcal{R}(\omega) = r \left(1 - \frac{(1 - r^2) \exp[2ik_0L]}{1 - r^2 \exp[2ik_0L]} \right). \quad (4.4)$$

For not too small values of the (real-valued) amplitude reflectivity r of the resonator mirrors, the reflectivity spectrum $|\mathcal{R}(\omega)|^2$ of a Fabry-Pérot displays deep dips whenever $2k_0L = 2\pi m'$, with m' an integer, on an otherwise constant background. These resonances occur when the denominator in Eq. (4.4) reaches its minimum value. Because of the strong similarities between Eqs. (4.2) and (4.4) we conclude that the resonances of the transmission spectrum $|G(\omega)|^2$ of our double slit appear when $kL + \arg(r) = 2\pi n$, with n an integer. The shape of the resonance (dip, peak, or asymmetric Fano-type [91]) is then determined by the phase of $\alpha \exp[ikL]$, i.e., by $u = \arg(r) - \arg(\alpha)$. When $u = 0$ the spectrum shows peaks, when $u = \pm\pi$, the spectrum carries dips, and Fano-type features arise when $u \approx \pm\pi/2$. Experimental results for the plasmon-induced modulation of the two-slit transmission spectrum hint at a value for u close to zero [61].

The transmission spectrum of the double slit (see Eq.(4.2)) plays an important role also in the time-domain response of the double slit since the interferometer signal can be written as [92]:

$$I(t) = 2 \int_{-\infty}^{+\infty} |E(\omega)G(\omega)|^2 \cos(\omega t) d\omega, \quad (4.5)$$

with $E(\omega)$ the field incident on both slits. We assume here that our Michelson interferometer is symmetric, i.e. that the transfer functions of both interferometer arms are equal. If the spectrum of $E(\omega)$ is much broader than the separation $\Delta\Omega$ of modulation features in $G(\omega)$ (see Fig. 4.6a), the interferometer signal will approximately equal the Fourier transform of $|G(\omega)|^2$, i.e., the interferometer signal will consist of a rapidly decaying series of equidistant bursts, separated by an interval equal to L/v_{group} , representing the subsequent round trips through the cavity. The duration of these bursts (in units of pump-probe delay) is determined by the coherence time of the incident light τ_{coh} . In this limit one thus observes well separated individual pulses; Fig. 4.4b serves as an example. When the slit separation is reduced the modulation features in $G(\omega)$ lie further apart so that $E(\omega)$ and $G(\omega)$ are modulated on the same scale (see Fig. 4.6b). In that limit the interferometer signal consists of more or less overlapping peaks and, in the overlap regions is quite sensitive to the value of the parameter u , as we shall see below. The limit where the spectral width of $E(\omega)$ is much smaller than a single modulation feature of $G(\omega)$ (see

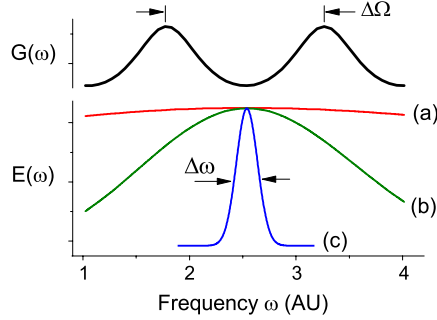


Figure 4.6. Spectral representation of the two-slit transfer function $H(\omega)$ and field $E(\omega)$ (a–c).

Fig. 4.6c) is uninteresting, corresponding to a situation where the coherence time of the incident light is much larger than the memory time of the two-slit cavity. In this limit, time-domain experiments are ineffective.

Let us now look in more detail at the intermediate regime where the coherence time τ_{coh} of the input pulse is comparable to the cavity round-trip time τ_{cav} . Let us further assume that the average frequency of the incident light is tuned so that $kL + \arg(\alpha)$ is an integer multiple of 2π (in the approximation that the surface plasmons do *not* reflect from the slits ($r = 0$), the incident light is tuned to a transmission maximum). Then the first two terms in Eq. (4.2) are in phase; in the interferometer signal the first two peaks will then add so that the dip between these peaks will be shallow. If $kL + \arg(r)$ is also an integer multiple of 2π (i.e., $u = 0$), all terms in Eq. (4.2) are in phase, so that all neighboring peaks in the interferogram are separated by shallow dips (see Fig. 4.7a). If, however, $kL + \arg(r)$ is an odd multiple of π ($u = \pi$), each subsequent term in Eq. (4.2) is out of phase with the previous one giving rise to deep dips between second, third, fourth, fifth etc. peaks in the interferogram (see Fig. 4.7b).

If, however, we tune the laser so that $kL + \arg(\alpha)$ is an odd multiple of π the first two terms in Eq. (4.2) are out of phase and give rise to a deep dip between the first two peaks in the interferogram. If now $kL + \arg(r)$ is an integer multiple of 2π (so that $u = \pi$) the subsequent terms in Eq. (4.2) will all be in phase with each other giving rise to shallow dips between peaks 2, 3, 4, ... in the interferogram (see Fig. 4.7c). If, however, $kL + \arg(r)$ is an odd multiple of π (so that $u = 0$) all subsequent terms in Eq. (4.2) will all be out of phase with each other giving rise to deep dips between all peaks in the interferogram (see Fig. 4.7d). Figures 4.7e and 4.7f show experimental results obtained for

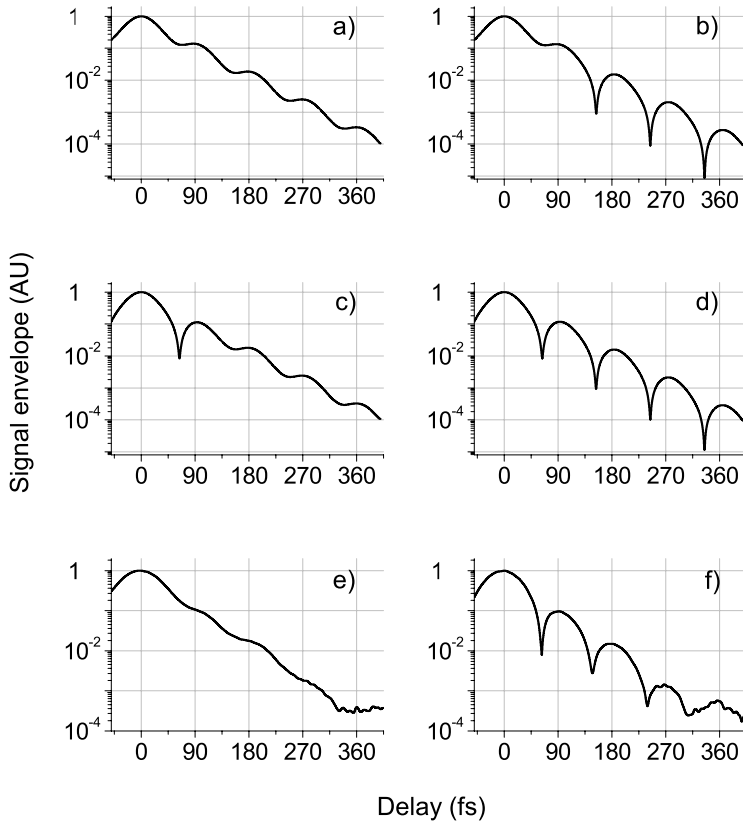


Figure 4.7. Calculated and experimental interferograms for various values of the tuning of the laser wavelength. Frames a) and d) show calculated data for the case that the phase parameter $u = 0$, while frames b) and c) show such data for the case that $u = \pi$. Frames e) and f) show experimental results for two different wavelength settings of the laser: in e) the laser is tuned to a transmission maximum; in f) to a transmission minimum.

the $25 \mu\text{m}$ slits at two different settings of the laser, one corresponding to the case $kL + \arg(\alpha) = 2m\pi$ (Fig. 4.7e) and one corresponding to the case $kL + \arg(\alpha) = (2m+1)\pi$ (Fig. 4.7f). These experimental results clearly suggest that $u \approx 0$.

This value for the parameter u fits well with the shape of the transmission spectrum of the double slit, as measured with TM-polarized incident light. Figure 4.8 shows such a spectrum together with spectra calculated on the basis that $|\alpha| = |r| = 0.2$, one spectrum for the case that $u = 0$, the other

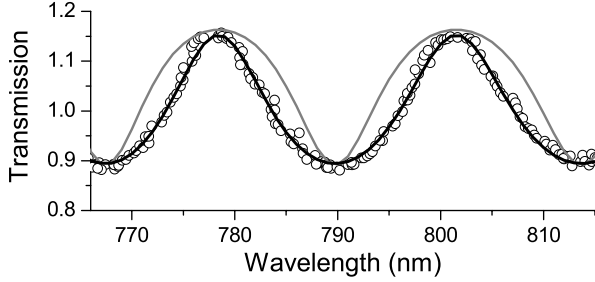


Figure 4.8. Double-slit transmission spectrum for TM-polarized incident light. The circles show the experimental data, the solid lines calculated spectra for $|\alpha| = |r| = 0.2$. The black line shows the result for $u = 0$, while the gray line represents a $u = \pi$ spectrum.

for the case $u = \pi$. Clearly, the curve with $u = 0$ provides a much better description of the experimental data than that with $u = \pi$.

4.5 Conclusions

In summary, we have used a high-dynamic range time-domain technique to investigate the propagation and scattering of surface plasmons as they travel between two sub-wavelength slits along the interface between air and a smooth gold film. With slit distances of the order of the surface-plasmon damping length, i.e. tens of micrometers, we have measured the group velocity of the surface plasmon and found it to be in excellent agreement with the value calculated from the dispersion relation using Palik's tabulated values for the dielectric properties of gold in the near-infrared spectral region. Furthermore, we have determined the magnitude of the surface-plasmon scattering and reflection coefficients upon interaction with the sub-wavelength slits. The magnitude of the scattering coefficient, describing the second-order process where incident light is scattered into a surface-plasmon which, in turn, is scattered into diffracted light, is in good agreement with the value recently calculated by Lalanne *et al.* [35]. The measured value of the reflection coefficient agrees well with theoretical calculations [24, 88] and experimental data obtained with somewhat different nano-structured surfaces [85, 87]. Finally, we have determined that the scattering and reflection coefficients have roughly equal phase. The latter result allows us to explain fine details in the transmission spectrum of the double slit that have, hitherto, gone unnoticed.

4.6 Appendix: Slowed-down surface plasmons (unpublished)

The dispersion of a surface plasmon that propagates along a metal-dielectric interface is sensitive to the dielectric permittivity ϵ_d of the dielectric (see Fig. 4.9). Consequently, the group velocity, given by the tangent to the dispersion curve at a specific value of ω , is also sensitive to the dielectric's permittivity. Here we present some experimental results that probe that dependence.

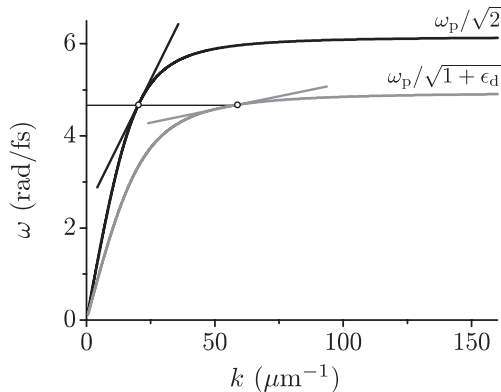


Figure 4.9. Dispersion relation for a surface plasmon traveling along a smooth interface between a metal and air (dark solid line) and between a metal and a dielectric with permittivity ϵ_d (light solid line).

We use the experimental arrangement of the foregoing Chapter, using a laser emitting transform-limited 100 fs pulses at $\lambda = 800$ nm. We illuminate the sample from the metallic side and probe the $90 \mu\text{m}$ double slit that is milled in the gold film. Consecutively, we deposit thin layers of methanol, ethanol and acetone on the sample and measure the group velocity of the surface plasmons traveling between the slits. At $\lambda = 800$ nm the refractive indices of these liquids at room temperature (20°C) are $n = 1.3290$ (methanol), $n = 1.3614$ (ethanol) and $n = 1.3590$ (acetone), respectively. The thickness of the liquid layer is chosen to be so large that the (phantom) peaks in the interferogram arising from multiple reflections between the air-liquid and liquid-gold interfaces are outside our range of interest.

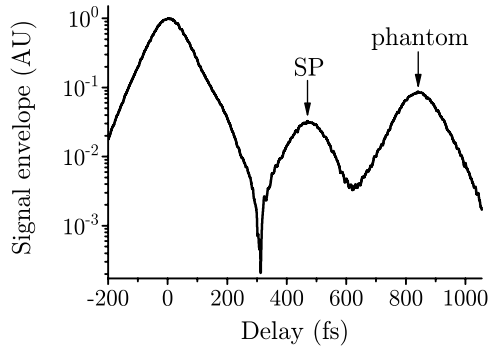


Figure 4.10. Envelope of the interferogram arising from the gold-ethanol interface for two slits that are $90 \mu\text{m}$ apart.

The experimental data for the gold-ethanol interface are shown in Fig. 4.10. Apart from the peak at zero delay one distinguishes a peak associated with the surface-plasmon traveling between the slits (labeled SP) and a phantom peak associated with reflections of the incident light in the thin layer of liquid. Since the various peaks in the interferogram are well separated we can immediately deduce a value for the surface-plasmon group velocity at $\lambda_{\text{inc}} = 800 \text{ nm}$ on the gold-liquid interface. The results are collected in Table 4.1, together with values for the group velocity calculated with the dispersion diagram. The agreement is excellent.

Dielectric	Measured group velocity (m/s)	Calculated group velocity (m/s)
Methanol	$1.97 \pm 0.04 \times 10^8$	1.96×10^8
Ethanol	$1.93 \pm 0.04 \times 10^8$	1.90×10^8
Acetone	$1.97 \pm 0.04 \times 10^8$	1.90×10^8
Air	$2.70 \pm 0.03 \times 10^8$	2.72×10^8

Table 4.1. Values of the group velocity of a surface plasmon traveling along a gold-dielectric interface for various dielectric materials. The experiments were performed at $\lambda = 800 \text{ nm}$.

Interestingly, the experimental data of Fig. 4.10 show a very pronounced dip between the peak at zero delay and the peak associated with the surface plasmon, indicating that, in this experiment, the center of the laser spectrum is very well aligned with a transmission *minimum* of the double-slit transmission function.

4. Bouncing surface plasmons

We have tried to extend these measurements to liquids such as benzyl-alcohol, which have a higher refractive index $n \simeq 1.54$. These, however, were unsuccessful. Probably, in these cases, the liquid layer formed a wedge so that, effectively, the sample was tilted. As discussed in the Appendix to Chapter 2, the plasmonic interference effects can easily be washed out in that case.

CHAPTER 5

Phase factors in light-plasmon scattering

We present an experimental study of the scattering of surface plasmons that propagate along a smooth metallo-dielectric interface off sub-wavelength slits milled in a metal film. We use configurations containing a combination of two and three slits to obtain detailed information on the scattering phase, and the tunneling amplitude and phase. We also demonstrate that the light transmitted by our structures has a space-variant polarization.

5.1 Introduction

When light impinges on the interface between a dielectric, characterized by a (real) dielectric coefficient $\epsilon_d(\omega)$, and a metal surface with dielectric coefficient $\epsilon_m(\omega)$, and that interface is not perfectly smooth, part of the light will be reflected, part will be directly scattered into free-space modes, and part will be converted into surface modes [8,24]. For almost all metals these surface modes are heavily damped. However, on gold, silver and aluminium, the surface mode is only weakly damped (in certain wavelength ranges) and is known as the surface plasmon or, more precisely, as the surface plasmon polariton [8,93,94]. This mode appears when the real parts of the dielectric coefficients of the metal and of the dielectric, $\epsilon'_m(\omega)$ and $\epsilon_d(\omega)$, have opposite sign. In essence, this means that $\epsilon'_m(\omega) < 0$. Since $\epsilon'_m(\omega) = n^2(\omega) - \kappa^2(\omega)$, with $n(\omega)$ and $\kappa(\omega)$ the real and imaginary parts of the refractive index, the requirements reads $n(\omega) < \kappa(\omega)$ or, in order to have a low-loss surface plasmon, $n(\omega) \ll \kappa(\omega)$. In the near-infrared spectral region silver and gold fulfill these requirements and are the metals of choice for the study of surface plasmons.

For a planar metallo-dielectric interface that supports a surface plasmon one can write for the wave vector of that mode [8]:

$$k_{\text{sp}} = \frac{\omega}{c} \sqrt{\frac{\epsilon_d \epsilon_m}{\epsilon_d + \epsilon_m}}. \quad (5.1)$$

Since ϵ_m is complex, so is k_{sp} . In the present chapter the imaginary part of k_{sp} , which quantifies the damping of the surface plasmon, plays only a minor role and will be largely neglected. The real part of k_{sp} yields the propagation constant of the surface plasmon; it can be calculated by replacing ϵ_m in Eq. (5.1) by its real part ϵ'_m [8]. Henceforth, we will denote the propagation constant as k_{sp} .

Since $\epsilon_d > 0$ and $\epsilon'_m < 0$, we have $k_{\text{sp}} - \sqrt{\epsilon_d} \omega / c > 0$, showing that there is a mismatch between the wave vectors of the interface-bound surface plasmon and of the unbound modes at the same frequency. Because of this mismatch surface plasmons can not be excited on a smooth metallo-dielectric interface when it is illuminated by a plane wave. However, a prism coupler [25,26] or a corrugation of the interface will be able to supply the missing momentum so that the incident light will couple to surface plasmons. By the same token, surface plasmons are able to couple to free-space radiation wherever the interface is not smooth. So, whenever a surface plasmon traveling along a smooth metallo-dielectric interface encounters a bump, trench, hole or slit, it is scattered into a transmitted plasmon, a reflected plasmon, and into free-space radiation (see Fig. 4.1b in Chapter 4). Associated with each of these

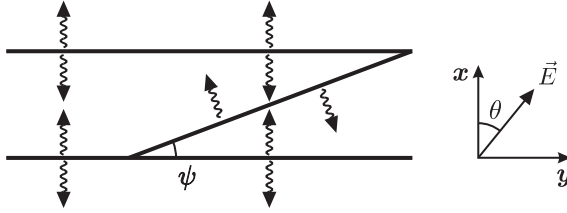


Figure 5.1. Composite slit structure consisting of a double slit, at left, and a three-slit section at right. The slanted slit is oriented at an angle ψ relative to the two parallel slits. When a light beam, polarized at an angle θ relative to the x direction, is incident on the structure, surface plasmons, indicated by wiggly arrows, are launched by each of the slits.

scattering channels is a scattering amplitude and phase. These corrugations can thus be seen as a multi-port splitter [24, 95]. Theoretically, this subject has been extensively researched by Maradudin and others [84, 94, 96–98].

Let us consider the case that a smooth and thin metal film is perforated by two close-lying long and narrow slits. Let us further assume that these two apertures are illuminated by a spatially coherent beam that is normally incident on the metal film. Each of the slits will give rise to both forward- and backward scattered light, and surface plasmons that run away from the apertures. Additionally, each aperture will scatter some of the surface-plasmon (SP) intensity that it receives from its partner into various output channels, namely a forward-scattered surface-plasmon, a backward-scattered SP, and scattered light, both towards the source and away from it. Consequently, interference will arise in all scattering channels. A signature of that interference is a modulation of the power measured in any of the output channels when the wavelength of the incident light is changed. By monitoring such modulation spectra one obtains information about the relative strengths of the interfering fields, i.e. of the transmission, reflection and scattering amplitudes and, in principle, also about their phase. While the amplitudes are easy to extract from the experimental data, the phase information often requires precise knowledge of the distance between the apertures that, in many cases, is not available with sufficient precision. Here we show that, by using a well-designed three-slit structure, the missing phase information can be obtained from a requirement of self-consistency, and is therefore available even when the distance between the various slits is not known with great accuracy.

5.2 Heuristic models

The system that we study here is depicted in Fig. 5.1. The left section forms a double-slit structure, in the section at right the twin slits are intersected by a slanted slit. All slits have a width $\approx \lambda/8$ so that a) their transmission is strongly polarized (see Chapter 6), b) they act as an effective source of surface plasmons for incident light that has a non-negligible polarization component perpendicular to the slit (TM-polarization) and c) their direct transmission is sufficiently small that the amplitudes of the directly transmitted light and the surface plasmon are of the same order of magnitude. In the experimental samples that we study, the double and triple slits are part of a single structure (see Fig. 5.2) so that the parallel slits in both structures are separated by the same distance d . In the case that we consider here the slit separation d is much smaller than the surface-plasmon amplitude damping length $L_{\text{sp}} = 1/k_{\text{sp}}'' = 1/\text{Im}(k_{\text{sp}})$.

In the experiment we image the light that is transmitted by the slit structure. The signal that we then record on a specific pixel of our CCD-camera is directly proportional the power that is radiated by the corresponding point in the slit structure. Obviously, not all the radiated power is collected by our imaging lens (our source has a sub-wavelength extent in one transverse direction) but we can safely assume that the effect of this loss is equal for all source points. Consequently, we can simply model the measured signal at any point on the CCD as the square modulus of the local propagating field in the source, i.e., as the square modulus of the transmitted field.

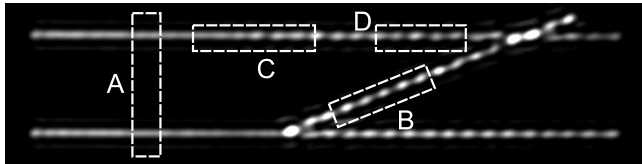


Figure 5.2. Image of one of the slit structures when illuminated by a plane wave at $\lambda = 742$ nm. The various sections that are indicated are discussed in the text.

We use area A to record the transmission of a double slit (see Section 5.2.1) in order to compare it, in Section 5.4.2, with the transmission of the slanted slit (area B, Section 5.2.2) in the three-slit system. Area C shows that the slanted slit acts as a line source of surface plasmons (see Section 5.4.4). By comparing the transmission of the slits in area A with the line-integrated transmission in area D we learn about the tunneling of surface plasmons across a nanoscale

slit. Finally, by analyzing the light transmitted in area D we show that, there, the polarization of the light is space variant.

5.2.1 Two-slit system

Let us first examine the two-slit part of our slit system (part A in Fig. 5.2). When illuminated by light that is polarized at an angle θ with respect to the x -axis, the transmitted field E_{slit} and detected signal S_{slit} can be written as (see Chapter 2, [61]):

$$E_{\text{slit}} \sim (1 + \alpha \exp[i(k_{\text{sp}}d + \phi_c)]) \cos \theta, \quad (5.2)$$

$$S_{\text{slit}} \sim (1 + \alpha^2 + 2\alpha \cos[k_{\text{sp}}d + \phi_c]) \cos^2 \theta, \quad (5.3)$$

where the factor 1 represents the light that is directly transmitted by the slit, $\alpha \exp(i\phi_c)$ the light-SP-light coupling coefficient and k_{sp} the SP propagation constant (see Eq. (5.1)). Here we assume that the field directly transmitted by the slit and that which has been scattered into a plasmon, are reduced by the same factor $\cos \theta$ when the polarization of the incident light is changed. We further assume that we can disregard the effects due to the back-scattering of surface plasmons off the slits that are discussed in Chapter 4. Equation (5.3) predicts a sinusoidal modulation of the detected signal as a function of the surface-plasmon wave vector k_{sp} (see Chapter 2). Calculations based on rigorous diffraction theory suggest that $\phi_c = \pi$ [61, 90].

5.2.2 Three-slit system

The light emitted by the slanted slit in the three-slit system originates from three sources, namely, light that is directly transmitted by that slit, and two surface plasmons, launched by the two parallel slits. The amplitude of the field emitted by the slanted slit can therefore be written as:

$$E_{\text{slanted}} \sim \cos(\theta - \psi) + (\alpha' \exp[i(k_{\text{sp}}x + \phi_c)] + \alpha' \exp[i(k_{\text{sp}}(d - x) + \phi_c)]) \cos \theta, \quad (5.4)$$

so that the detected signal becomes

$$\begin{aligned} S_{\text{slanted}} &\sim \underbrace{\cos^2(\theta - \psi) + 2\alpha'^2 \cos^2 \theta}_{\text{}} \\ &+ \underbrace{4\alpha' \cos(\theta - \psi) \cos \left[\frac{k_{\text{sp}}d}{2} + \phi_c \right] \cos \left[k_{\text{sp}} \left(x - \frac{d}{2} \right) \right] \cos \theta}_{\text{}} \\ &+ \underbrace{2\alpha'^2 \cos \left[2k_{\text{sp}} \left(x - \frac{d}{2} \right) \right] \cos^2 \theta}_{\text{}}. \end{aligned} \quad (5.5)$$

Again θ measures the angle between the polarization direction of the incident light and the x -axis, and $\alpha' = \alpha \cos \psi$. We assume that the amplitude for the scattering from a surface plasmon to a propagating light field by a slit is proportional to $\vec{k}_{\text{sp}} \cdot \vec{n} = \cos \psi$ with \vec{n} the in-plane normal to the slit. Here ψ is the angle subtended by the horizontal and slanted slits (see Fig. 5.1).

The terms contained in the first brace form a wavelength-independent background term; the term in the second brace (proportional to α') represents the interference between light directly transmitted by the slanted slit and the surface plasmons launched by the slits at the top and bottom, while the term in the third brace (proportional to α'^2) originates from the interference between the two counterpropagating plasmons launched by the top and bottom slits. The term due to the interference between transmitted light and surface plasmons has a spatial period equal to λ_{sp} , while the plasmon-plasmon interference term has a spatial period of $\lambda_{\text{sp}}/2$.

SP-SP interference

Because the plasmon strength is small ($\alpha \simeq 0.2$, see Chapter 4) the SP-SP interference, being proportional to α^2 will be difficult to observe. Fortunately, however, the term describing the light-SP interference can be made to vanish by tuning the wavelength of the incident light so that $\cos[k_{\text{sp}}d/2 + \phi_c] = 0$. At that wavelength it should be possible to observe the SP-SP interference, i.e., observe a surface-plasmon standing wave. One may argue that even under these circumstances it will be difficult to observe this high-spatial frequency intensity modulation, being at the limit of what can be observed using far-field techniques such as imaging. The trick lies in the fact that the slit is slanted so that the measured spatial pattern has a periodicity of $\lambda_{\text{sp}}/(2 \sin \psi)$, where ψ is the angle subtended by the parallel slits and the slanted slit.

At exactly this wavelength the signal coming from region A of our structure can be written as:

$$S_{\text{slit}} \sim (1 + \alpha^2 - 2\alpha \cos \phi_c) \cos^2 \theta, \quad (5.6)$$

so that this signal is *minimal* when $\phi_c = 0$, and *maximal* when $\phi_c = \pi$. Obviously, the value of ϕ_c is not limited to being an integer multiple of π ; all values are, in principle, allowed.

Interestingly, we see that we have gained access to hitherto inaccessible information on the scattering phase ϕ_c by a simple correlation measurement: the wavelength is tuned so that the light-SP interference in the slanted slit system vanishes and one observes the signal from the neighboring two-slit structure.

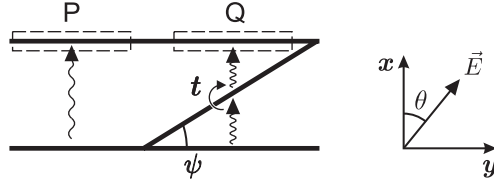


Figure 5.3. Setup for measuring the surface-plasmon tunneling amplitude t . Sections P and Q define the areas over which the signal should be integrated.

SP Tunneling

The images that we record also contain information on the *tunneling* of a surface plasmon across a slit, in our case the slanted slit. That information can be extracted by studying the signal, integrated along two sections of either the top or bottom slit (see Fig. 5.3), as a function of the wavelength of the incident light.

While the signal in section P is independent of the coordinate y , the signal in section Q is modulated due to the interference of the light transpiring through the top slit and the surface plasmon that is launched by the slanted slit (see Section 5.4.4). By integrating over a sufficiently large length of slit this interference pattern is washed out. Then we are no longer sensitive to the SP launched by the slanted slit. Alternatively, one can choose the polarization of the incident light to be parallel to the slanted slit ($\theta = \pi/2 - \psi$); in that case the slanted slit does not emit surface plasmons. The latter approach has a drawback in that the surface plasmons launched by the horizontal slits have a small amplitude (proportional to $\sin \psi$).

Assuming the incident light to be x -polarized, i.e., $\theta = 0$ we can write the y -averaged field amplitudes in sections P and Q as:

$$\bar{E}_P \sim 1 + \alpha \exp[i(k_{\text{sp}}d + \phi_c)], \quad (5.7)$$

$$\bar{E}_Q \sim 1 + t\alpha \exp[i(k_{\text{sp}}d + \phi_c + \phi_t)], \quad (5.8)$$

where $\tilde{t} = t \exp(i\phi_t)$ is the surface-plasmon tunneling coefficient. The section-averaged signals can then be written as:

$$\bar{S}_P \sim 1 + \alpha^2 + 2\alpha \cos[k_{\text{sp}}d + \phi_c], \quad (5.9)$$

$$\bar{S}_Q \sim 1 + (t\alpha)^2 + 2t\alpha \cos[k_{\text{sp}}d + \phi_c + \phi_t]. \quad (5.10)$$

When the signals are measured as a function of the wavelength of the incident light, the signal from both sections P and Q will vary sinusoidally

with a visibility equal to:

$$\mathcal{V}_P = \frac{2\alpha}{1 + \alpha^2} \simeq 2\alpha, \quad (5.11)$$

$$\mathcal{V}_Q = \frac{2t\alpha}{1 + (t\alpha)^2} \simeq 2t\alpha, \quad (5.12)$$

since $\alpha^2 \ll 1$. The ratio of the visibility of the spectrum in sections P and Q is a direct measure of the tunneling amplitude t . The value of the tunneling phase ϕ_t can be extracted from the shift in wavelength of the two spectra.

5.3 Experimental setup

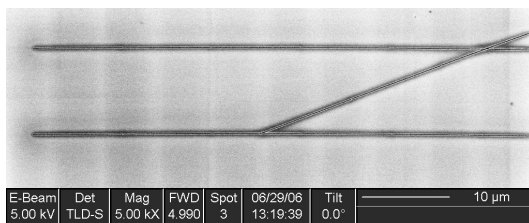


Figure 5.4. A SEM image of the sample.

Our sample consists of a 200 nm thick Au film sputtered on top of a ~ 10 nm thick Cr layer that adheres to a 0.5 mm thick glass substrate. Slits of 100 nm width are milled into this gold film with the help of a focussed-ion beam [52]. An image of a typical structure milled into the film, recorded with a scanning-electron microscope, is shown in Fig. 5.4. One sees two $60 \mu\text{m}$ long parallel slits, separated by a distance of $10 \mu\text{m}$, and a third slit that intersects the other two at an angle of approximately 20° .

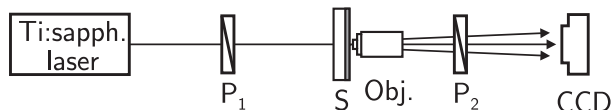


Figure 5.5. Experimental setup.

This structure is illuminated from the glass side by the unfocussed output beam of a Ti:Sapphire laser (Coherent, model 899), that is wavelength tunable

between 740 nm and 830 nm (see Fig. 5.5). The light that emerges from the metal nano-structure is collected by an oil-immersion microscope objective (100 \times magnification, 1.25 N.A.) and imaged on a CCD camera (Apogee, Alta U1). Due to the immersion oil on top of the gold film the surface-plasmon wavelength $\lambda_{\text{sp}} = 2\pi/k_{\text{sp}}$ at a particular frequency ω is much smaller than the free-space wavelength $2\pi c/\omega$, approximately being equal to $2\pi c/(n\omega)$, with n the oil's refractive index. Using the tabulated values of the complex refractive index of gold [53] ($\epsilon_{\text{Au}} = -24.61 + 1.76i$ at $\lambda = 785$ nm) and the published value of the oil's refractive index ($n = 1.51$) we find $\lambda_{\text{sp}} = 494$ nm when the wavelength of the incident light is 785 nm. The sample is surrounded by two polarizers; the one upstream from the sample allows us to choose the polarization of the incident light. The polarizer that is positioned downstream from the sample allows us to do an elementary polarization analysis of the light transmitted by the sample.

In the current experiment it is important that the slits are sufficiently narrow to be almost completely opaque for incident light that is TE-polarized, that is, polarized in a direction parallel to the slits. For that reason we favor 100 nm wide slits (see Chapter 6). Because of the peculiar shape of the milled structure (see Fig. 5.4) some part of the structure will transmit a non-negligible amount of light, whatever the (uniform) polarization of the incident light may be. Note that this also implies that surface plasmons will come into play for any input polarization.

5.4 Results and Discussion

Figure 5.6 shows a series of images of the three-slit part of our sample at incident wavelengths equal to, from top to bottom, $\lambda_{\text{inc}} = 785$ nm, $\lambda_{\text{inc}} = 805$ nm and $\lambda_{\text{inc}} = 532$ nm, respectively. In all of these images the incident light is vertically polarized (see Fig. 5.1), i.e., perpendicular to the horizontal slits. One immediately notices the different modulation patterns in these three images, particularly along the slanted slit. The bottom image, obtained with incident light at a wavelength of 532 nm shows no modulation at all, simply as a consequence that surface plasmons on the gold-oil interface are very strongly damped at this wavelength ($\text{Im}(k_{\text{sp}}) = 1.7 \mu\text{m}^{-1}$ at $\lambda = 532$ nm). The other two images show quite similar patterns along the horizontal slits but different patterns along the slanted slit. We will discuss these differences in more detail below. Note that, in the image in the center ($\lambda_{\text{inc}} = 785$ nm) we had to overexpose the horizontal slits in order to record the pattern along the slanted slit with sufficient signal to noise.

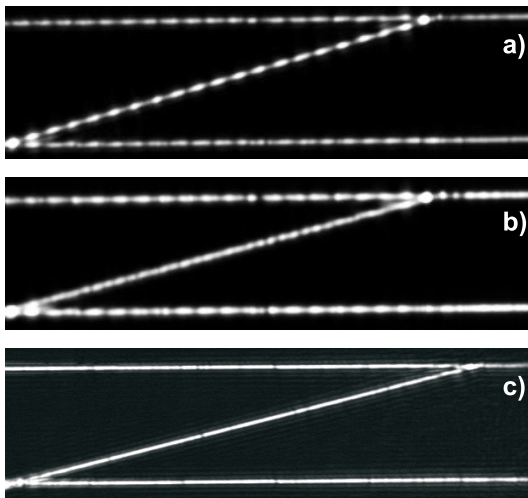


Figure 5.6. Images of the three-slit part of our slit system, obtained with vertically polarized incident light at $\lambda_{\text{inc}} = 785$ nm (frame a); $\lambda_{\text{inc}} = 805$ nm (frame b); $\lambda_{\text{inc}} = 532$ nm (frame c). The center image is overexposed along the horizontal slits to bring out the weak modulation along the slanted slit with sufficient signal to noise.

5.4.1 Signal modulation along the slanted slit

A cross section of the measured signal along the slanted slit is shown in Fig. 5.7a and Fig. 5.7b for $\lambda_{\text{inc}} = 785$ nm and $\lambda_{\text{inc}} = 805$ nm, respectively. In frame a) we see a modulation pattern containing $\simeq 20$ maxima separated by $\approx 2.9 \mu\text{m}$. Projected upon the x -axis we find a modulation period of ≈ 500 nm, which fits well with the calculated value (494 nm). A Fourier transform of the pattern along the slit (frame c) confirms that it is characterized by just one spatial frequency. The pattern arises because the surface plasmons, launched from the horizontal slits at the top and bottom are scattered by the slanted slit into transmitted light and interfere, at that slit, with the light that is directly transmitted by it. The pattern represents the term proportional to $\cos[k_{\text{sp}}(x - d/2)]$ in Eq. (5.5). In a sense, the slanted slit, together with the light incident on it, provides us here with a tomographic cut through the surface-plasmon wave field at the gold-oil interface. Note, however, that we do not directly probe the field at the interface itself, but that we record the image of that field as generated by our optical setup, i.e., we pass through the far field. The field at the surface itself has recently been carefully studied using near-field techniques, in the context of a fiery debate on the nature of the surface wave [63, 99–103].

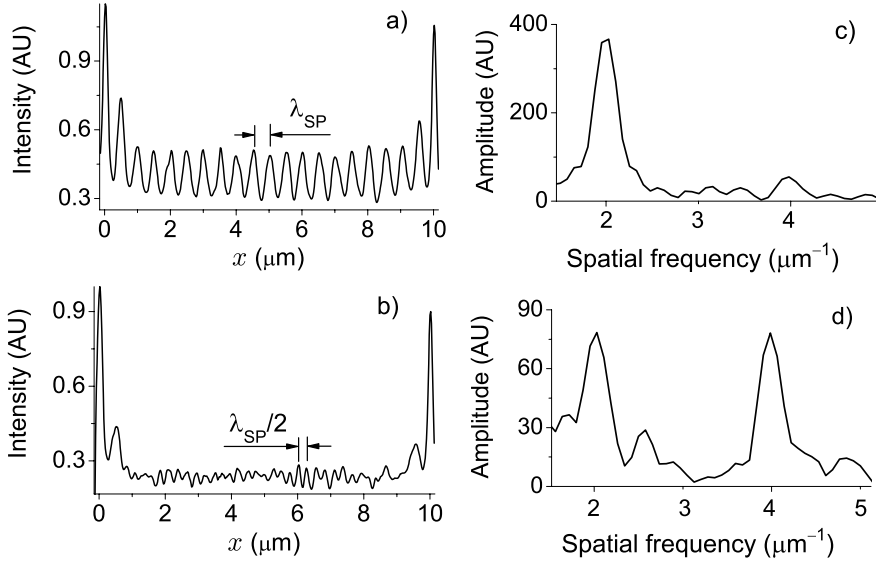


Figure 5.7. Cross-sections of the signal along the probe slit at $\lambda_{\text{inc}} = 785$ (frame a) and 805 nm (frame b), respectively. Frames c) and d) show the corresponding spatial Fourier transforms of the signals along the slit.

For $\lambda_{\text{inc}} = 805$ nm the visibility of the modulation pattern along the slanted slit (frame b) is much reduced. This pattern carries two modulation frequencies: $k_1/(2\pi) \approx 2 \mu\text{m}^{-1}$ and $k_2/(2\pi) \approx 4 \mu\text{m}^{-1}$, as shown in frame d). The low-frequency component of this spectrum has just been discussed and its presence is inadvertent. The high-frequency component comes about as a result of the interference of two counterpropagating surface plasmons between the slits; it corresponds to the last term in Eq. (5.5).

When the light incident on our multi-slit structure is vertically polarized, the pattern of Fig. 5.7b arises only at specific wavelengths, namely when $\cos(k_{\text{sp}}d/2 + \phi_c) = 0$. However, when the polarization of the incident light is chosen to be *parallel* to the slanted slit this pattern appears for *any* wavelength of the incident light for which surface plasmons are supported by the gold-oil interface and are not too heavily damped. At this polarization the slanted slit (being only 100 nm wide) does not directly transmit the incident light ($\cos(\theta - \psi) = 0$ in Eq. (5.5)) so that the SP-SP interference pattern corresponding to the term $\cos[2k_{\text{sp}}(x - d/2)]$ in Eq. (5.5) can be observed.

Figures 5.7a and 5.7b show that, whatever the wavelength of the incident light, the signal rapidly rises near the end points of the slanted slit (at $x = 0 \mu\text{m}$

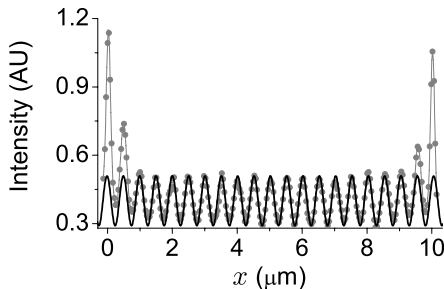


Figure 5.8. The data of Fig. 5.7a (grey curve) with a simple sinusoidal function (black curve) superposed. The excellent correspondence of the position of the maxima of the two curves indicates that our experimental data can be described by a single spatial frequency.

and $x = 10 \mu\text{m}$). There the slanted slit intersects one of the horizontal slits; we interpret the rapid rise of the signal along the slanted slit as being due to diffraction off the horizontal slits. Careful analysis of the full pattern of Fig. 5.7a shows that the modulation frequency of the pattern is constant along the full length of the slanted slit (see Fig. 5.8). Therefore, the rise of the signal near the horizontal slits does not herald the presence of an additional surface wave [51].

5.4.2 Coupling phase slip

In the two-step process, where incident light is first scattered at one slit into a surface plasmon which then is back-converted to light at the other slit, the total phase accrued can be written as [61]:

$$\Delta\Phi = k_{\text{sp}}d + \phi_c, \quad (5.13)$$

where d is the distance between the two slits and ϕ_c represents an additional phase slip. Numerical studies based on rigorous diffraction theory or a Green's function formalism predict that $\phi_c = \pi$ [61, 90]; so far this theoretical prediction has not been verified in an experiment.

It would appear to be quite simple to experimentally verify this prediction, for instance by using the spectral modulation technique of Chapter 2. However, in order to find a reasonably exact value for ϕ_c the inaccuracy in $k_{\text{sp}}d$ should be sufficiently small, but the slit separation d and the surface-plasmon wave vector k_{sp} are usually not precisely determined. The lack in precision in the experimental value of d ($\approx 0.2 \mu\text{m}$) stems from calibration inaccuracies

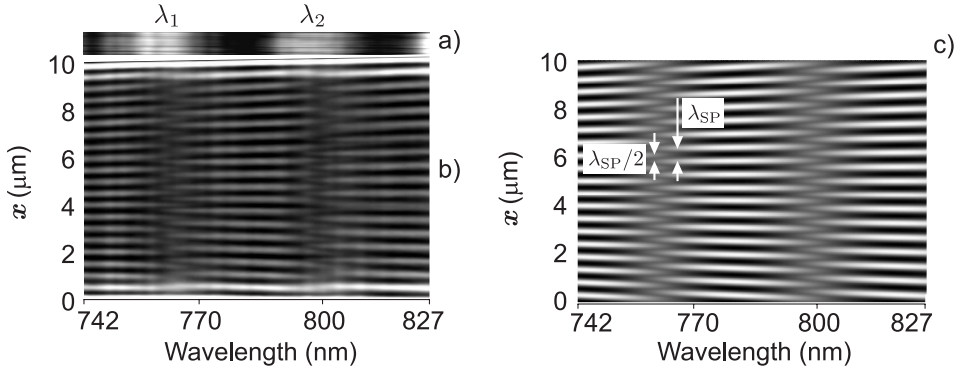


Figure 5.9. At left: Experimental data for the two-slit part of our sample (frame a) and the three-slit part (frame b), as a function of the wavelength of the incident radiation. The two-slit *maxima* occur at wavelengths $\lambda_1 = 760$ nm and $\lambda_2 = 796$ nm where the signal along the slanted slit shows a doubling of the spatial frequency. At right: calculated signal along the slanted slit according to Eq. (5.5) using $\phi_c = \pi$.

of the scanning-electron microscopes used by us, while the imprecision in k_{sp} stems from the fact that the dielectric coefficients of the gold film may not be equal to the published values [22, 53] and from the fact that Eq. (5.1) applies to an infinitely extending perfectly flat interface, which is not the case in the vicinity of our slits.

As discussed in section 5.2.2 our composite slit provides us with an opportunity to determine the phase slip ϕ_c without knowing the exact separation of the slits, by comparing the signal transmitted by the two-slit part with the pattern along the slanted slit in the three-slit part. The results of that experiment for the wavelength interval 742–827 nm are shown in the left frame of Fig. 5.9. The signal in the two-slit section (frame a) has maxima at $\lambda_{\text{inc}} = 760$ nm and $\lambda_{\text{inc}} = 796$ nm, exactly at those wavelengths where the signal along the slanted slit is rather low (frame b) and where it has twice the number of maxima as compared to the signal at other wavelengths. Frame c) displays the fringe structure along the slanted slit according to Eq (5.5) using $\phi_c = \pi$. The experimental and calculated fringe structures are in excellent agreement.

Whenever the signal in the two-slit section is maximum we have (see Eq. (5.3)):

$$k_{\text{sp}}d + \phi_c = 2\pi m, \quad (5.14)$$

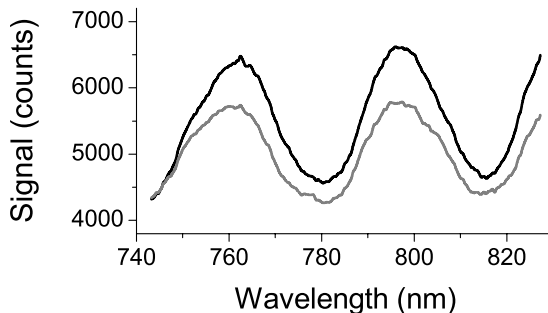


Figure 5.10. Transmission spectrum of the top slit of the two-slit section (black curve) and the top slit of the three-slit section (grey curve).

while the disappearance of the interference between the surface-plasmon and the incident light indicates that (see Eq. (5.5))

$$\frac{k_{\text{sp}}d}{2} + \phi_c = \pi/2 + 2\pi m'. \quad (5.15)$$

Here m and m' are integers. Together, these relations yield:

$$\phi_c = \pi + 2\pi q, \quad (5.16)$$

where q is integer-valued.

5.4.3 Plasmon tunneling

As discussed in Section 5.2 the surface-plasmon tunneling amplitude and phase can also be extracted from a comparison of the signals transmitted by the two-slit and three-slit parts of our sample. However, we now focus on the spatial average of the signal along the horizontal slits in the two- and three-slit sections, respectively. The experimental results are shown in Fig. 5.10 where the black curve displays the results for the two-slit section (section P in Fig. 5.3) and the grey curve those for the three-slit part (section Q in Fig. 5.3). From these spectra we derive values for the visibility: $\mathcal{V}_P = 0.17$ and $\mathcal{V}_Q = 0.14$. Using Eqns. (5.11) and (5.12) we find the tunneling amplitude $t \simeq 0.8$. By noting that the two spectra are well aligned we find that the tunneling phase shift $\phi_t \approx 0$, in good agreement with the prediction of Janssen *et al.* [90].

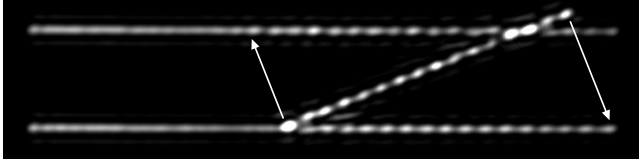


Figure 5.11. Transmitted-light image of a slightly different ion-beam milled sample exhibiting interference fringes in both the horizontal and slanted slits. The arrows indicate the propagation directions of the plane-wave surface plasmons emitted by the slanted slit.

5.4.4 Slanted slit as a source of surface plasmons

So far we have concentrated on the role of the slanted slit as a “probe” of the surface-plasmon field, generated by the two parallel slits. That, of course, is a simplification since the slanted slit will, in general, also emit surface plasmons. This is most easily seen by noting that the signal along the parallel slits is modulated in a manner similar to the signal along the slanted slit (see Fig. 5.11). One can easily show that the spatial frequency of the signal along the horizontal slit is equal to $k = k_{\text{sp}} \sin \psi$, with ψ the angle subtended by the slanted and horizontal slits. The length of the interference pattern along the horizontal slits indicates that the surface plasmon launched by the slanted slit propagates as a plane wave along the interface.

This being said, one may ask whether the signal along the slanted slit may be affected by the surface plasmons emitted by this same slit after reflection from the two horizontal slits. For vertically polarized incident light one may argue that the amplitude of the light field transpiring through the slanted slit as a result of such a reflected plasmon is proportional to $\alpha|r| \cos \psi \sin 2\psi$, with $|r|^2$ the surface-plasmon reflection probability, which we have assumed to be independent of the angle of incidence (of the surface plasmon on a slit). For $\psi \approx 10^\circ$ as in the present experiment and $|r| \simeq \alpha$ (see Chapter 4) we get $\alpha|r| \cos \psi \sin 2\psi = 0.33\alpha^2$, a factor 6 smaller than the SP-SP interference effect discussed before. Therefore we can safely ignore these reflections.

If we choose the incident light to be y -polarized, the horizontal slits will transmit a very small fraction of the incident light although the frequency of the incident light is well beyond cut-off (slit width $\approx \lambda/8$, see Chapter 6). The surface plasmons, generated at the slanted slit (with low efficiency because the incident light is polarized almost parallel to this slit) will propagate towards the horizontal slits and will be partially scattered there into vertically polarized light. So the light emanating from the horizontal slits will have both vertically (due to SPs) and horizontally (due to tunneling) polarized components. The

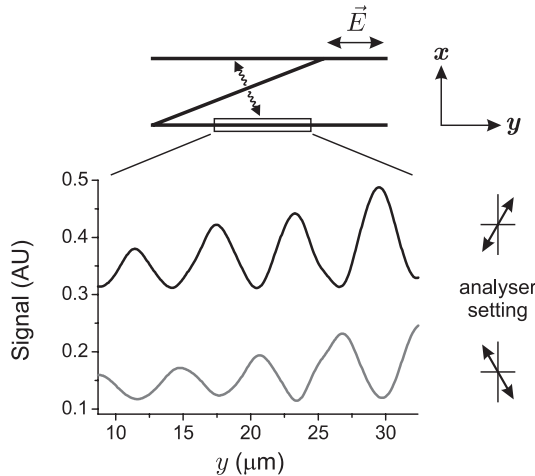


Figure 5.12. Experimental arrangement for observing a plasmon-induced space-variant polarization. The incident light is polarized parallel to the horizontal slits, which are sufficiently wide to be slightly transmitting. Surface plasmons launched by the slanted slit generate light at the horizontal slit that is vertically polarized. The two curves at the bottom show the space-dependent signal as transmitted by a uniform polarizer, for two settings of the polarizer transmission axis. The upper black curve is manually off-set from the grey curve for distinction.

phase difference between these components depends on the position along the horizontal slit because the vertically polarized component has its source in the slanted slit. We therefore expect the polarization to be space-variant along the horizontal slits.

We have studied this effect using a three-slit structure with somewhat wider slits (200 nm instead of 100 nm) and a more acute angle between the slanted and horizontal slits ($\approx 5^\circ$ instead of $\approx 10^\circ$). The results are shown in Fig. 5.12, where, in addition to a sketch of the slit structure, we show the spatial modulation of the signal along the bottom horizontal slit for two orientations of the analyzing polarizer that is positioned in front of our CCD-camera.

First, we note that the *amplitude* of the vertically and horizontally polarized components of the light coming out of the bottom slit should only weakly depend on the coordinate y . Their relative *phase*, however, will be a linear function of y , because of the angle subtended by the slanted and horizontal slits. Where the phase difference $\delta\phi = m\pi$, with m an integer, the output polarization will be linear. There are two sets of points where this is the case:

those where m is even (the vertically and horizontally polarized components are in phase) and those with m odd, where the vertically and horizontally polarized components are π out of phase. We can now orient the analyzing polarizer so that it extinguishes the light coming from those points where m is even, or those where m is odd. When the analyzer is oriented so that the even m points are extinguished, the points where m is odd will be bright, and when the analyzer is oriented so that the m is odd points are extinguished, the even m points will be bright. Both cases are shown in Fig. 5.12. In this experiment the polarization of the incident light is chosen so that the space-variant effect is most easily observed. In our configuration with differently oriented slits this effect occurs for any polarization of the incident light, but it may be difficult to observe in the most general case.

5.5 Conclusions

By using simple two- and three-slit structures milled in a gold metal film we have been able to directly measure the phase associated with the double-scattering process where incident light is converted into a surface plasmon in a sub-wavelength slit and back-converted to light in a neighboring slit. We have found this phase to be $\pi \pm 5\%$, in good agreement with predictions based on rigorous diffraction theory.

These structures also allow us to measure the amplitude and phase of the process where a surface plasmon tunnels across a sub-wavelength slit in a gold metal film. Finally, we have shown that the polarization of the light transmitted by such a structure can be space variant.

5.6 Appendix: Towards a complete picture of surface-plasmon scattering (unpublished)

The scattering of light and surface plasmons at a sub-wavelength slit is one of the central issues discussed in this thesis. By using various experimental techniques we have determined the scattering phase of the process (see Fig. 5.13)

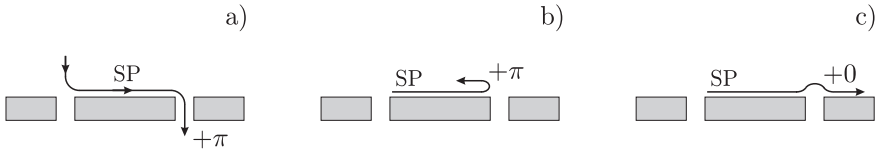


Figure 5.13. Scattering processes of light and surface plasmons.

- a) where a wave incident from free space scatters into a surface plasmon and re-scatters into a propagating mode of the slit; this phase is equal to π (mod. 2π).
- b) where a surface plasmon, incident on such a slit is back-scattered into a surface plasmon; this phase is equal to π (mod. 2π).
- c) where a surface plasmon “jumps over” a slit; this phase is equal to 0 (mod. 2π).

The wavelengths where constructive or destructive interference occurs in the various scattering channels are determined by these phase factors, in addition to the propagation phase $k'd$ (with k' the real part of the surface-plasmon wave vector k_{SP} and d the distance between the slits).

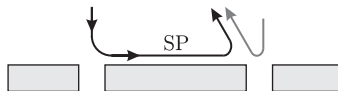


Figure 5.14. One-step and two-step scattering processes that give rise to interference in back-scattering. The two-step process has a surface plasmon as an intermediate state.

So far, we have neglected one important scattering process and thus one additional channel where interference can occur. This channel regards the *direct back-scattering of light off the slit*. The so scattered light interferes with light that originates at the other slit, is scattered into a plasmon, and is re-scattered into light (see Fig. 5.14).

A priori, it is not known how the interference in the back-scattered light relates to that in the transmitted channel, that is, whether the interference features in transmission and back-scattering are in phase, π out of phase, or something else. Figure 5.15 shows the result of an experiment. The back-scattered light is collected over a wide range of back-scatter angles; it does not contain the light that is directly reflected by the metal.

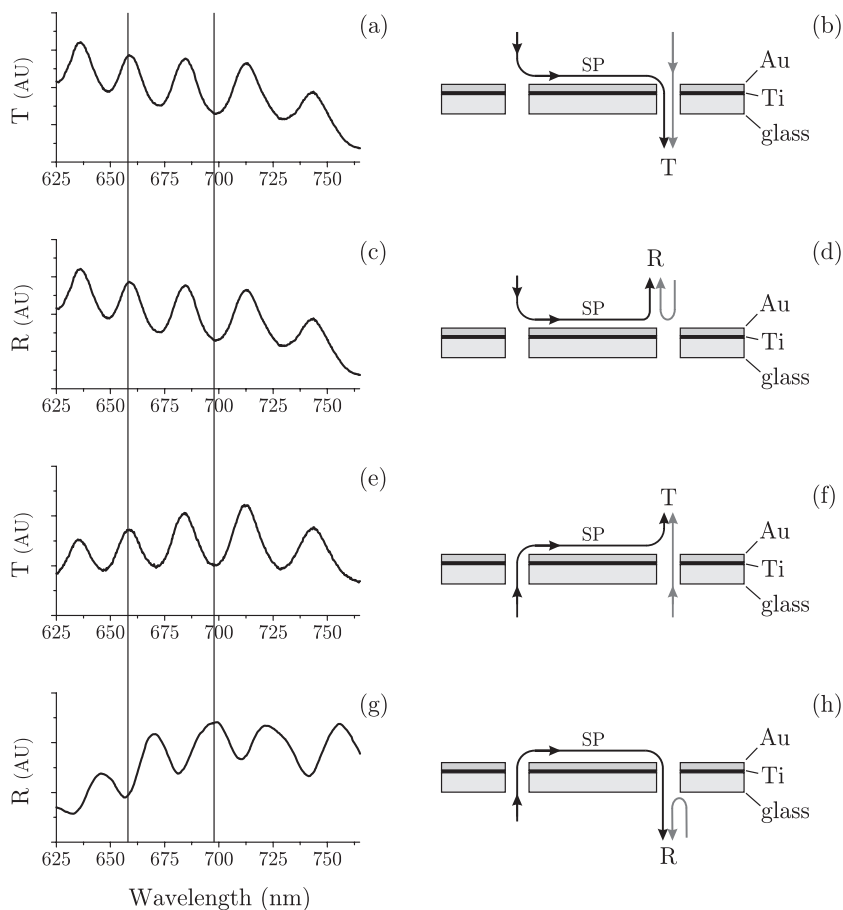


Figure 5.15. Spectra of transmitted light (a and e) and back-scattered light (c and g), with light incident on the metallic side of the sample (a and c), and on the glass side of the sample (e and g). For each of the spectra on the left, the diagrams on the right indicate the paths that interfere. Note the stacking of the materials in the sample; the 10 nm thin titanium layer between the gold and the glass serves two purposes. It acts as an adhesion layer for the gold and serves to rapidly damp the surface plasmons that are launched at the glass/gold interface.

Evidently, when the light is incident on the metallic side of the sample, the transmission and “reflection” spectra are very similar. However, when the light is incident on the glass side of the sample the transmission and “reflection” spectra have a phase difference that varies somewhat with wavelength, being $\approx \pi$. Note, that the experimental results show that the “reflection” spectra depend on the orientation of the sample, i.e, the side of the sample that is turned towards the light source matters. Violation of reciprocity is not at stake here because the system is not loss-free.

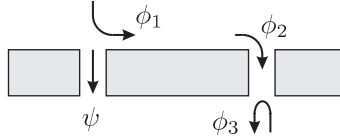


Figure 5.16. Nontrivial phase shifts for various scattering processes at sub-wavelength slits in thin metal films.

The collected experimental results induce us to present a heuristic model of the scattering of light and surface plasmons at sub-wavelength slits (see Fig. 5.16). This model is based on the following assumptions:

- A nontrivial phase shift of ϕ_1 is associated with the process where light, incident from free space, is scattered into a surface plasmon. The same phase shift occurs when a surface plasmon is scattered into free space.
- A nontrivial phase shift of ϕ_2 is associated with the process where light, propagating as a slit mode, scatters into a surface plasmon. The identical phase shift occurs when a surface plasmon is scattered into a slit mode.
- When a free-space mode is incident on a slit and is back-scattered, it accrues a nontrivial phase shift due to Fresnel reflection equal to ϕ_3 , with $|\phi_3| = \pi$.
- When light propagates as a slit mode it acquires a phase $\psi = k_0 n_z t$. Here t is the film thickness (the length of the waveguide), n_z the effective mode index, and $k_0 = \omega/c$ the free-space wave vector of the incident light. For the sample under investigation (see Chapter 6) we have $\psi \simeq \pi/2$.

We can now associate the following phase differences with the interfering paths in Fig. 5.15. From previous measurements (Chapter 5) we know that $\phi_1 + \phi_2 = \pi$ and that $\phi_3 = \pi$. The experiment of Fig. 5.15 shows that $\Delta\Phi_1 = \Delta\Phi_2$ so that

$$|\phi_1 - \phi_2| = |\phi_3| = \pi. \quad (5.17)$$

Pathway	Frame	Relative phase
Transmission	b, f	$\Delta\Phi_1 = k'd + \phi_1 + \phi_2$
Reflection in air	d	$\Delta\Phi_2 = k'd + 2\phi_1 - \phi_3$
Reflection in glass	h	$\Delta\Phi_3 = k'd + 2\phi_2 - \phi_3 + 2\psi$

Table 5.1. Phase differences for various interfering pathways in Fig. 5.15.

From the “reflection in glass” spectrum we deduce that

$$|2\phi_2 - \phi_3| = \pi. \quad (5.18)$$

Since $|\phi_3| = \pi$ we have $|\phi_2| = \pi$ or $\phi_2 = 0$, all modulo 2π . Combining with Eq. (5.17) yields the following combinations:

$$|\phi_1| = \pi \quad |\phi_2| = 0 \quad |\phi_3| = \pi, \quad (5.19)$$

$$|\phi_1| = 0 \quad |\phi_2| = \pi \quad |\phi_3| = \pi. \quad (5.20)$$

The first solution is in agreement with the prediction of Ref. [90], the other not.

CHAPTER 6

Retardation effects in sub-wavelength slits in thin metal films near cut-off

We have experimentally studied the transmission properties of a single sub-wavelength-wide slit in a 200 nm thick Au film as a function of the slit width, for both TE and TM polarizations. Contrary to the standard waveguide model for an ideal metal that predicts a cut-off for the TE mode at a slit width equal to $b = \lambda/2$, we find that the transmission for TM and TE polarized incident light is approximately equal at $b = \lambda/4$ ($\lambda = 800$ nm), and that the TE transmission becomes negligible only when $b \simeq \lambda/8$. A polarization analysis of the transmitted light shows that at $b = \lambda/4$ the slit acts as a quarter-wave plate. Calculations based on rigorous diffraction theory are in good agreement with the experimental results.

6.1 Introduction

In 1861 Fizeau described in a remarkable paper his observations on the polarization properties of natural light as it was transmitted through a wedge-shaped scratch in a thin silver film [104]. He discovered that the light transmitted through the narrowest sections of the slit is polarized perpendicular to the slit, while the light transmitted through somewhat wider sections is predominantly polarized parallel to the slit. He compared a whole range of metals, such as gold, brass, tin, iron, etc. and found similar results for all these materials. In his paper Fizeau also presents values for the film thickness (of order 200 nm) and the slit width (of order 100 nm). Fizeau did not have a theoretical framework to explain his results because Maxwell's theory of electromagnetism had not yet been developed.

Sub-wavelength slit apertures in metal screens came back into the focus of attention in the context of the development of radar around the time of the second world war. The polarizing action of such apertures could now be explained in terms of electromagnetic theory, using a description in terms of a waveguide consisting of two plane-parallel metallic sheets [105]. In that model the strong polarizing action of the narrowest slits comes about because these slits allow only one polarization mode to propagate with low loss, while the other is extremely lossy, being evanescent. The development of novel astronomical and spectroscopic techniques in subsequent years provided another push to study this subject but now at optical wavelengths, i.e., on a much smaller spatial scale [106–108]. At these wavelengths ohmic damping in the metal can not be ignored.

The issue of the transmission of very small *circular* holes was discussed by Bethe in a landmark paper in 1944 [37], predicting that the transmission of a hole with radius $a \ll \lambda$ scales as $(a/\lambda)^6$. This work was extended by Bouwkamp [109]; the resulting theoretical model is known as the Bethe-Bouwkamp theory and has played an important role in the development of optical recording techniques [110].

Sub-wavelength apertures in thin metallic films were suddenly rocketed to center stage by the recent observation that a regular (two-dimensional) array of such apertures has a much larger transmission than what one expects based on Bethe's theory [36]. In these studies [72] both the hole diameter and the thicknesses of the metal film are of the order of a few hundred nanometers, smaller than the wavelength of the incident light. The transmission spectrum of such a hole array displays sharp resonances; these resonances vanish when the apertures are arranged in an arbitrary pattern. The standard explanation of these phenomena is that the regular array of holes acts as a grating that couples the

incident field to a surface wave; the latter is scattered to a transmitted wave by the same grating-like structure. The transmission spectrum then carries information about the various gratings that are contained in the hole array while the line shape of an individual resonance reflects the interference between the light that is directly transmitted (in a Bethe-like fashion) by the holes and the channel that involves a surface wave as an intermediary [111, 112]. It is widely accepted that surface plasmon polaritons, henceforth called surface plasmons, are responsible for this effect although this explanation is contested [51]. In these experiments all relevant dimensions (wavelength of incident radiation, hole diameter, film thickness) have sub-micron, i.e., nanometric size. For that reason, it belongs to the field of nano-optics. Similar results, i.e., pronounced spectral signatures, are also obtained for metallic films featuring a single hole surrounded by equidistant circular grooves or a slit surrounded by parallel equidistant trenches [111].

In the experiments on two-dimensional hole arrays the polarization of the incident radiation plays an important role in that it determines the surface-plasmon modes (Bloch waves) that the incident beam can couple to. In a 1D structure, such as a parallel slit array (grating) or a slit surrounded by parallel, equidistant grooves, the polarization of the incident light has a much more pronounced effect. Only when the latter has a component perpendicular to the slits (so-called TM-polarization) does the incident light couple to surface plasmons. When the light is polarized parallel to the slits these surface modes do not come into play. Most of this was known already from the study of the the diffraction properties of metallic gratings [113].

Recent theoretical and experimental work on the transmission of single slits has focussed on slits that have a sub-wavelength width [41, 43, 48, 114]. For TM-polarized incident light these authors predict or observe Fabry-Pérot resonances when the thickness of the metallic screen exceeds $\lambda/(2n_z)$ where n_z is the index of refraction of the metallic waveguide for the TM-polarized mode. The TE-polarized mode has received much less attention and, seemingly, for a good reason. Universally accepted waveguide models predict that a narrow slit does not transmit such a mode when its wavelength is beyond cut-off. For perfect metals the cut-off wavelength equals twice the slit width; for real metals the cut-off wavelength is somewhat larger [56, 115]. All these models predict a rather pronounced resonance in the transmission spectrum of a single slit at a wavelength just before cut-off [116–122].

Our interest in this field was triggered by a series of measurements on sub-wavelength double slits [61]. In these experiments we showed that surface plasmons act to modulate the *spectrum* of such a double slit. In order to argue

that the spectral modulation is indeed due to surface plasmons we used TM-polarized incident light, allowing excitation of these surface modes, and TE-polarized incident light, where surface plasmons can not be excited. It came as a surprise when we measured that the transmittivity of the slits (200 nm wide in a 200 nm thick gold metal film) for incident light at a wavelength of $\simeq 800$ nm was *of the same order of magnitude for both input polarizations*. In view of the fact that the slits were much narrower than the wavelength of the incident radiation ($b/\lambda \simeq 0.25$) the TE-transmission was, naively, expected to be orders of magnitude smaller than that for the TM-polarization. A rigorous theoretical scattering model based on a Green's function approach predicted that the TE-polarized transmission is not negligible but, typically, an order of magnitude smaller than that for the TM polarization [61]. Experiments using similar samples prepared under slightly different conditions confirmed our initial experimental results. Clearly, they could not be attributed to a single anomalous sample.

In a subsequent study we investigated the polarization properties of the double slit or, more accurately, each of the pair of slits. The questions we wanted to address are: i) what is the polarization state of the transmitted light when the polarization of the incident light is purely TE or TM; ii) what is the polarization state of the transmitted light when the incident light is circularly polarized? The results are shown in Fig. 6.1: when the incident light is either TM- or TE-polarized the transmitted light is fully polarized and has the same polarization as the incident light. However, when the incident light is *circularly* polarized the transmitted light is *linearly* polarized at an angle of 45° relative to the TM- and TE-directions in a way similar to a quarter-wave plate. To complete our measurements we also measured the polarization of the transmitted light for incident light polarized at an angle of 45° relative to the TM- and TE-axes, and found it to be circular. The last two observations imply that the attenuation of the TE and TM-polarized components are approximately equal, and that the propagation constants of the TE- and TM-polarized modes in the slits must be quite different to induce a phase slip of $\pi/2$ over a length of just 200 nm. Effectively, we find $|n_{\text{TE}} - n_{\text{TM}}| = 1$. It appears that such a sub-wavelength slit acts as a lossy, non-dichroic, birefringent optical element.

Here we present a systematic study of the polarization properties of the light transmitted by a single sub-wavelength slit of variable width (50–500 nm) milled in a 200 nm thick gold metal film using incident light at a wavelength of $\simeq 800$ nm. We confirm our first observations and explore at what slit widths the TE-mode is really beyond cut-off. We compare our results with numerical

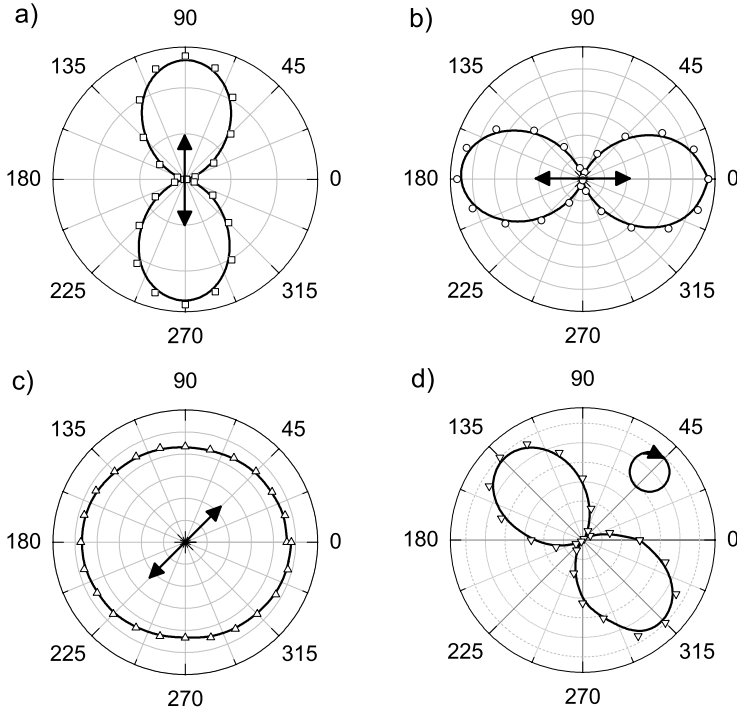


Figure 6.1. Polar plots of the transmission of a single sub-wavelength slit in a thin gold film as a function of the orientation of an analyzing polarisator. The results apply to a 200 nm wide slit milled in a 200 nm thick gold film for incident light at a wavelength of 800 nm. In a) the incident light is TM polarized (perpendicular to the slit axis); in b) it is TE polarized (parallel to the slit axis); in c) it is polarized at an angle of 45° ; in d) it is circularly polarized.

calculations based on rigorous diffraction theory.

6.2 Experiment

In the experiment we analyze the light intensity, transmitted through a 1×10 array of $10 \mu\text{m}$ long and 50–500 nm wide slits, milled in a 200 nm thick gold film. The width of the slits increases stepwise from 50 nm, well below the cut-off width for TE polarized light at $\lambda = 800 \text{ nm}$, to 500 nm, at which value the lowest TE-mode can propagate through the slit. The film is deposited on a 0.5 mm thick D263T borosilicate glass substrate, covered by a 10 nm titanium

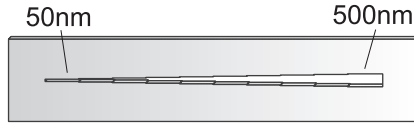


Figure 6.2. Array of sub-wavelength slits.

adhesion layer.

The slits are arranged in a single line (see Fig. 6.2) to simplify the data acquisition: we illuminate all slits in one shot with the beam of a wavelength-tunable ($\lambda \approx 800$ nm). The laser beam has a diameter of ≈ 2 mm at the sample so that the intensity varies only weakly across the composite slit and the laser beam's phase front is approximately flat. An important argument to set the sub-slits along the single line, rather than arranging them in a grating-like way, is that when the surface plasmons are excited by any slit they are not “received” by any other slit.

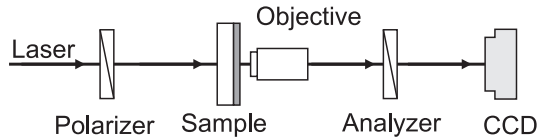


Figure 6.3. Experimental setup. The sample is illuminated from the glass side; the transmitted light is polarization analyzed and imaged on a CCD camera.

The light transmitted by structure is imaged on a CCD camera (Apogee, Alta U1) by means of a 0.65 N.A. microscope objective (Fig. 6.3). The polarization of the light incident on the structure was set to being parallel to the slits (TE polarization), perpendicular to the slits (TM polarization) or at 45° to the slits, containing both TM and TE components.

6.3 Experimental results

We have performed two types of experiments with the array of slits: i) we have measured the total power transmission of all individual slits for the case that the incident light is purely TE- or TM-polarized and ii) we have measured the transmission as a function of the angle of the analyzing polarizer for the case that the incident light is polarized at an angle of 45° relative to the long axis of the slit. The latter measurements provide information on the difference in propagation phase of the TM- and TE-polarized components of the light as it

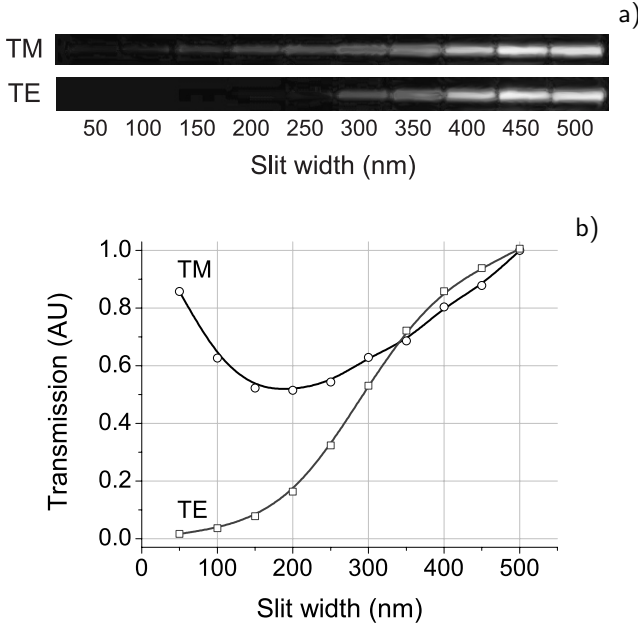


Figure 6.4. a) Slit images for TM or TE illumination; b) Normalized transmittivities ($\lambda = 800$ nm) of TM- or TE-polarized incident light as a function of the slit width. At a slit width of 500 nm the transmission for TE- and TM-polarized incident light at $\lambda = 800$ nm is almost exactly equal. We have, arbitrarily, set the transmission to 1 at this value of the slit width.

propagates through a slit.

6.3.1 Transmission of purely TE/TM polarized incident light.

The recorded images of the slit array for the case that the incident light is either purely TE- or TM- polarized are shown in Fig. 6.4a. It is seen that the TM mode transmits down to the smallest slit width (50 nm) whereas the TE mode essentially becomes opaque when the slit width $b < 250$ nm.

In order to get meaningful results we normalize the signal integrated over the slit, by the slit width. Figure 6.4b shows the normalized transmission data as the function of the slit width. Henceforth, we will discuss the normalized slit transmittivity.

As the slit width is reduced the slit transmission decreases by roughly the same factor for the TE and TM polarizations until $b \simeq 350$ nm. When b is further reduced the normalized TM transmission goes through a minimum at

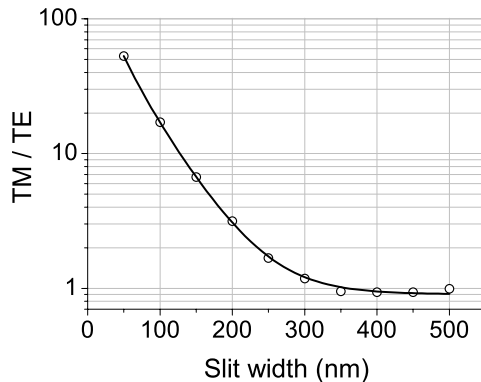


Figure 6.5. TM/TE transmission ratio at $\lambda = 800$ nm of a single sub-wavelength slit, milled in 200 nm thick Au film, as a function of the slit width.

$b \simeq 200$ nm to increase again when b gets even smaller. When we plot the non-normalized transmission power as a function of the slit width we find that power depends linearly on the slit width. Figure 6.4 shows that the normalized TE transmission, however, decreases monotonously. At $b = 50$ nm the TE-transmission is only $\sim 2\%$ of that for the TM polarization. From the data of Figure 6.4b we extract the TM/TE transmission ratio which we plot in Fig. 6.5. Apparently, a narrow slit in a thin metal film is not such a good polarizer as often assumed.

6.3.2 Polarization analysis of transmitted light

To gain a better understanding of the physics associated with the data of Fig. 6.1 we have made a systematic study of the polarization properties of the light transmitted by a sub-wavelength slit as a function of the slit width. We use the array of Fig. 6.2 with normally incident light at $\lambda_{\text{inc}} = 800$ nm, polarized at an angle of 45° relative to the slit. The transmitted light is sent through an analyzing polarizer and is detected as a function of the orientation of this analyzer. The results are shown in Fig. 6.6, in a series of polar plots. As the slit width is reduced from 500 nm to 300 nm the transmitted light gradually becomes more and more elliptically polarized (the minimum transmission increases gradually), while the main axis of the polarization ellipse remains oriented along the polarization direction of the incident light, namely at 45° to the slit. As the slit width is reduced further, the transmitted light becomes more and more linearly polarized, ultimately being purely TM-polarized at

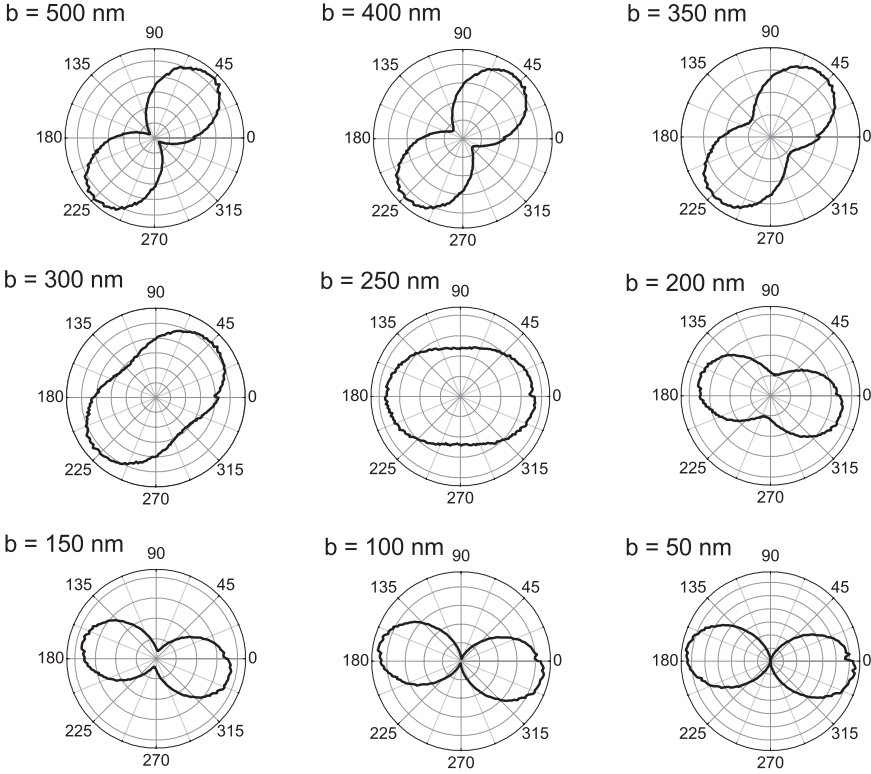


Figure 6.6. Polar diagrams of the measured signal as a function of the orientation of the analyzing polariser.

$b = 50$ nm.

The directions parallel and perpendicular to the slit are its eigenpolarizations, each with its own damping and propagation constant. In a general case such a slit is therefore both dichroic and birefringent, both properties depending on the ratio b/λ . The effect that we observe as the slit width is decreased from 500 to 300 nm can be explained in terms of an increasing birefringence and negligible dichroism. At $b = 250$ nm, the main axis of the polarization ellipse is rotated, pointing in a direction that is almost perpendicular to the slit. This sudden change is due to the fact that, at $b = 250$ nm, dichroism has become important, as already evident from Fig. 6.5. If the slit width is further decreased, the dichroic effect becomes even larger (see Fig. 6.5). The TE-polarized component of the transmitted light becomes weaker and weaker causing the polar diagram to collapse to a \cos^2 pattern. Note that in the

present experiment we do not generate purely circularly polarized light as in the experiment of Fig. 6.1. We attribute this to the use of a different sample with slightly different properties.

In order to extract the phase lag $\Delta\phi$ between the TE- and TM-polarized components of the transmitted field we write the incident field as:

$$\mathbf{E}_{\text{in}} = \begin{pmatrix} E_{\text{TM}} \\ E_{\text{TE}} \end{pmatrix} = \begin{pmatrix} 1 \\ 1 \end{pmatrix}. \quad (6.1)$$

The amplitude-transmission through the slit can be represented by the matrix:

$$\mathbf{T} = \begin{pmatrix} t_{\text{TM}} e^{i\Delta\phi} & 0 \\ 0 & t_{\text{TE}} \end{pmatrix}, \quad (6.2)$$

while the action of the analyzing polarizer, oriented at an angle ψ , is given by:

$$\mathbf{P} = \begin{pmatrix} \cos \psi \\ \sin \psi \end{pmatrix}. \quad (6.3)$$

The amplitude of the transmitted field can be written as:

$$|E_{\text{out}}| = \mathbf{P}^T \mathbf{T} \mathbf{E}_{\text{in}} = t_{\text{TM}} e^{i\Delta\phi} \cos \psi + t_{\text{TE}} \sin \psi, \quad (6.4)$$

so that the signal measured by the detector can be written as:

$$S_{\text{out}} \propto t_{\text{TM}}^2 \cos^2 \psi + t_{\text{TE}}^2 \sin^2 \psi + t_{\text{TM}} t_{\text{TE}} \sin 2\psi \cos \Delta\phi. \quad (6.5)$$

Using the ratio $(t_{\text{TM}}/t_{\text{TE}})^2$ as measured in our transmission experiment (see Fig. 6.5) we fit the experimental data of Fig 6.6 with Eq. (6.5) taking $\Delta\phi$ as a fitting parameter. The results of a fit for the 250 nm wide slit are shown in Fig. 6.7a.

Figure 6.7b shows that the phase difference $\Delta\phi$ decreases almost linearly with increasing slit width, and so does the effective birefringence $|n_{\text{TE}} - n_{\text{TM}}|$ of the slit. The phase difference passes through a value of $\pi/2$ at $b = 250$ nm. For that slit width, however, the transmitted light is *not* circularly polarized, due to the unequal amplitudes of the TE- and TM-polarized components. Although different in the details, the results obtained with the array of slits (Figs. 6.4–6.7) fully support the initial results of Fig. 6.1. Being able to generate circularly polarized light with sub-wavelength wide slits, requires careful tuning of all slit parameters and of the incident wavelength. It is a matter of serendipity that we found those conditions in our first experiment.

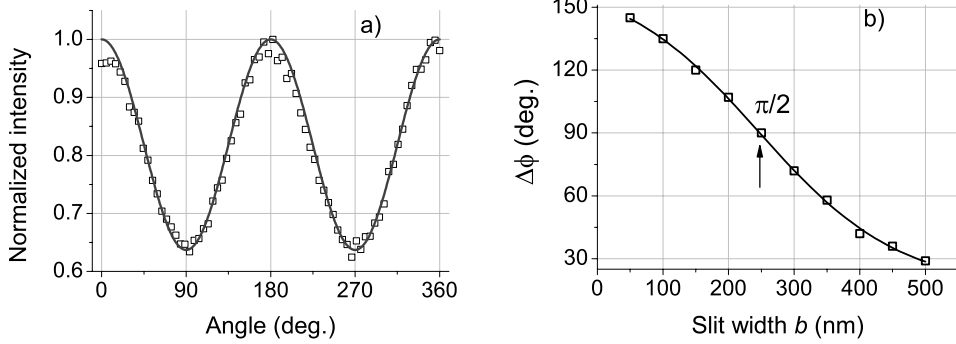


Figure 6.7. a) Example of fitting of experimental data points for the 250 nm wide slit (squares) with the model (solid line); b) Phase difference of TM and TE modes for the 200 nm deep slits as a function of slit width. The data points (squares) are obtained from a fit of the various curves of Fig. 6.6. The solid line serves to guide the eye.

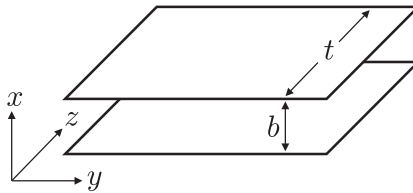


Figure 6.8. Waveguide formed by two infinitely extending plane-parallel metal sheets, separated by a distance b .

6.4 Discussion

As discussed in the introduction, the study of the transmission of electromagnetic radiation through small apertures has a long and venerable history. The standard approach to describe this, involves the study of the propagation properties of EM radiation through a waveguide with the same transverse dimensions as the slit, made from the same material as the metallic screen that carries the slit. Additionally, one has to weigh in the impedance mismatch between this waveguide and free space. Our slit forms a rectangular waveguide with a large aspect ratio (height/width). For that reason we can effectively describe each slit as a planar waveguide (see Fig. 6.8). Here we will apply such a waveguide model to see how much we can learn.

Inside the waveguide the solutions to Maxwell's equations separate into two sets of modes. For the so-called TE-modes the electric field is purely

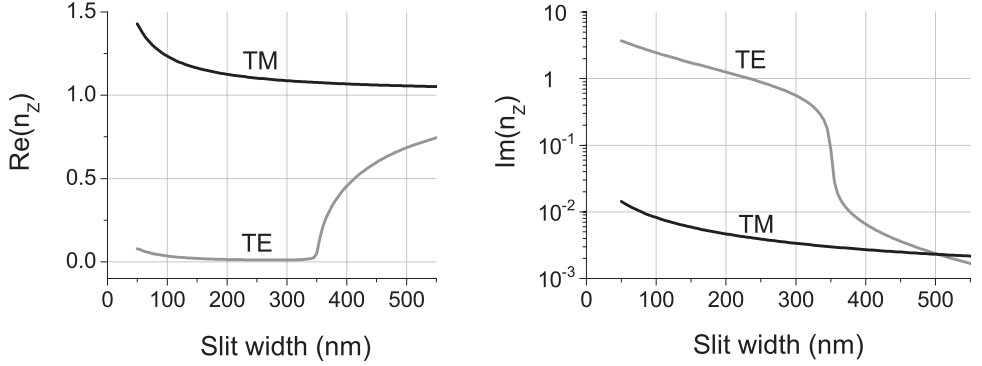


Figure 6.9. Real and imaginary parts of the mode index n_z for TM- and TE-polarized modes at $\lambda = 800$ nm in a waveguide of gold. The width of the waveguide (slit) is varied.

transverse, i.e., does not have a component in the propagation (z)-direction ($E_z = 0$); for these modes one solves the wave equation for E_y . The TM-modes have a purely transverse magnetic field and $H_z = 0$ everywhere in the waveguide; in this case one solves the wave equation for H_y .

For a monochromatic wave the dependence on space and time for E_y (TE-mode) or H_y (TM-mode) is written as:

$$\exp[i(\omega t - k_x x - k_z z)], \quad (6.6)$$

with

$$k_z = \sqrt{\frac{\omega^2}{c^2} - k_x^2}, \quad (6.7)$$

yielding

$$n_z = \sqrt{1 - \frac{k_x^2}{k_0^2}}, \quad (6.8)$$

for the mode index ($k_0 = \omega/c$). The allowed values for k_x follow from a set of matching conditions at the metallic boundaries and the requirement that, in the metal, k_x is purely imaginary [123]. These matching conditions give rise to a self-consistency equation for k_x , one for the case of a TE-wave, and one for the case of a TM-wave. The solutions of these equations for k_x are generally complex. Using Eq. (6.8) one can then determine the complex refractive indices for the TE- and TM-modes, respectively.

Figure 6.9 shows the results of such a calculation for the TE- and TM-polarized modes as a function of the slit width, at $\lambda = 800$ nm, for a waveguide

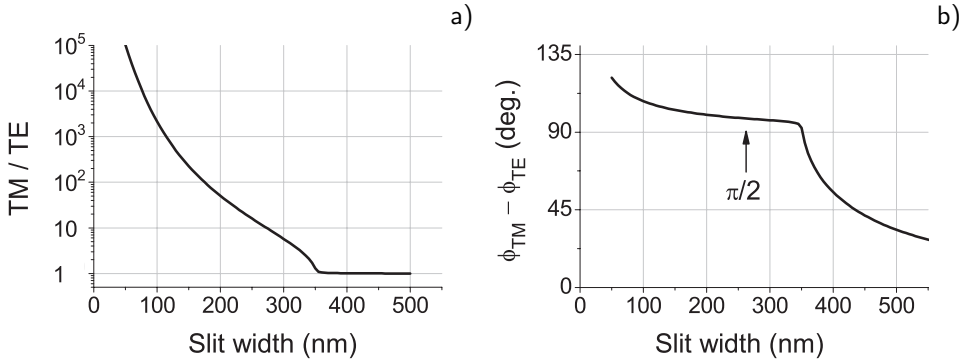


Figure 6.10. a) TM/TE transmission ratio of a 200 nm long piece of waveguide made from gold at a wavelength of 800 nm; b) Relative phase delay between the TE- and TM-modes of such a waveguide, as a function of waveguide width.

of gold. For the TM-mode both the real and imaginary parts of n_z depend weakly on the slit width b : the real part increases with decreasing slit width [41] while the imaginary part is close to zero, except at the smallest values of b , showing that the TM mode is only weakly damped. The variation of n_z is much more pronounced for the TE-mode: as b is reduced the real part of n_z drops off rapidly to become vanishingly small at $b \simeq 350$ nm (the cut-off width). At the same value of b the imaginary part of n_z is seen to jump by roughly a factor 50.

With the results of Fig. 6.9 we can explain most of our experimental results. First, by looking at the real part of the mode index, we see that the birefringence increases to a value of order 1, as the slit width is reduced from 500 to 350 nm. At smaller values of the slit width, the birefringence is “locked” to a value ≈ 1 . From the results for the imaginary part of the mode index, we see that the dichroism explodes at $b = 350$ nm, becoming so large that the transmitted light is purely TM-polarized when the slit width is below the critical value. Actually, already at $b = 400$ nm the dichroic effect is sufficiently large that the transmitted light is predominantly TM-polarized.

From the results of Fig. 6.9 we can calculate the relative modal transmission $\exp[-4\pi \text{Im}(n_z^{\text{TM}} - n_z^{\text{TE}}) t/\lambda]$ and the relative phase delay $\Delta\phi = 2\pi t \text{Re}(n_z^{\text{TM}} - n_z^{\text{TE}})$ for a section of waveguide of length $t = 200$ nm (see Fig. 6.10). It is seen that, even for such a short waveguide, the cut-off is well defined: the TM/TE transmission ratio rises rapidly for $b < 350$ nm. Moreover, we see that the TE-TM phase delay is predicted to be $\Delta\phi = \phi_{\text{TM}} - \phi_{\text{TE}} \approx \pi/2$ in the range $200 < b < 350$ nm, in quite good agreement with the

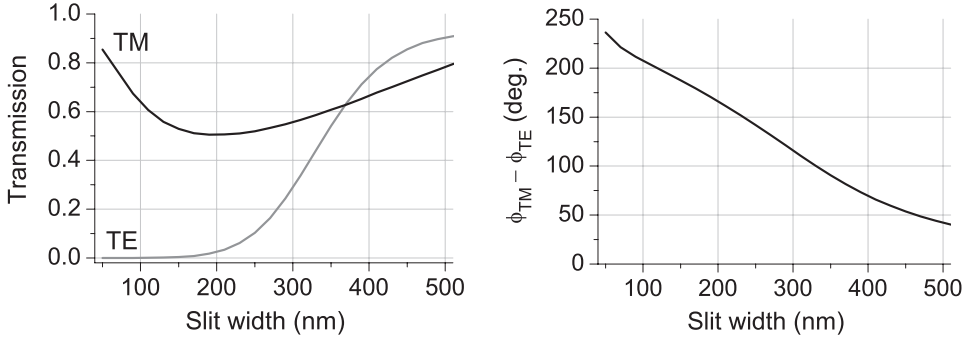


Figure 6.11. Results of a numerical calculation, based on a rigorous diffraction model, for the width-normalized transmission and relative phase delay, for a slit in a 200 nm thick gold film, studied with incident light at 800 nm.

experimental result (see Figs. 6.1 and 6.7).

Although the waveguide approach yields a reasonably prediction for the TM-TE phase slip at slit width of order 250 nm, it doesn't do such a good job in predicting the width dependence of the phase slip nor of the TM/TE transmission ratio as found in our experiments. This is not surprising since our model only accounts for the waveguide properties of the slit and does not take into account the coupling of the incident radiation with the waveguide mode, the outcoupling properties of the waveguide and the possibility of exciting surface plasmons or other surface modes.

In order to obtain a more complete picture we have turned to a rigorous diffraction model [90] where we take into account all known details of our setup. Specifically, we calculate the transmission and phase delay of a plane wave incident on the interface between a dielectric (glass) and a composite metal film consisting of 10 nm titanium metal with 200 nm gold on top. The metal sandwich is perforated by a single, infinitely long, narrow slit and the output field radiates into vacuum. We do so for both TE- and TM-polarized incident fields. The results are shown in Fig. 6.11.

Overall, the results of this calculation are in very good agreement with the experimental data of Fig. 6.4. In particular, the calculations reproduce the dip at $b \simeq 200$ nm in the transmission of the TM wave. We believe that this dip is associated with the excitation of surface plasmons. The probability of exciting these surface modes is predicted to peak when $b/\lambda \approx 1/4$ [34]. Also the gradual variation of the TE-mode transmission is well reproduced by the calculations, though the onset of transmission is shifted to larger slit

width in the calculation as compared to the experiment. The fact that for small values of the slit width the experimental TE transmission is considerably larger than predicted, can be attributed to unavoidable variations in the slit width. Small sections that have a width that is larger than the nominal value, will substantially increase the transmitted power. The calculations also do a good job in predicting the TM-TE phase difference that we have observed in the experiment yielding a $\pi/2$ phase difference between TM and TE modes at $b \simeq 350$ nm. Note, however, that the $(\phi_{\text{TM}} - \phi_{\text{TE}})$ curve in Fig. 6.11 is a bit steeper than that of Fig. 6.7b.

6.5 Conclusions

We have studied the transmission properties of a sub-wavelength slit milled in a 200 nm thick gold-metal film as a function of the slit width (50–500 nm), and of the polarization of the incident radiation (at $\lambda = 800$ nm). As the slit width is decreased the normalized transmission of the TE-mode diminishes quite gradually until it becomes vanishingly small at a value of the normalized slit width of order $1/8$, reminiscent of the phenomenon of waveguide cut-off. In contrast, the width-normalized transmission of the TM-mode varies only by a factor of 2 when the slit width varies between 50 nm and 500 nm. In this interval it shows a characteristic dip at a slit width of order $\lambda/4$, associated with the efficient excitation of surface plasmons. Moreover, we have measured the phase slip between the TM- and TE-polarized modes through such a sub-wavelength slit. We have compared our experimental results with a simple waveguide model and with the results of a rigorous diffraction calculation. The latter shows good predictive power and is able to reproduce most of the features of our experimental results.

CHAPTER 7

Short-wavelength surface plasmons

We report the generation and detection of surface plasmons propagating along a smooth buried silver/glass interface for incident wavelengths ranging from the blue well into the telecom band. Limited by ohmic loss, we reach photon energies of 2.6 eV, where the surface-plasmon wavelength equals 260 nm. These short-wavelength surface plasmons travel at one third of the speed of light in vacuo.

7.1 Introduction

Currently, there is considerable research activity in the field of plasmonics, one of the reasons being that surface plasmons provide a tool to structure light on a scale that is much finer than what can be achieved in free space or in a dielectric. A second goal of the research effort is to generate a form of slow light, allowing much enhanced interactions with resonant probes.

In the approach that is usually taken to achieve these goals the metallo-dielectric interface is *structured* either in the propagation direction, for instance by assembling an array of nano-sized metallic particles, or in the lateral direction, or both. On such a structured interface the surface plasmon is often quite rapidly damped as a consequence of radiative losses.

Alternatively, one can exploit the dispersion relation of a surface plasmon on an *unstructured* metallo-dielectric interface to generate short-wavelength (high- k), slow plasmons. Due to ohmic damping such high- k surface plasmons are either quite lossy or nonexistent, as is the case for gold. Here we explore the possibility of using a buried glass-silver interface for generating short-wavelength plasmons with a damping length of a few μm , more than sufficient for a variety of applications.

7.2 Dispersion and Damping

A surface plasmon is a solution to the wave equation that is bound to the interface between a dielectric, characterized by a real and positive relative permittivity ϵ_d , and a metal. The permittivity of the latter is always complex and is written as $\epsilon_m = \epsilon'_m + i\epsilon''_m$. At optical frequencies metallic behavior is associated with the requirement that $\epsilon'_m < 0$. Note that quite a few materials, such as tungsten and molybdenum, that are usually considered to be metallic do not fulfill this requirement over a considerable part of the optical spectrum.

For a surface plasmon to exist on a particular metallo-dielectric interface one must have $\epsilon'_m < -\epsilon_d < 0$. On a smooth interface its propagation constant is given by [8]:

$$k_{\text{sp}} = \frac{\omega}{c} \sqrt{\frac{\epsilon_m \epsilon_d}{\epsilon_m + \epsilon_d}}. \quad (7.1)$$

Since ϵ_m is a complex frequency-dependent quantity, so is k_{sp} . Hence we write:

$$k_{\text{sp}} = k' + ik'', \quad (7.2)$$

the imaginary part of k_{sp} quantifying the surface-plasmon damping length $L_{\text{sp}} = (k'')^{-1}$.

In the wavelength range where $\epsilon_m'' \ll -\epsilon_m'$ we can approximate the real and imaginary parts of k_{sp} as:

$$k' \simeq \frac{\omega}{c} \sqrt{\frac{\epsilon_m' \epsilon_d}{\epsilon_m' + \epsilon_d}}, \quad (7.3)$$

$$k'' \simeq \frac{\omega}{c} \frac{\epsilon_m''}{2(\epsilon_m')^2} \left(\frac{\epsilon_d \epsilon_m'}{\epsilon_d + \epsilon_m'} \right)^{3/2}. \quad (7.4)$$

In the appropriate wavelength interval the propagation constant k' of the surface plasmon can thus be well approximated by using Eq. (7.1) while neglecting the imaginary part of the permittivity [8]. Equation (7.4) shows that the real and imaginary parts of the wave vector of a surface plasmon are approximately related by:

$$\frac{k''}{k'} = \frac{\lambda_{\text{sp}}}{L_{\text{sp}}} \approx \frac{\epsilon_m'' \epsilon_d}{2(\epsilon_m')^2} \left(\frac{k'}{\sqrt{\epsilon_d} k_0} \right)^2, \quad (7.5)$$

with $k_0 = \omega/c$. The factor in brackets, which is a measure for how much the surface-plasmon dispersion curve $\omega(k')$ deviates from the light line $\omega = ck_0/\sqrt{\epsilon_d}$, is of order unity. Consequently, the ratio of the imaginary and real parts of the surface-plasmon wave vector is approximately given by the quantity $\epsilon_d \epsilon_m''/2(\epsilon_m')^2$, which, for good metals, is much smaller than unity. The damping length of the surface plasmon $L_{\text{sp}} = (k'')^{-1}$, in units of the surface-plasmon wavelength $\lambda_{\text{sp}} = (k')^{-1}$, thus scales as ϵ_d^{-1} . From this perspective, the best dielectric is vacuum.

If, however, the aim is to reach small values of λ_{sp} it is advantageous to use a material that has $\epsilon_d > 1$. For instance, in the experiment described below we attain $\lambda_{\text{sp}} = 260$ nm using a silver-glass interface and 2.6 eV photons. The amplitude damping length of a 2.6 eV surface plasmon propagating along that interface equals $L_{\text{sp}} = 2$ μm . To achieve a similar value of λ_{sp} on a *silver-air interface* we require 3.5 eV photons, with $L_{\text{sp}} = 0.35$ μm . This counterintuitive result is caused by the strong dispersion of the dielectric permittivity of silver, particular at high photon energies.

7.3 Experiment

It is widely appreciated that films of gold and silver do not adhere well when deposited or sputtered on top of a glass surface. For that reason, it is quite common to first apply a bonding material, for instance a thin (nanometer-thick) layer of chromium or titanium (see Chapters 2–6). As compared to

gold and silver, both these metals are quite dissipative, and the bonding layer should be at most a few nm thick in order not to extinguish the surface plasmons on the glass-silver interface. In the present experiment we don't use such a dissipative adhesion layer.

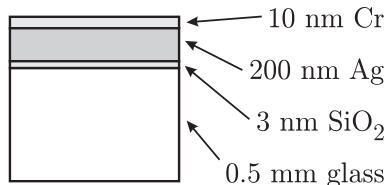


Figure 7.1. Structure of our sample.

In our samples, prepared by Laseroptik GmbH in Garbsen, Germany, we use a substrate made from borosilicate glass (Schott D263T), that is first coated with a 2–3 nm thick layer of *fused quartz* and, immediately after, with silver metal. Apparently, a freshly applied SiO₂ layer is sufficiently sticky to bind the Ag layer [124]. The silver film is 200 nm thick and is overcoated with a 10 nm thick layer of chromium. This top layer serves two purposes: to protect the silver film from becoming tarnished in ambient air, and to eliminate surface plasmons on the second interface [23]. A schematic of our film is shown in Fig. 7.1. The SiO₂ layer that sits between the glass and the silver is so thin that its presence is henceforth neglected. We have structured the silver film by means of ion-beam milling with a series of slit pairs, the two slits of a pair being separated by 8 or 25 μm , each slit being 100 nm wide and 50 μm long.

To measure the dispersion curve of the surface plasmon along the buried interface we use a so-called white-light laser (Fianium SC-450-2). This laser, when operated at full power (≈ 2 W), emits a continuous spectrum spanning the wavelength region from 450 to 1700 nm. The output spectrum of the laser is reasonably flat (see Fig. 7.2) except for the region near $\lambda = 1064$ nm where the narrow-band seed laser emits. The polarization of the laser output shows no preferred axis.

By using a wedge beamsplitter, about 5% of the output of the laser is directed at our sample. It passes a polarizer mounted in a rotation mount so that the polarization of the light can be chosen. Subsequently, it impinges on the sample at normal incidence and the transmitted light is imaged on the entrance facet of a fiber spectrometer (Ocean Optics SD2000 for the visible part of the spectrum, and Ocean Optics NIR-512 for the near-infrared part). The polarization of the incident light is chosen to be TM (relative to the slits) so that surface plasmons can be excited on the buried interface.

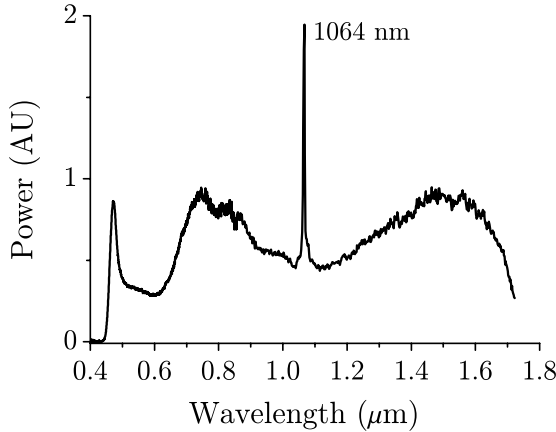


Figure 7.2. Spectrum of the Fianium SC-450-2 laser at full power. The experimental spectrum has been acquired by using a visible and IR fiber spectrometer and stitching the two data sets together.

In the present experiment the wavelength of the incident light spans nearly two octaves, from 450 to 1700 nm. Over this full range of incident wavelengths both the slit width and the film thickness are constant at a nominal value of 100 and 200 nm, respectively. The slit width thus varies between $\lambda/4$ and $\lambda/16$, the film thickness between $\approx \lambda/2$ and $\lambda/8$.

7.4 Results and Discussion

Figure 7.3 shows raw data for wavelengths between 400 and 1500 nm for an 8 μm and a 25 μm double slit. All spectra show a fast spectral modulation on top of a slowly varying spectrum. The latter represents the output of the Fianium laser as registered by our spectrometer, while the spectral modulation is due to plasmonic cross-talk as discussed in Chapter 2. While the modulation features are very well resolved in the near-infrared spectral region ($\lambda > 650$ nm) the visibility of the fringes rapidly decreases at shorter wavelengths. In the spectrum of the 8 μm double slit fringes can be seen down to wavelengths of 477 nm ($h\nu = 2.6$ eV); in contrast, for the 25 μm double slit the spectrum becomes featureless already at $\lambda = 530$ μm ($h\nu = 2.34$ eV). At long wavelengths ($\lambda > 1300$ nm), the spectral modulation vanishes also; at such small values of the wavelength-normalized slit width ($w/\lambda < 0.1$) the surface-plasmon excitation probability is predicted to become very small [35].

The features that we observe are due to interference: the light field that

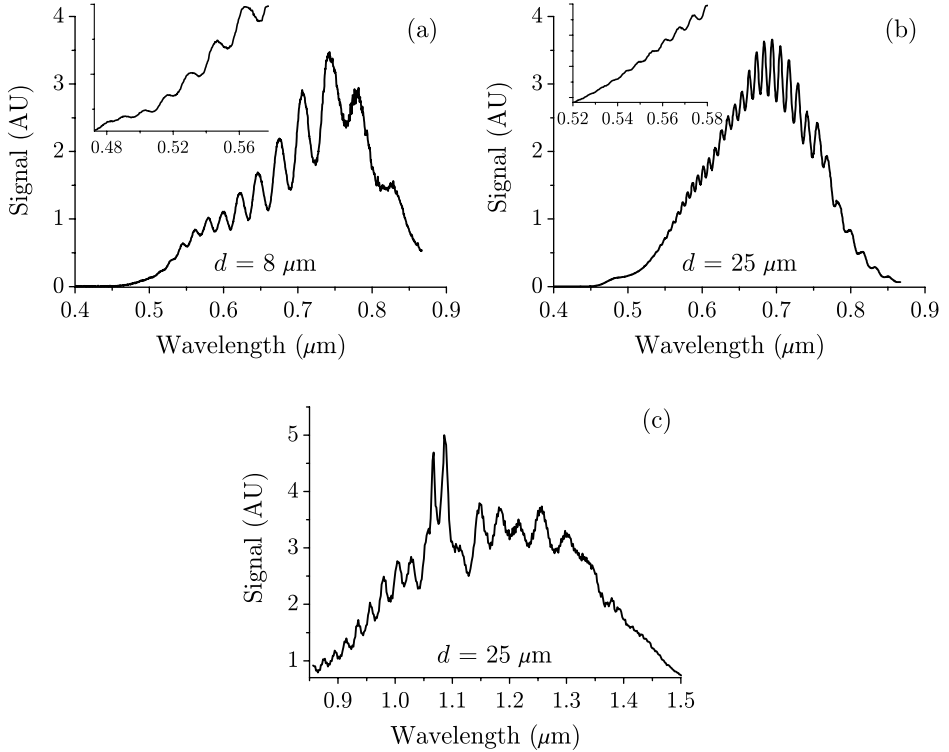


Figure 7.3. Uncorrected transmission spectra for a) an 8 μm double slit in the visible part of the spectrum, b) a 25 μm double slit, also in the visible part of the spectrum, and c) a 25 μm double slit in the IR part of the spectrum. The insets in a) and b) show a magnified view of the short-wavelength part of the spectra. The infrared spectrum carries a prominent doublet near $\lambda = 1.06 \mu\text{m}$, representing the strongly enhanced output of the laser near that wavelength, modulated by plasmonic cross-talk.

emanates from slit 1 is a coherent sum of (a small fraction of) the light field incident on that slit, and a small fraction of the field that falls on slit 2, is scattered into a surface plasmon that travels from slit 2 to slit 1 and is back-converted into a light field at slit 1. The amplitude of the field emanating from slit 1 can be written as:

$$E = E_0(\lambda)[1 + \alpha(\lambda) \cos(k'd + \pi)], \quad (7.6)$$

where E_0 represents the amplitude of the field transmitted by slit 1, d is the distance between the slits and α a positive real coefficient describing the

scattering of light incident on slit 2, coupled into a surface plasmon, and re-radiated by slit 1. Both E_0 and α are explicitly dependent on the wavelength λ of the incident light. The phase factor π has been discussed in Chapter 5.

From the experimental spectra we can extract the wavelengths of the maxima and minima in the signal, the maxima corresponding to the case that $k'(\lambda)d = (2m + 1)\pi$, while $k'(\lambda)d = 2m\pi$ at the minima. By a judicious choice of the value of m at a particular maximum or minimum we can associate values of m with all maxima and minima. Since we know d with sufficient accuracy we can extract values for the surface-plasmon propagation constant k' for all incident wavelengths. This allows us to construct a dispersion diagram of the surface plasmon (see Fig. 7.4).

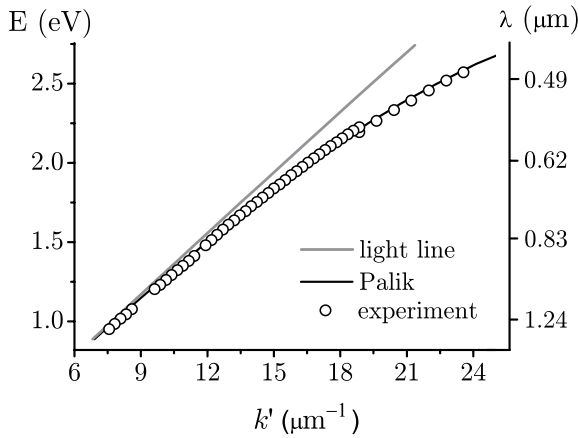


Figure 7.4. Dispersion curve for the surface plasmon along a smooth silver-glass interface. The circles give the experimental results, the black solid line the values of the real part of the surface-plasmon propagation constant calculated using Eq.(7.1) and the tabulated values for the dielectric permittivity of silver and the glass. The grey solid line shows the dispersion of a free electromagnetic wave propagating through the bulk glass.

The data points for $k' < 12 (\mu\text{m})^{-1}$ have been recorded with the infrared spectrometer using the pair of slits separated by $25 \mu\text{m}$; those for $18.6 (\mu\text{m})^{-1} < k' < 12 (\mu\text{m})^{-1}$ with the visible spectrometer and the $25 \mu\text{m}$ double slit, while those for $k' > 18.6 (\mu\text{m})^{-1}$ were gathered with the $8 \mu\text{m}$ double slit. The solid line shows the dispersion curve according to Eq. (7.1), using the tabulated values for the dispersion of the real and imaginary parts of the refractive index of silver [22], and that of D263T borosilicate glass [125]. Finally, the grey solid line shows the dispersion of a free electromagnetic wave

through our glass with $n = 1.5166$ at $\lambda = 800$ nm. The experimental data are in excellent agreement with the calculated dispersion curve; to achieve this level of agreement we have to take the (small) dispersion of the refractive index of the D263T glass into account.

The last data point on our graph corresponds to a photon energy of 2.6 eV, i.e., a free-space wavelength of 477 nm. Using the tabulated values of the complex refractive index of silver we calculate the surface-plasmon damping coefficient for the silver-glass interface to be $k'' = 0.502$ (μm)⁻¹. Thus, the surface-plasmon (amplitude) damping length equals ≈ 2 μm , which explains why the modulation signal due to surface plasmons becomes very small for a slit separation of 8 μm , at these short wavelengths. The use of closer-lying slits (4 or 6 μm slit separation) did not allow us to measure plasmonic modulation at higher photon energies. Recently, Temnov *et al.* reported similar measurements on a bare (i.e., air-) silver interface; their experimental data terminated at $h\nu = 2.1$ eV, in the middle of the orange spectral region ($\lambda = 590$ nm) [73]. We conjecture that the difference is due to the superior quality and stability of our buried silver film. The use of a buried interface carries another advantage: at our highest-energy data point the surface-plasmon effective index $n_{\text{sp}} = c_0 k' / \omega = 1.83$, with c_0 the vacuum speed of light and ω the optical frequency. At this frequency we have $\lambda_{\text{sp}} = 260$ nm.

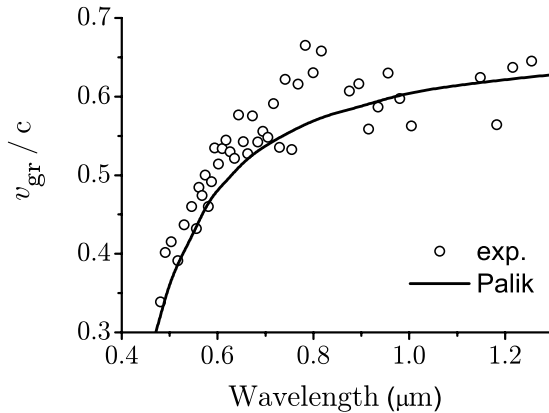


Figure 7.5. Dispersion of the group velocity of a surface plasmon along the buried quartz-silver interface. The data points are obtained by determining $\Delta\omega/\Delta k$ from adjacent experimental points in Fig. 7.4. The solid curve follows from the theoretical expression for the surface-plasmon dispersion (Eq. (7.1)).

From our data we can determine the dispersion of the surface-plasmon group

velocity on our interface (see Fig. 7.5). The scatter in the data represents the small deviations of the experimental data points away from the smooth dispersion curve of Fig. 7.4.

We observe the surface-plasmon group velocity to reach a value of $c_0/3$, with c_0 the vacuum speed of light, a reduction by a factor 2 as compared to surface plasmons in the infrared spectra region ($h\nu < 1.0$ eV). A similar reduction in surface-plasmon group velocity has recently been reported in a structured metallic waveguide [126].

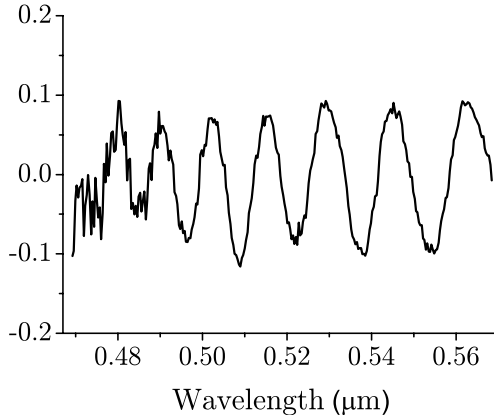


Figure 7.6. AC-component of the experimental data of Fig. 7.3 for the $8 \mu\text{m}$ double slit, corrected for the effect of surface-plasmon damping.

The spectra of Fig. 7.3 show that the spectral modulation varies considerably with the wavelength of the incident radiation, and that it is largest in the near-infrared spectral region. Various factors play a role here. First, we note that, according to Eq. (7.6), the modulation depth

$$M = 2 \frac{S(\lambda_{\max}) - S(\lambda_{\min})}{S(\lambda_{\max}) + S(\lambda_{\min})} \approx 4\alpha(\lambda) \quad (7.7)$$

provides a measure of the relative strength of the plasmonic and direct channels in the slit transmission. Therefore, the modulation depth is sensitive to factors that affect the direct channel, such as the ratio of slit width and incident wavelength, the ratio of slit depth and wavelength, *and* factors that affect the SP channel such as, again, the ratio of slit width and incident wavelength, and the surface plasmon damping along the interface. The latter effect can easily be calculated. In Fig. 7.6 we show the high-frequency component of the experimental data of the $8 \mu\text{m}$ double slit of Fig. 7.3, corrected for surface-plasmon damping using the dispersion data of Johnson and Christy [22]. The

corrected data show only a slight wavelength dependence, suggesting that the other factors play a minor role across the wavelength range covered in Fig. 7.6, or that these factors largely cancel each other.

7.5 Conclusions

We have performed a comprehensive study of the surface-plasmon dispersion on a glass-silver interface spanning 2 octaves in photon energy. Using a double-slit setup we have observed, up to photon energies of 2.6 eV, spectral features that are caused by an interference effect that involves a surface plasmon and light directly transmitted by the slits. At these high photon energies the surface plasmon on the silver-glass interface has a wavelength of only 260 nm and propagates with a group velocity equal to 1/3 of the speed of light in vacuum. Our experiments show that buried silver is an excellent and stable material for surface-plasmon studies and that the silver-glass interface gives access to surface plasmons with very short wavelengths.

Bibliography

- [1] D. L. Simms, *Archimedes and the burning mirrors*, Phys. Educ. **10**, 517 (1975).
- [2] D. L. Simms, *Archimedes and the burning mirrors of syracuse*, Technology and Culture **18**, 1 (1977).
- [3] http://www.thebritishmuseum.ac.uk/explore/highlights/highlight_objects/pe_mla/t/the_lycurgus_cup.aspx.
- [4] N. W. Ashcroft and N. D. Mermin, *Solid state physics*, Holt, Rinehart and Winston, USA, 1976.
- [5] C. Kittel, *Introduction to solid state physics*, Wiley, USA, 7 edition, 1995.
- [6] R. H. Ritchie, *Plasma losses by fast electrons in thin films*, Phys. Rev. **106**, 874 (1957).
- [7] C. J. Powell and J. B. Swan, *Origin of the characteristic electron energy losses in aluminum*, Phys. Rev. **115**, 869 (1959).
- [8] H. Raether, *Surface plasmons on smooth and rough surfaces and on gratings*, Springer, Berlin, 1988.
- [9] W. L. Barnes, A. Dereux, and T. W. Ebbesen, *Surface plasmon sub-wavelength optics*, Nature **424**, 824 (2003).
- [10] R. D. Averitt, S. L. Westcott, and N. Halas, *Linear optical properties of gold nanoshells*, JOSA B **16**, 1824 (1999).
- [11] M. Moskovits, *Surface-enhanced spectroscopy*, Rev. Mod. Phys. **57**, 783 (1985).
- [12] A. Zangwill, *Physics at surfaces*, Cambridge Univ. Press, Cambridge, UK, 1988.
- [13] T. Neumann, M. L. Johansson, D. Kambhampati, and W. Knoll, *Surface-plasmon fluorescence spectroscopy*, Adv. Funct. Mater. **12**, 575 (2002).

- [14] G. A. Farias and A. A. Maradudin, *Surface plasmon on a randomly rough surface*, Phys. Rev. B **28**, 5675 (1983).
- [15] K. R. Welford and J. R. Sambles, *Coupled surface plasmons in a symmetric system*, J. Mod. Opt. **35**, 1467 (1988).
- [16] J. J. Burke, G. I. Stegeman, and T. Tamir, *Surface-polariton-like waves guided by thin, lossy metal films*, Phys. Rev. B **33**, 5186 (1986).
- [17] I. Breukelaar, R. Charbonneau, and P. Berinia, *Long-range surface plasmon-polariton mode cutoff and radiation*, Appl. Phys. Lett. **88**, 051119 (2006).
- [18] E. D. Palik, editor, *Handbook of optical constants of solids II*, Academic Press, Boston, USA, 1991.
- [19] V. M. Agranovich, Y. R. Shen, R. H. Baughman, and A. A. Zakhidov, *Optical bulk and surface waves with negative refraction*, Journal of Luminescence **110**, 167 (2004).
- [20] P. Tournois and V. Laude, *Negative group velocities in metal-film optical waveguides*, Opt. Comm. **137**, 41 (1997).
- [21] Y. Liu, D. Pile, Z. Liu, D. Wu, C. Sun, and X. Zhang, *Negative group velocity of surface plasmons on thin metallic films*, SPIE **6323**, 63231M (2006).
- [22] P. B. Johnson and R. W. Christy, *Optical constants of the noble metals*, Phys. Rev. B **6**, 4370 (1972).
- [23] M. D. McMahon, R. Lopez, H. M. Meyer, L. C. Feldman, and R. F. Haglund, *Rapid tarnishing of silver nanoparticles in ambient laboratory air*, Appl. Phys. B **80**, 915 (2005).
- [24] A. V. Zayats, I. I. Smolyaninov, and A. A. Maradudin, *Nano-optics of surface-plasmon polaritons*, Phys. Rep. **408**, 131 (2005).
- [25] E. Kretschmann and H. Raether, Z. Naturforsch. A **23**, 2135 (1968).
- [26] A. Otto, Z. Physik **216**, 398 (1968).
- [27] T. López-Ríos and G. Vuye, *In situ investigation of metallic surfaces by surface plasmon ATR spectroscopy, electrical resistance measurements and Auger spectroscopy*, J. Phys. E: Sci. Instrum. **15**, 456 (1982).
- [28] N. Zhang, R. Schweiss, Y. Zong, and W. Knoll, *Electrochemical surface plasmon spectroscopy — recent developments and applications*, Electrochimica Acta **52**, 2869 (2007).
- [29] R. C. Reddick, R. J. Warmack, and T. L. Ferrell, *New form of scanning optical microscopy*, Phys. Rev. B **39**, 767 (1989).
- [30] P. Dawson, F. de Fornel, and J.-P. Goudonnet, *Imaging of surface plasmon propagation and edge interaction using a photon scanning tunneling microscope*, Phys. Rev. Lett. **72**, 2927 (1994).

- [31] S. I. Bozhevolnyi, I. I. Smolyaninov, and A. V. Zayats, *Near-field microscopy of surface-plasmon polaritons: localization and internal interface imaging*, Phys. Rev. B **51**, 17916 (1995).
- [32] H. Gersen, J. P. Korterik, N. F. van Hulst, and L. Kuipers, *Tracking ultrashort pulses through dispersive media: experiment and theory*, Phys. Rev. E **68**, 026604 (2003).
- [33] H. Gersen, T. J. Karle, R. J. P. Engelen, W. Bogaerts, J. P. Korterik, N. F. van Hulst, T. F. Krauss, and L. Kuipers, *Real-space observation of ultraslow light in photonic crystal waveguides*, Phys. Rev. Lett. **94**, 073903 (2005).
- [34] P. Lalanne, J. P. Hugonin, and J. C. Rodier, *Theory of surface plasmon generation at nanoslit apertures*, Phys. Rev. Lett. **95**, 263902 (2005).
- [35] P. Lalanne, J. P. Hugonin, and J. C. Rodier, *Approximate model for surface-plasmon generation at slit apertures*, J. Opt. Soc. Am. A **23**, 1608 (2006).
- [36] T. W. Ebbesen, H. J. Lezec, H. F. Ghaemi, T. Thio, and P. A. Wolff, *Extraordinary optical transmission through sub-wavelength hole arrays*, Nature **391**, 667 (1998).
- [37] H. A. Bethe, *Theory of diffraction by small holes*, Phys. Rev. **66**, 163 (1944).
- [38] U. Schröter and D. Heitmann, *Surface-plasmon-enhanced transmission through metallic gratings*, Phys. Rev. B **58**, 15419 (1998).
- [39] M. B. Sobnack, W. C. Tan, N. P. Wanstall, T. W. Preist, and J. R. Sambles, *Stationary surface plasmons on a zero-order metal grating*, Phys. Rev. Lett. **80**, 5667 (1998).
- [40] J. A. Porto, F. J. García-Vidal, and J. B. Pendry, *Transmission resonances on metallic gratings with very narrow slits*, Phys. Rev. Lett. **83**, 2845 (1999).
- [41] S. Astilean, P. Lalanne, and M. Palamaru, *Light transmission through metallic channels much smaller than the wavelength*, Opt. Comm. **175**, 265 (2000).
- [42] H. E. Went, A. P. Hibbins, J. R. Sambles, C. R. Lawrence, and A. P. Crick, *Selective transmission through very deep zero-order metallic gratings at microwave frequencies*, Appl. Phys. Lett. **77**, 2789 (2000).
- [43] Y. Takakura, *Optical resonance in a narrow slit in a thick metallic screen*, Phys. Rev. Lett. **86**, 5601 (2001).
- [44] M. M. J. Treacy, *Dynamical diffraction explanation of the anomalous transmission of light through metallic gratings*, Phys. Rev. B **66**, 195105 (2002).

- [45] Q. Cao and P. Lalanne, *Negative role of surface plasmons in the transmission of metallic gratings with very narrow slits*, Phys. Rev. Lett. **88**, 057403 (2002).
- [46] P. Lalanne, C. Sauvan, J. P. Hugonin, J. C. Rodier, and P. Chavel, *Perturbative approach for surface plasmon effects on flat interfaces periodically corrugated by subwavelength apertures*, Phys. Rev. B **68**, 125404 (2003).
- [47] A. Barbara, P. Quemerais, E. Bustarret, T. López-Ríos, and T. Fournier, *Electromagnetic resonances of sub-wavelength rectangular metallic gratings*, Eur. Phys. J. D **23**, 143 (2003).
- [48] J. R. Suckling, A. P. Hibbins, M. J. Lockyear, T. W. Preist, J. R. Sambles, and C. R. Lawrence, *Finite conductance governs the resonance transmission of thin metal slits at microwave frequencies*, Phys. Rev. Lett. **92**, 147401 (2004).
- [49] F. J. García-Vidal, H. J. Lezec, T. W. Ebbesen, and L. Martín-Moreno, *Multiple paths to enhance optical transmission through a single sub-wavelength slit*, Phys. Rev. Lett. **90**, 213901 (2003).
- [50] A. P. Hibbins, J. R. Sambles, C. R. Lawrence, and J. R. Brown, *Squeezing millimeter waves into microns*, Phys. Rev. Lett. **92**, 143904 (2004).
- [51] H. Lezec and T. Thio, *Diffraction evanescent wave model for enhanced and suppressed optical transmission through subwavelength hole arrays*, Opt. Exp. **12**, 3629 (2004).
- [52] L. A. Giannuzzi and F. A. Stevie, editors, *Introduction to focused ion beams: instrumentation, theory, techniques and practice*, Springer, USA, 2005.
- [53] E. D. Palik, editor, *Handbook of optical constants of solids*, Academic Press, Boston, USA, 1985.
- [54] P. B. Johnson and R. W. Christy, *Optical constants of transition metals: Ti, V, Cr, Mn, Fe, Co, Ni, and Pd*, Phys. Rev. B **9**, 5056 (1974).
- [55] T. D. Visser, H. Blok, and D. Lenstra, *Theory of polarization-dependent amplification in a slab waveguide with anisotropic gain and losses*, IEEE J. Quantum Electron. **35**, 240 (1999).
- [56] H. F. Schouten, T. D. Visser, D. Lenstra, and H. Blok, *Light transmission through a subwavelength slit: waveguiding and optical vortices*, Phys. Rev. E **67**, 036608 (2003).
- [57] K. E. Atkinson, *A survey of numerical methods of Fredholm equations of the second kind*, SIAM, Philadelphia, 1976, Chap. 2.
- [58] L. Mandel and E. Wolf, *Optical coherence and quantum optics*, Cambridge University Press, Cambridge, UK, 1995.

- [59] M. Born and E. Wolf, *Principles of optics*, Cambridge University Press, Cambridge, UK, seventh edition, 1999.
- [60] E. Wolf, *Young's interference fringes with narrow-band light*, Opt. Lett. **8**, 250 (1983).
- [61] H. F. Schouten, N. V. Kuzmin, G. Dubois, T. D. Visser, G. Gbur, P. F. A. Alkemade, H. Blok, G. W. 't Hooft, D. Lenstra, and E. R. Eliel, *Plasmon-assisted two-slit transmission: Young's experiment revisited*, Phys. Rev. Lett. **94**, 053901 (2005).
- [62] R. Carminati and J. Greffet, *Near-field effects in spatial coherence of thermal sources*, Phys. Rev. Lett. **82**, 1660 (1999).
- [63] P. Lalanne and J. P. Hugonin, *Interaction between optical nano-objects at metallo-dielectric interfaces*, Nature Phys. **2**, 551 (2006).
- [64] W. L. Barnes, A. Dereux, and T. W. Ebbesen, *Surface plasmon sub-wavelength optics*, Nature **424**, 824 (2003).
- [65] I. I. Smolyaninov, J. Elliott, G. Wurtz, A. V. Zayats, and C. C. Davis, *Digital resolution enhancement in surface plasmon microscopy*, Appl. Phys. B **84**, 253 (2006).
- [66] B. Liedberg, C. Nylander, and I. Lundström, *Biosensing with surface plasmon resonance — how it all started*, Biosensors and Bioelectronics **10**, i (1995).
- [67] F. Yu, S. Tian, D. Yao, and W. Knoll, *Surface plasmon enhanced diffraction for label-free biosensing*, Analytical Chemistry **76**, 3530 (2004).
- [68] V. Shalaev and S. Kawata, *Nanophotonics with surface plasmons*, Elsevier, Amsterdam, 2006.
- [69] M. L. Brongersma and P. G. Kik, *Surface plasmon nanophotonics*, Springer, The Netherlands, 2007.
- [70] L. Cao, N. C. Panoiu, and R. M. Osgood, *Surface second-harmonic generation from surface plasmon waves scattered by metallic nanostructures*, Phys. Rev. B **75**, 205401 (2007).
- [71] D. E. Chang, A. S. Sorensen, P. R. Hemmer, and M. D. Lukin, *Quantum optics with surface plasmons*, Phys. Rev. Lett. **97**, 053002 (2006).
- [72] C. Genet and T. W. Ebbesen, *Light in tiny holes*, Nature **445**, 39 (2007).
- [73] V. V. Temnov, U. Woggon, J. Dintinger, E. Devaux, and T. W. Ebbesen, *Surface plasmon interferometry: measuring group velocity of surface plasmons*, Opt. Lett. **32**, 1235 (2007).
- [74] C. H. Gan, G. Gbur, and T. D. Visser, *Surface plasmons modulate the spatial coherence of light in Young's interference experiment*, Phys. Rev. Lett. **98**, 043908 (2007).

- [75] N. V. Kuzmin, H. F. Schouten, G. Gbur, G. W. 't Hooft, E. R. Eliel, and T. D. Visser, *Enhancement of spatial coherence by surface plasmons*, Opt. Lett. **32**, 445 (2007).
- [76] H. Ditlbacher, A. Hohenau, D. Wagner, U. Kreibig, M. Rogers, F. Hofer, F. R. Aussenegg, and J. R. Krenn, *Silver nanowires as surface plasmon resonators*, Phys. Rev. Lett. **95**, 257403 (2005).
- [77] C. F. Bohren and F. R. Huffman, *Absorption and scattering of light by small particles*, Wiley, New York, 1983.
- [78] A. E. Siegman, *Lasers*, University Science Books, USA, 1986.
- [79] J. J. Scherer, J. B. Paul, A. O'Keefe, and R. J. Saykally, *Cavity ringdown laser absorption spectroscopy: history, development, and application to pulsed molecular beams*, Chem. Rev. **97**, 25 (1997).
- [80] M. Z. Alam, J. Meier, J. S. Aitchison, and M. Mojahedi, *Gain assisted surface plasmon polariton in quantum wells structures*, Opt. Exp. **15**, 176 (2007).
- [81] J. C. Diels and W. Rudolph, *Ultrashort laser pulse phenomena*, Academic Press, California, 1996.
- [82] M. Galli, F. Marabelli, and G. Guizzetti, *Direct measurement of refractive-index dispersion of transparent media by white-light interferometry*, Appl. Opt. **42**, 3910 (2003).
- [83] M. Bai, C. Guerrero, S. Ioanid, E. Paz, M. Sanz, and N. García, *Measuring the speed of a surface plasmon*, Phys. Rev. B **69**, 115416 (2004).
- [84] R. F. Wallis, A. A. Maradudin, and G. I. Stegeman, *Surface polariton reflection and radiation at end faces*, Appl. Phys. Lett. **42**, 764 (1983).
- [85] A. Bouhelier, T. Huser, H. Tamaru, H. J. Güntherodt, D. W. Pohl, F. I. Baida, and D. V. Labeke, *Plasmon optics of structured silver films*, Phys. Rev. B **63**, 155404 (2001).
- [86] J. Seidel, S. Grafström, L. Eng, and L. Bischoff, *Surface plasmon transmission across narrow grooves in thin silver films*, Appl. Phys. Lett. **82**, 1368 (2003).
- [87] T. Okamoto, K. Kakutani, T. Yoshizaki, M. Haraguchi, and M. Fukui, *Experimental evaluation of reflectance of surface plasmon polariton at metal step barrier*, Surface Science **544**, 67 (2003).
- [88] F. López-Tejiera, F. J. García-Vidal, and L. Martín-Moreno, *Scattering of surface plasmons by one-dimensional periodic nanoindented surfaces*, Phys. Rev. B **72**, 161405(R) (2005).
- [89] M. U. González, J. C. Weeber, A. L. Baudrion, A. Dereux, A. L. Stepanov, J. R. K. E. Devaux, and T. W. Ebbesen, *Design, near-field*

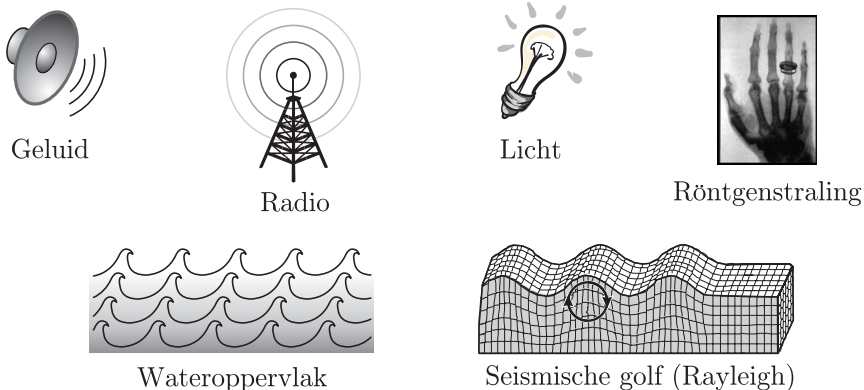
- characterization, and modeling of 45° surface-plasmon Bragg mirrors, *Phys. Rev. B* **73**, 155416 (2006).
- [90] O. T. A. Janssen, H. P. Urbach, and G. W. 't Hooft, *On the phase of plasmons excited by slits in a metal film*, *Opt. Exp.* **14**, 11823 (2006).
- [91] U. Fano, *Effects of configuration interaction on intensities and phase shifts*, *Phys. Rev.* **124**, 1866 (1961).
- [92] R. H. J. Kop and R. Sprik, *Phase-sensitive interferometry with ultrashort optical pulses*, *Rev. Sci. Instr.* **66**, 5459 (1995).
- [93] V. M. Agranovich, *Crystal optics of surface polaritons and the properties of surfaces*, *Sov. Phys.-Usp.* **18**, 99 (1975).
- [94] V. M. Agranovich and D. L. Mills, editors, *Surface polaritons: electromagnetic waves of surfaces and interfaces*, North-Holland, Amsterdam, 1982.
- [95] J. A. Sánchez-Gil, *Surface defect scattering of surface plasmon polaritons: mirrors and light emitters*, *Appl. Phys. Lett.* **73**, 3509 (1998).
- [96] A. V. Shchegrov, I. V. Novikov, and A. A. Maradudin, *Scattering of surface plasmon polaritons by a circularly symmetric surface defect*, *Phys. Rev. Lett.* **78**, 4269 (1997).
- [97] J. A. Sánchez-Gil and A. A. Maradudin, *Resonant scattering of surface-plasmon polariton pulses by nanoscale metal defects*, *Opt. Lett.* **28**, 2255 (2003).
- [98] J. A. Sánchez-Gil and A. A. Maradudin, *Surface-plasmon polariton scattering from a finite array of nanogrooves/ridges: efficient mirrors*, *Appl. Phys. Lett.* **86**, 251106 (2005).
- [99] G. Gay, O. Alloschery, J. Weiner, H. J. Lezec, C. O. Dwyer, M. Sukharev, and T. Seideman, *The response of nanostructured surfaces in the near field*, *Nature Phys.* **2**, 792 (2006).
- [100] G. Gay, O. Alloschery, B. V. de Lesegno, J. Weiner, and H. J. Lezec, *Surface wave generation and propagation on metallic subwavelength structures measured by far-field interferometry*, *Phys. Rev. Lett.* **96**, 123901 (2006).
- [101] L. Aigouy, P. Lalanne, J. P. Hugonin, G. Julie, V. Mathet, and M. Mortier, *Near-field analysis of surface waves launched at nanoslit apertures*, *Phys. Rev. Lett.* **98**, 153902 (2007).
- [102] F. Kalkum, G. Gay, O. Alloschery, J. Weiner, H. J. Lezec, Y. Xie, and M. Mansuripur, *Surface-wave interferometry on single subwavelength slit-groove structures fabricated on gold films*, *Opt. Exp.* **15**, 2613 (2007).

- [103] T. D. Visser, *Plasmonics – surface plasmons at work?*, Nature Phys. **2**, 509 (2006).
- [104] M. H. Fizeau, *Recherches sur plusieurs phénomènes relatifs à la polarisation de la lumière*, Ann. Chim. (Phys.) **63**, 385 (1861).
- [105] J. C. Slater, *Microwave transmission*, McGraw-Hill, New York, 1942.
- [106] G. Thiessen, *Polarisation des Lichtes beim Durchgang durch Metallspalte*, Die Himmelswelt **55**, 72 (1948).
- [107] R. V. Jones and J. C. S. Richards, *The polarization of light by narrow slits*, Proc. Roy. Soc. London A **225**, 122 (1954).
- [108] M. A. Ismail, *Transmission of light by slit designed for astronomical spectrograph*, Astrophysics and Space Science **122**, 1 (1986).
- [109] C. J. Bouwkamp, *Diffraction theory*, Rep. Progr. Phys. **18**, 35 (1954).
- [110] G. Bouwhuis, J. Braat, A. Huijser, J. Pasman, G. van Rosmalen, and K. S. Immink, *Principles of optical disk systems*, Adam Hilger Ltd, Bristol, UK, 1985.
- [111] H. J. Lezec, A. Degiron, E. Devaux, R. A. Linke, L. Martín-Moreno, F. J. García-Vidal, and T. W. Ebbesen, *Beaming light from a subwavelength aperture*, Science **297**, 820 (2002).
- [112] C. Genet, M. P. van Exter, and J. P. Woerdman, *Fano-type interpretation of red shifts and red tails in hole array transmission spectra*, Opt. Comm. **225**, 331 (2003).
- [113] R. C. McPhedran, *On the theory and solar application of inductive grids*, Appl. Phys. **14**, 1 (1977).
- [114] F. Yang and J. R. Sambles, *Resonant transmission of microwaves through a narrow metallic slit*, Phys. Rev. Lett. **89**, 063901 (2002).
- [115] H. F. Schouten, T. Visser, G. Gbur, D. Lenstra, and H. Blok, *The diffraction of light by narrow slits in plates of different materials*, J. Opt. A **6**, s277 (2004).
- [116] R. Wannemacher, *Plasmon-supported transmission of light through nanometric holes in metallic thin films*, Opt. Comm. **195**, 107 (2001).
- [117] F. G. de Abajo, *Light transmission through a single cylindrical hole in a metallic film*, Opt. Exp. **10**, 1475 (2002).
- [118] Y. Xie, A. Zakharian, J. Moloney, and M. Mansuripur, *Transmission of light through slit apertures in metallic films*, Opt. Exp. **12**, 6106 (2004).
- [119] J. Lindberg, K. Lindfors, T. Setälä, M. Kaivola, and A. Friberg, *Spectral analysis of resonant transmission of light through a single sub-wavelength slit*, Opt. Exp. **12**, 623 (2004).

- [120] F. J. García-Vidal, E. Moreno, J. A. Porto, and L. Martín-Moreno, *Transmission of light through a single rectangular hole*, Phys. Rev. Lett. **95**, 103901 (2005).
- [121] S. V. Kukhlevsky, M. Mechler, L. Csapo, K. Janssens, and O. Samek, *Resonant backward scattering of light by a subwavelength metallic slit with two open sides*, Phys. Rev. B **72**, 165421 (2005).
- [122] F. J. García-Vidal, L. Martín-Moreno, E. Moreno, L. K. S. Kumar, and R. Gordon, *Transmission of light through a single rectangular hole in a real metal*, Phys. Rev. B **74**, 153411 (2006).
- [123] B. E. A. Saleh and M. C. Teich, *Fundamentals of photonics*, John Wiley & Sons, Inc., USA, Hoboken, New Jersey, 2007.
- [124] W. Moorhoff, Laseroptik GmbH, Garbsen, Germany, private communication.
- [125] http://www.uqgoptics.com/materials_commercial_schott_D263T.asp.
- [126] M. Sandtke and L. Kuipers, *Slow guided surface plasmons at telecom frequencies*, Nature Photon. **1**, 573 (2007).

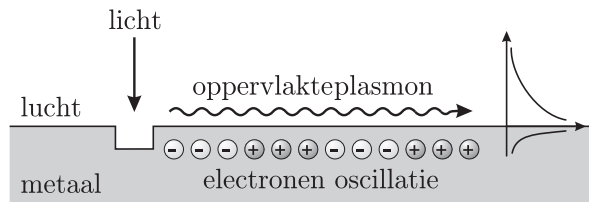
Samenvatting

Overall om ons heen zijn golven: geluid wordt overgebracht door geluidsgolven, aan zee zie we golven op het wateroppervlak, soms voelen wij seismische golven, we maken voortdurend gebruik van elektromagnetische golven zoals bij radio, licht, Röntgenstraling, enz. Grofweg kan je al deze golfverschijnselen in twee klassen indelen, nl. golven die zich voortplanten in de drager zelf en golven die juist alleen aan het oppervlak van de drager propageren. Voorbeelden van de laatste variant zijn watergolven en zogenaamde Rayleigh golven in de seismiek, een van de vier mogelijk seismische golven (zie Fig. 1). In beide gevallen gaat het oppervlak (van het water of van de aardkorst) op en neer en de afzonderlijke volume-eenheden doorlopen een elliptisch pad.



Figuur 1. Golven in de natuur.

Ook elektromagnetische golven kunnen zich strikt langs het grensvlak van twee media voortplanten. Een bekend voorbeeld zijn de Sommerfeld of Zenneck golven: radiogolven met een golf lengte van 100 tot 1000 meter, die als het ware langs het oppervlak van de aarde scheren. Soortgelijke golven spelen een hoofdrol in dit proefschrift: oppervlakte-elektromagnetische golven aan het grensvlak tussen edelmetalen en lucht of glas. Deze heten *oppervlakteplasmonen*. Deze elektromagnetische oppervlaktegolf is verknoopt met een longitudinale golfbeweging van de oppervlakteladingsdichtheid met gelijke golflengte en frequentie.

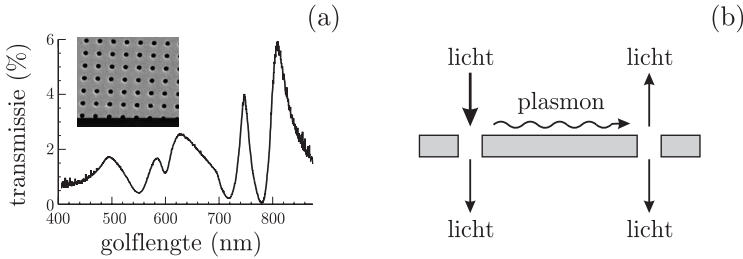


Figuur 2. Configuratie voor het aanslaan van een oppervlakteplasmon aan een metalen oppervlak.

Een oppervlakteplasmon is bijzonder omdat het een puur twee-dimensionaal golfverschijnsel is: in de richting loodrecht op het oppervlak spreidt de golf zich nauwelijks uit en vervalt binnen een afstand van de orde van de golflengte (in lucht) of veel kleiner (in het metaal) (zie Fig. 2). Door die zeer beperkte uitgebreidheid is het oppervlakteplasmon erg gevoelig voor de eigenschappen van het materiaal boven op het metaal en voor de vlakheid van dat oppervlak. Vanwege deze gevoeligheid worden oppervlakteplasmonen toegepast als ‘probe’ van oppervlakken.

Een tweede consequentie van de zeer beperkte uitgebreidheid van het oppervlakteplasmon in de richting loodrecht op het oppervlak is dat het elektrische veld van dat plasmon sterk opgeslingerd is: als je een lichtbundel efficiënt in een oppervlakteplasmon kan omzetten dan is het elektrische veld van dat plasmon veel (een factor van 10–100) groter dan het elektrische veld van de invallende lichtbundel. Deze opslinging is aantrekkelijk bijvoorbeeld voor niet-lineair optische verschijnselen.

De belangstelling voor oppervlakteplasmonen heeft enkele cycli doorlopen. Het begon allemaal met Robert Wood’s waarneming dat het spectrum van een witte lichtbron, uiteengerafeld met behulp van een metalen tralie, donkere lijnen bevat. Sommige kleuren waren als het ware verdwenen. Dit verschijnsel staat bekend als de anomalie van Wood en wordt tegenwoordig verklaard in termen van het, bij die specifieke golflengtes, resonant aanslaan van oppervlak-



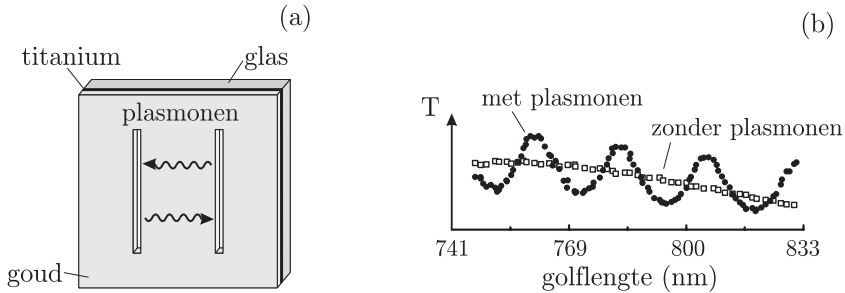
Figuur 3. (a) Licht transmissie door een metalen film met een raster van gaatjes; (b) Licht \rightarrow plasmon \rightarrow licht koppeling bij de gaatjes.

teplasmonen aan het metalen tralie. De meest recente cyclus in de interesse voor oppervlakteplasmonen is aangezwengeld door het werk van de groep van Ebbesen aan de licht-transmissie eigenschappen van metaalfilms die doorboord waren met duizenden minuscule gaatjes (zie Fig. 3a). Als die gaatjes willekeurige posities innemen is de transmissie erg klein, geheel in overeenstemming met algemeen geaccepteerde theoretische modellen. Als de gaatjes echter een regelmatig patroon vormen is de licht-transmissie vele malen groter. Voor zo'n regelmatige structuur vertoont de licht-transmissie als functie van de golflengte van het opvallende licht ook sterke variaties: bij sommige golflengten is de transmissie echt hoog en bij andere golflengten verwaarloosbaar klein. In wezen is zo'n regelmatig gaatjespatroon zoals gebruikt door de groep van Ebbesen niets anders dan een twee-dimensionaal metalen tralie, en het is dus niet verwonderlijk dat oppervlakteplasmonen naar voren werden geschoven om de anomale transmissie-eigenschappen te verklaren. Enerzijds laten de gaatjes een klein beetje licht door; anderzijds zorgen zij voor een koppeling tussen het invallende licht en oppervlakteplasmonen met een welbepaalde golflengte en voortplantingsrichting (zie Fig. 3b). Laatstgenoemden kunnen ook weer terugstrooien naar licht, opnieuw aan de gaatjes.

Dit onderzoek was als het ware een lont die een kruitvat aanstak: een ware waterval van onderzoeken en publicaties volgden op het gebied van gestructureerde metaal films en hun respons op invallend licht. Dit onderzoeksgebied wordt tegenwoordig “plasmonics” of “nano-plasmonics” genoemd.

In eerste instantie ging een groot deel van de belangstelling uit naar metallische structuren die, net als die van de groep van Ebbesen minuscule, op regelmatige afstand geboorde gaatjes bevatten. De gaatjes waren bijvoorbeeld rond, vierkant, rechthoekig of ellipsvormig en elke structuur vertoonde zijn eigen speciale karakteristieken. Men kon ook sleutelen aan de diameter van de gaatjes of de metaalfilm inpakken of een heel ander golflengtegebied

bestuderen. Er werd veel gepubliceerd en er was erg veel discussie over de interpretatie van de meetresultaten. In de toepassing van de theorie werd door velen het sterk gestructureerde metaaloppervlak behandeld alsof het geheel vlak en ongestructureerd was; dit veroorzaakte de nodige controverse. Nieuwe modelbeschrijvingen werden gelanceerd en de discussie raakte behoorlijk verhit. Het was tijd voor een vereenvoudiging.



Figuur 4. (a) Dubbelspleet in een dunne goudfilm; (b) Twee-spleet transmissie spectrum.

Taco Visser kwam met een elegant voorstel: neem een metaalfilm, frees daarin twee smalle lange parallelle spleten die op enige afstand van elkaar staan (Fig. 4a) en meet het transmissie spectrum van die geperforeerde film (Fig. 4b). Als de spleten voldoende smal zijn en de spleetafstand is goed gekozen dan zal door toedoen van de oppervlakteplasmonen de transmissie van deze film als functie van de golflengte van het invallende licht op en neer gaan. Het aardige is dat de twee-spleten geometrie, zoals hier voorgesteld, een van de kanonieke geometriën van de natuurkunde is. Zij heeft bijgedragen aan de ontwikkeling van de golfbeschrijving van licht en is ook van groot belang in de context van het begrip van de quantum mechanica. Het twee-spleten experiment staat dan ook in elk natuurkunde studieboek en is bekend als het experiment van Young.

Het elegante van dit voorstel is dat het aanslaan, het zich voortplanten en het de-exciteren van het oppervlakteplasmon goed ruimtelijk gescheiden zijn. Het aanslaan en het de-exciteren gebeurt aan de spleten en de voorplanting over een vlak stuk metaal daartussen.

Dit voorstel van Visser vormt de basis van het in dit proefschrift beschreven onderzoek. In **hoofdstuk 2** rapporteer ik over de metingen aan een systeem bestaande uit: een 200 nm dikke goudfilm met daarin twee 200 nm brede, 50 μm lange spleten op een onderlinge afstand van 5, 10, 15, 20 of 25 μm . Die goudfilm hangt niet los in de ruimte maar is door middel van een titani-

um hechtlaag gebonden aan een substraat van glas. Het experiment bevestigt de theoretische voorspelling, namelijk dat het transmissiespectrum van een dubbelspleet een modulatie vertoont (Fig. 4b). Deze modulatie wordt veroorzaakt doordat een deel van het op de spleten invallende licht coherent omgezet wordt in oppervlakteplasmonen, die bij aankomst bij de andere spleet gedeeltelijk weer in licht worden omgezet, opnieuw door een coherent, dat wil zeggen fasebehoudend verstrooiingsproces. Bij elk van de spleten ontstaat interferentie van, enerzijds, het direct op die spleet invallende licht, en anderzijds, het licht dat via plasmonische koppeling afkomstig is van de andere spleet. Deze interferentie in de spleet is verantwoordelijk voor de waargenomen spectrale modulatie.

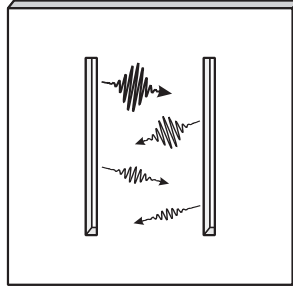
Bij interferentie hoort een faserelatie. Het is duidelijk dat de faserelatie bepaald wordt door het product van spleetafstand en golfgetal (propagatie constante) van het oppervlakteplasmon. Maar is er meer? Elke verstrooiingsgebeurtenis, bijvoorbeeld de partiële omzetting van het invallende licht in een oppervlakteplasmon, kan een fasesprong veroorzaken. Die fasesprong heeft gevolgen voor de positie van de maxima en minima in het transmissie spectrum. Theoretische berekeningen toonden aan dat de fasesprong voor het dubbele verstrooiingsproces “licht in de vrije ruimte \rightarrow oppervlakteplasmon \rightarrow licht in de spleet” gelijk is aan π . Onze experimentele nauwkeurigheid was niet groot genoeg om dat te bevestigen of te weerleggen.

Dit eerste experiment, beschreven in hoofdstuk 2, gaf onmiddellijk aanleiding tot een nieuw experiment (**hoofdstuk 3**). Hierin werden niet beide spleten belicht maar slechts één van de twee. Dat vereist de nodige zorg omdat je al gauw bij het focuseren van een laserbundel last kan krijgen van buigingsringen, waardoor onbedoeld een beetje licht op de tweede spleet valt. Op grond van het boven beschreven dubbele verstrooiingsmechanisme verwacht je nu dat je, ondanks het belichten van maar één spleet, toch een twee-spleten interferentiepatroon kan waarnemen. Wij nemen dat inderdaad waar; het patroon heeft een aantal ongewone eigenschappen.

Merk op dat dit betekent dat, als je een afbeelding maakt van de dubbelspleet, bijvoorbeeld met een microscoop, dan je dan licht uit beide spleten ziet komen: veel uit de belichte spleet, weinig uit de niet-belichte spleet (zie hoofdstuk 1, Figuur 1.6).

Als je een interferentiepatroon kan waarnemen als je maar één spleet belicht dan moet je ook een interferentiepatroon kunnen waarnemen als je beide spleten belicht maar elk met een andere lichtbron. Je kan dat ook anders formuleren: het licht dat op de ene spleet valt hoeft geen enkele faserelatie te hebben met het licht dat op de andere spleet valt en toch krijg je een inter-

ferentiepatroon. Het experiment toont aan dat deze gedachtegang correct is: de plasmonen zorgen voor coherentie aan de uitgang van de spleten terwijl die totaal afwezig is aan de ingang van de spleten.

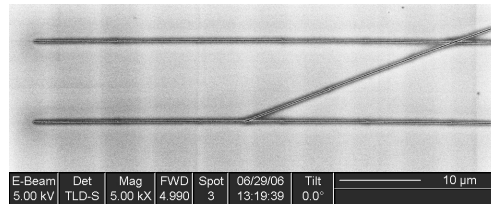


Figuur 5. Oppervlakteplasmon impuls kaatsen heen en weer tussen twee spleten.

Ook **hoofdstuk 4** vindt zijn oorsprong in de metingen van hoofdstuk 2. Het daar waargenomen spectrum vertoont een modulatie patroon dat net niet sinusvormig is; de pieken zijn een beetje smaller dan de dalen. Dit suggereert dat het oppervlakteplasmon als het bij een spleet arriveert ook teruggestrooid wordt, zeg maar teruggekaatsd, maar voor slechts een kleine fractie (zie Fig. 5). In hoofdstuk 4 bestudeer ik dit kaatsgedrag van oppervlakteplasmonen gebruik makend van smalle spleten die zowel als bron, afvoerkanaal en spiegel dienst doen. Ondanks het feit dat de weerkaatsingscoëfficiënt klein is (≈ 0.04) kunnen we, met behulp van een interferometrische techniek, vier weerkaatsingen van een oppervlakteplasmon waarnemen. De metingen geven ook informatie over de groepssnelheid van een oppervlakteplasmon. Ook in dit experiment spelen fasesprongen bij verstrooiing, in dit geval weerkaatsing, een rol. Wij vinden dat deze weerkaatsings fasesprong gelijk is aan die van het eerder besproken dubbele verstrooiingsproces.

Als beide spleten door het invallende licht worden beschonen zullen zij allebei oppervlakteplasmonen lanceren. Tussen de twee spleten ontstaat dan een staande plasmogolf. De periodiciteit hiervan is gelijk aan de halve plasmon golflengte, in ons geval ≈ 250 nm. Om deze staande plasmon golf waar te nemen moeten wij een truc uithalen (**hoofdstuk 5**). Ten eerste moeten wij het oppervlak tussen de twee spleten, bijvoorbeeld door middel van een extra spleet, verstoren zodanig dat de plasmonen gaan afstralen. Ten tweede moeten wij ervoor zorgen dat wij een meetinstrument gebruiken met voldoende ruimtelijk oplossend vermogen. Aangezien de plasmonen zullen afstralen bij 800 nm (de golflengte van het oorspronkelijk op de spleten invallende licht)

is er een probleem. Met normale verre-veld microscopie kan je geen 250 nm structuren bij een golflengte van 800 nm oplossen. Wij hebben ervoor gekozen om tussen de twee spleten een smalle schuine spleet aan te brengen (zie Fig. 6). Deze zorgt voor de noodzakelijke verstoring van het plasmonveld om iets te kunnen zien en, omdat hij schuin staat, rekt hij het patroon als het ware uit (in ons geval met een factor 6).



Figuur 6. Drie spleet afbeelding.

Door middel van deze schuine spleet kunnen wij, in principe, de staande plasmogolf onderzoeken. Omdat er ook een deel van het invallende licht door de schuine spleet sijpelt ontstaat er nog een ander, veel helderder, interferentiepatroon in het door de schuine spleet doorgelaten licht. Gelukkig kunnen wij dat laatste patroon onderdrukken door de golflengte van het invallende licht geschikt te kiezen en kunnen wij de staande plasmogolf alsnog waarnemen. Ons sample is zo gemaakt dat de twee parallelle spleten waar tussen de schuine spleet loopt nog een heel stuk doorlopen voorbij het gebied waar de schuine spleet ligt. Als wij de lichttransmissie van dit deel van het sample meten zien we dat deze transmissie maximaal wordt bij precies die golflengten waar het staande-golfpatroon in de schuine spleet zichtbaar wordt. Deze correlatie biedt ons de mogelijkheid de fase van het verstrooiingsproces “invallend-licht \rightarrow oppervlakteplasmon \rightarrow licht door de spleet” experimenteel te bepalen. Wij vinden een waarde π , geheel in overeenstemming met de theoretische voorspellingen.

Met dit sample kunnen wij ook de waarschijnlijkheid meten dat het plasmon over een spleet heen ‘springt’ en de daarmee gepaard gaande fasevertraging. Alles bij elkaar levert het ons een vrij compleet beeld op van de wisselwerking van een oppervlakteplasmon met een spleet.

In **hoofdstuk 6** komt een intrigerend resultaat van onze allereerste metingen aan bod. Bij de metingen van hoofdstuk 2 gebruiken wij spleten met een breedte van 200 nm in een 200 nm dikke goudfilm. Wij verwachtten dat deze spleten een veel kleinere lichttransmissie zouden hebben voor licht gepolariseerd parallel aan de spleten dan voor licht gepolariseerd loodrecht op

de spleten. Dat bleek, tot onze verassing, niet waar te zijn. Nog verrassender vonden wij het feit dat als we licht op de spleten lieten vallen bij een golflengte van 800 nm met een polarisatie onder 45 graden met de spleet, het doorgelaten licht circulair gepolariseerd is (en vice versa). De spleten werken als het ware als een $\lambda/4$ -plaatje, bekend uit de kristal-optica. Om deze waarnemingen beter te begrijpen hebben we een experiment gedaan aan een grote serie enkele spleten met steeds toenemende spleetbreedte, van 50 nm tot 1000 nm. Wij hebben daarmee de niet-triviale variatie van de transmissie coëfficiënt als functie van de spleetbreedte zorgvuldig in kaart gebracht voor beide hoofdrichtingen van de polarisatie van het licht. Wij hebben onze metingen vergeleken met resultaten van numerieke berekeningen op grond van een diffractie model en vinden prima overeenstemming.

In **hoofdstuk 7** rapporteer ik over een experiment aan zilver. Goud is geel en zilver is wit; dat kleurverschil zegt iets over de respons van beide materialen op invallend licht: in het blauwe deel van het spectrum gedraagt zilver zich nog netjes als een "tekstboek"metaal, goud doet dat helemaal niet. Omdat zilver, als het aan lucht wordt bloot gesteld, snel dof wordt, wordt het metaal ingepakt tussen glas en een dunne chroomlaag. Wij bestuderen de oppervlakteplasmonen aan het grensvlak van zilver en glas. Als nieuwigheid bestuderen we deze oppervlakteplasmonen over een heel groot spectraal gebied, van het blauw-groen tot in het infrarood. De metingen in het blauw-groene deel van het spectrum zijn bijzonder: de golflengte van het oppervlakteplasmon is daar ongehoord klein (≈ 260 nm).

Интерференционные эффекты с поверхностными плазмонами

Волны в природе

Волны и волновые процессы окружают нас. Мы слышим звуки, доносимые до нас звуковыми волнами, мы видим волны на поверхности воды, мы ощущаем сейсмические волны, мы широко используем волны электромагнитные: радиоволны, световые волны, рентгеновские волны и т.д. Волновые движения можно условно разделить на два подкласса: волны, распространяющиеся внутри среды (объемные волны), и волны, распространяющиеся на поверхности среды, т.е. на границе раздела сред (поверхностные волны). Примерами поверхностных волн в природе могут служить волны на поверхности воды и поверхностные сейсмические волны Рэлея (см. Рис. 1). В обоих случаях частицы на поверхности среды описывают эллиптические траектории.



Рис. 1. Волны в природе.

Электромагнитные волны также могут распространяться вдоль границы раздел сред. Хорошо известными примерами таких волн являются радиоволны Зоммерфельда, длиной от 100 до 1000 метров, распространяющиеся около или по поверхности земли.

Поверхностные плазмоны

Свойства поверхностных плазмонов

Поверхностные электромагнитные волны играют главную роль в данной диссертации. Это электромагнитные волны, распространяющиеся вдоль границы раздела металла и диэлектрика (воздуха или стекла). Эти волны называются *поверхностными оптическими волнами* или *поверхностными плазмонами* (ПП). Они представляют собой совместное колебание плотности свободных электронов внутри металла и электромагнитной волны в диэлектрике, колебание, локализованное у границы раздела этих сред. Особенностью поверхностного плазмона является его чисто двумерная природа: ПП распространяется только вдоль границы раздела и его поле быстро затухает при удалении от этой границы (см. Рис. 2).



Рис. 2. Возбуждение поверхностного плазмона на поверхности металла.

Вследствие этого свойства поверхностного плазмона напрямую зависят от свойств поверхности, по которой он распространяется. Оптические свойства металла и диэлектрика, а так же рельеф границы раздела будут целиком определять скорость распространения поверхностного плазмона, зависимость этой скорости от длины волны (дисперсию ПП), а так же затухание плазмона. Другим следствием двумерной природы поверхностного плазмона является то, что свободно-распространяющаяся электромагнитная волна, переходя в поверхностный плазмон, сосредотачивается в тонком приповерхностном слое, и ее амплитуда увеличивается в десятки-сотни раз. Такое значительное усиление локального поля поверхностным

плазмон является привлекательным для изучения нелинейных оптических эффектов, интенсивность которых растет пропорционально квадрату (кубу и т.п.) возбуждающего поля¹.

История открытия и изучения поверхностных плазмонов

Интерес к поверхностным плазмонам развивался циклически. В начале прошлого века английский физик Роберт Вуд обнаружил темные линии в спектрах дифракции белого света на металлических решетках: некоторые цвета, составляющие белый спектр, не испытывали отражения. Это явление получило название Вудовской аномалии. В сороковых годах прошлого века это явление получило объяснение в работах итальянского физика-теоретика Уго Фано, предположившего существование поверхностных волн, резонансно возбуждаемых определенными длинами волн падающего света на поверхности решетки, и препятствующих последующему отражению этих длин волн. В шестидесятых годах прошлого века были сформулированы условия существования ПП и схемы их возбуждения (А. Отто, Е. Кретчманн). В шестидесятые-семидесятые годы поверхностные плазмоны активно изучались в предложенных геометриях Отто и Кретчманна, использовавших эффект увеличения волнового вектора света, прошедшего через стеклянную призму, что позволяло возбуждать поверхностные плазмоны и исследовать их характеристики на гладких и шероховатых поверхностях.

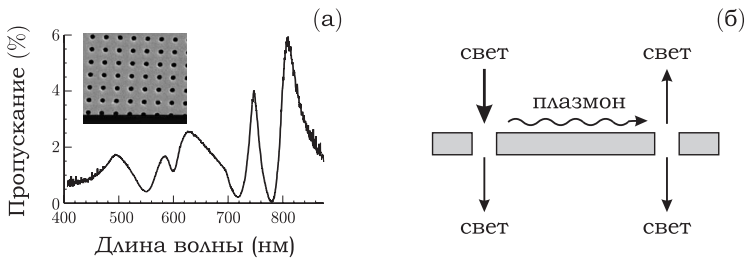


Рис. 3. (а) Спектр пропускания перфорированной металлической пленки; (б) Преобразование “свет→плазмон→свет” на отверстиях в металлической пленке.

Недавний всплеск интереса к поверхностным плазмонам был вызван работой группы французского ученого Томаса Эббесена (1998 г.), в которой изучались спектры пропускания металлических пленок, перфори-

¹) которым, в данном случае, является интенсивное поле поверхностного плазмона

рованных множеством крохотных отверстий с диаметром много меньше длины волны падающего света (см. Рис.3а). В случае, когда местоположение отверстий на пленке носило случайных характер, количество света, прошедшего через них, было незначительным, и хорошо описывалось общепринятыми теоретическими моделями, объясняющими распространение света через единичное отверстие. В случае же, когда расположение отверстий было строго упорядоченным — отверстия находились в узлах квадратной сетки, пропускание света через такую систему возрастало во много раз. Это возрастание, однако, происходило только для определенных длин волн падающего света, пропускание же остальных длин волн было таким же незначительным. Иначе говоря, спектр пропускания упорядоченной системы отверстий имел резонансный характер с аномально большим пропусканием в максимумах и глубокими минимумами (см. Рис.3а).

Такая система отверстий представляла собой не что иное, как двумерную дифракционную решетку Вуда, и не удивительно, что аномально большое пропускание света нельзя было бы описать с помощью феномена поверхностных плазмонов. С одной стороны, прямое пропускание света через отверстия весьма мало. С другой же стороны, отверстия рассеивали падающий на них свет в поверхностные плазмоны, которые, как предполагалось, были ответственны за резонансное усиление пропускания.

За работой Эббесена последовала целая серия теоретических и экспериментальных исследований, посвященных физике структурированных металлических пленок и их взаимодействию со светом. Эта новая область исследований получила название “плазмоника” или “нано-плазмоника”. В первую очередь, интерес был сосредоточен на структурах, подобных эббесеновской, а именно, металлических пленках, перфорированных сериями равноотстоящих нано-отверстий различного диаметра и формы: круглой, эллиптической, квадратной, прямоугольной. Их свойства исследовались не только в оптическом, но и в инфракрасном и микроволновом диапазонах, и значительным образом зависели от формы отверстий, геометрии их расположения, длины волны и поляризации падающего излучения, а так же свойств металла. Было так же опубликовано множество теоретических работ, в которых делались попытки приближенно описать рассматриваемую систему. В таких работах поверхностные плазмоны рассматривались на гладких поверхностях, и влияние отверстий на дисперсию поверхностных плазмонов не учитывалось¹, что приводило к рассогласованию теоретических и экспериментальных результатов. Предлагались новые модели, объяснявшие одни аспекты, но испытывающие затруднения в других, тон

¹) Аналитически, такой учет является крайне сложным.

дискуссий накалялся, и было необходимо внести упрощение, прежде всего в экспериментально-рассматриваемую систему.

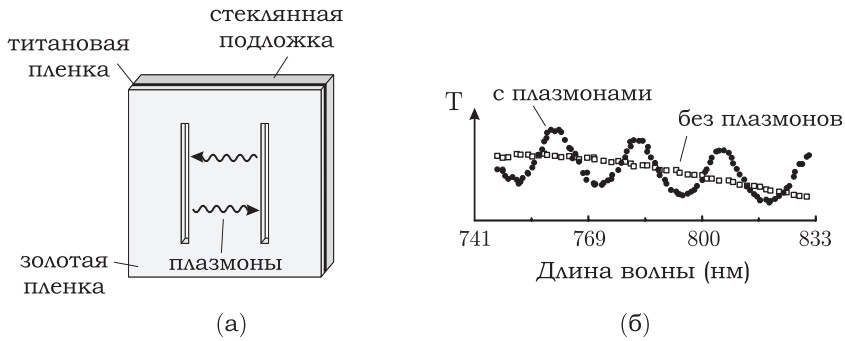


Рис. 4. (а) Система двух параллельных щелей в тонкой золотой пленке; (б) Спектр пропускания данной системы.

Поверхностные плазмоны и двущелевая система в металлической пленке

В 2003 году Тако Фиссер (Свободный Университет Амстердама) теоретически рассмотрел намного более простую систему, состоящую всего лишь из двух узких параллельных щелей в металлической пленке, расположенных на некотором расстоянии друг от друга (см. Рис.4а). В зависимости от поляризации падающего излучения смоделированный спектр пропускания такой системы состоял либо из периодических равноотстоящих максимумов, либо не имел ярко выраженных особенностей (см. Рис.4б). Фиссер связал это с наличием поверхностных плазмонов, распространявшихся между щелями и интерферировавших со светом, напрямую распространявшимся через них.

Важно отметить, что система двух щелей в непрозрачном экране является канонической системой физики. Она послужила английскому физику Томасу Юнгу для доказательства волновой природы света, а так же сыграла важную роль в понимании многих аспектов квантовой механики при изучении интерференции электронов, атомов и молекул.

С точки зрения физики поверхностных плазмонов привлекательностью данной системы является то, что каждая щель является как источником, так и приемником поверхностных плазмонов (Рис.3б). Более того, так как длина щели предполагается много больше длины волны падающего света, то щель представляет собой антенну, переизлучающую падающую на нее

световую волну в направленную волну поверхностных плазмонов, распространяющуюся перпендикулярно щели по поверхности металла (Рис.4а). Это дает возможность расположить вторую щель-приемник на достаточно большом расстоянии от щели-источника, что позволяет поверхностным плазмонам распространяться по плоской, невозмущенной поверхности металлической пленки, где свойства поверхностного плазмона могут быть описаны в простой аналитической форме.

Тема и содержание диссертации

Система, состоящая из двух и более щелей в различных металлических пленках, легла в основу данной диссертации. Целью диссертации было исследование возможности возбуждения ПП в двущелевой системе, измерение эффективности и фазовых характеристик данного процесса, исследование дисперсии и затухания ПП и т.д.

Экспериментальные исследования были проведены в Лейденском университете под руководством профессора Херта Хоофта и доктора Эрика Элиэля. Теоретическое моделирование делалось в соавторстве с доктором Тако Фиссером и Хьюго Схаутеном (Свободный Университет, Амстердам), а так же профессором Полом Урбахом и Олафом Янсенем (Технический Университет, Дельфт). Экспериментальные образцы были изготовлены при содействии доктора Пола Алкемаде (Технический Университет, Дельфт).

Экспериментальные образцы

Экспериментальные образцы, исследованные в данной диссертации, состояли из золотых и серебряных пленок толщиной 200 нм^1 , напыленных на стеклянные подложки, размерами $18 \times 18 \times 0.5 \text{ мм}$. Толщина пленки выбиралась таким образом, чтобы с одной стороны быть много больше глубины скин-слоя (глубины проникновения поля в металл), а с другой стороны быть меньше половины длины волны возбуждающего света, чтобы исключить резонансный характер пропускания щели. Резонансы в пропускании возникают из-за того, что щель в достаточно толстой пленке (больше половины длины волны) может вести себя как резонатор Фабри-Перо: световая мода, распространяющаяся внутри нее испытывает множественные отражения на границе щель-воздух, эти отражения интерферируют

¹) 1 миллиметр (мм) = 1000 микрометров (микрон, мкм) = 1,000,000 нанометров (нм)

между собой, и спектр пропускания щели становится резонансным. Отражения происходят из-за того, что значение постоянной распространения моды внутри щели превосходит показатель преломления воздуха, равный единице.

Критерием выбора золота и серебра, как основных металлов для производства пленок, служило то, что ПП на данных металлах обладают в видимом оптическом диапазоне сравнительно небольшим затуханием и распространяются на расстояния до сотни микрон. Преимуществом золота является то, что оно не окисляется на воздухе, поэтому удобно рассматривать ПП на границе раздела золото-воздух. Преимуществом серебра, в отличие от золота, является отсутствие поглощения в сине-зеленой области видимого спектра¹, что позволяет наблюдать “синие” ПП, поле которых сосредоточено больше в металле, чем в диэлектрике, и поэтому они обладают большой дисперсией и затуханием. Такие плазмоны представляют интерес для интегрированных нано-цепей, где необходима сверхмалая длина волны ПП.

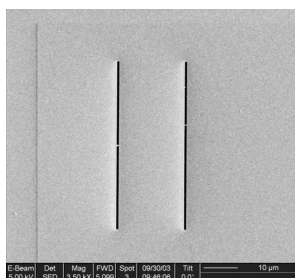


Рис. 5. Изображение поверхности экспериментального образца со щелями, полученное с помощью электронного сканирующего микроскопа.

С помощью сфокусированного пучка ионов галлия в золотых и серебряных пленках были изготовлены двущелевые системы различных размеров. Длина щелей составляла 50 мкм, ширина каждой щели составляла 100–200 нм, а расстояние между щелями изменялось от нескольких микрон до десятков микрон.

Ширина щели выбиралась таким образом, чтобы эффект ПП был наи-

¹) Так как серебро является металлом во всем видимом световом диапазоне, то есть действительная часть его диэлектрической проницаемости меньше нуля, то оно одинаково отражает все цвета видимого спектра и выглядит белым. Золото же перестает быть металлом и становится диэлектриком уже в сине-зеленой части видимого спектра и поэтому имеет характерный желтый цвет в отражении и сине-зеленый на просвет.

более заметен на фоне прямого пропускания света через щель. Как выяснилось позже, преобразование падающего света в плазмон напрямую зависело от ширины щели, и было наиболее оптимальным, когда ширина щели составляла около четверти длины волны падающего света, то есть около 200 нм.

Расстояние между щелями выбиралось таким образом, чтобы оно с одной стороны было: а) много больше, чем длина волны падающего света, для исключения влияния щели на характер распространения ПП по гладкой металлической поверхности, и б) было меньше, чем длина затухания ПП. К примеру, длина затухания ПП с длиной волны 800 нм, распространяющегося по границе раздела воздух-золото, составляет около 100 мкм. На этой длине напряженность поля ПП падает в $e \simeq 2.7183$ раз.

Стоит упомянуть два различных механизма, определяющих затухание ПП: излучательный и безызлучательный, когда энергия плазмона переходит или в свет или в тепло. Излучательное затухание происходит, когда ПП рассеивается обратно в свет на шероховатостях поверхности, по которой он распространяется. На абсолютно гладких поверхностях излучательное затухание отсутствует. Безызлучательное затухание имеет место всегда, даже когда ПП распространяется по гладкой поверхности раздела — его причиной служит рассеяние ПП на кристаллической решетке металла, приводящее к ее разогреванию.

В образце с золотой пленкой были так же изготовлены системы из трех щелей в форме буквы Z: две щели, параллельные друг другу и одна наклонная щель, пересекающая их под углом ~ 10 град. Наклонная щель служила пробником для стоячей волны, образованной поверхностными плазмонами, распространяющимися друг навстречу другу между параллельными щелями. В подобном образце были сделаны и одиночные щели различной ширины для изучения поведения мод светового поля в них.

Эксперименты и результаты

Для исследования образцов с различными щелевыми структурами было создано несколько экспериментальных установок. Ниже приводятся схемы установок и обсуждаются результаты экспериментов.

Спектры пропускания

Глава 2. Идеей первого эксперимента была проверка существования ПП в двущелевой системе. В качестве источника света использовался титан-

сапфировый лазер с возможностью перестройки длины волны в небольшом диапазоне 740–830 нм. Пучок диаметром около 1 мм равномерно освещал исследуемую двущелевую систему в экспериментальном образце и свет, прошедший через щели собирался системой линз на фотодиодный детектор (Рис.6). Сигнал детектора записывался регистрационной системой как функция длины волны падающего света.

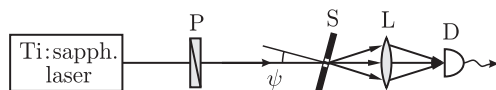


Рис. 6. Схема экспериментальной установки: титан-сапфировый лазер, P — поляризатор, S — образец, L — система линз, D — детектор.

Полученные спектры пропускания двущелевых систем (см. Рис.4б) представляли гармонические (почти синусоидальные) зависимости, хорошо согласующиеся с теоретическими расчетами Т. Фиссера. Для доказательства того, что такая модуляция спектра пропускания была вызвана именно плазмонами, были проделаны дополнительные эксперименты. В первом из них поляризация падающего на щели света, то есть направление электрического вектора, была выбрана параллельно щелям, в отличие от основного эксперимента, где она была перпендикулярна щелям. Для такой поляризации не должно было происходить возбуждения ПП. Действительно, спектр пропускания в этом случае не содержал никаких выраженных особенностей и слабо зависел от длины волны (см. Рис.4б). Аналогичный спектр для обеих поляризаций падающего света наблюдался и в случае, когда исследовалось пропускание сквозь щели, изготовленные в титановой пленке. Титан хотя и поддерживает ПП в рассматриваемом диапазоне длин волн, но длина затухания ПП составляет меньше одного микрона, то есть много меньше расстояния между щелями, и влияние ПП сводится к нулю.

Измеренные спектры пропускания хорошо описывались простой моделью, рассматривавшей интерференцию света напрямую прошедшего через щель и ПП, сгенерированного другой щелью и падающего на данную щель. Так как фаза этого плазмона, прошедшего от щели-источника к щели-приемнику зависела от длины волны падающего света, то для определенных длин волн имела место конструктивная/деструктивная интерференция между световым и плазмонным каналами, результатом чего был максимум/минимум в спектре пропускания. По амплитуде модуляции сигнала в спектре пропускания была определена относительная амплитуда плазмонного канала по сравнению с прямым световым каналом. Она со-

ставила около 20%. Помимо того, из теоретических расчетов напряженности электромагнитного поля ПП вокруг щелей следовало, что между ними образуется стоячая волна, сформированная поверхностными плазмонами, распространяющимися друг навстречу другу (Рис.7). Это предположение экспериментально исследовано в Гл.5. Таким образом, в данной главе было однозначно показано наличие поверхностных плазмонов в двущелевой системе и их влияние на пропускание света через нее.

Глава 7. В Главе 7 исследован спектр (дисперсия) поверхностных плазмонов в гораздо более широком диапазоне длин волн — от синей области видимого диапазона (~ 450 нм) до ближней инфракрасной области (~ 1300 нм). ПП изучались на границе стекло-серебро на двущелевых системах с шириной щелей 100 нм и расстоянием между щелями 8 и 25 мкм. Источником света служил волоконный лазер Fianium с ультра-широким спектром излучения (450–1700 нм) и выходной мощностью около 2 Вт. В данном эксперименте, однако, использовалась лишь небольшая часть мощности лазера. Свет, прошедший через щели собирался системой линз на входной апертуре волоконного спектрометра, позволявшего измерять интенсивность всех спектральных компонент одновременно. Полученные спектры пропускания позволили рассчитать дисперсию и групповую скорость ПП. В синей части диапазона ПП распространялся со скоростью примерно в три раза меньше скорости света в вакууме. Длина волны этого коротковолнового плазмона составила всего около 260 нм.

Интерференция в дальнем поле (Глава 3)

В данной главе рассматривалось влияние ПП на пространственную когерентность светового поля, переизлучаемого щелями. Изучалось распреде-

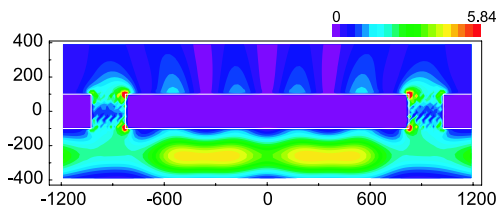


Рис. 7. Моделирование распределения интенсивности электромагнитного поля в системе: отчетливо видна стоячая волна на поверхности металла между щелями, образованная плазмонами, распространяющимися друг навстречу другу.

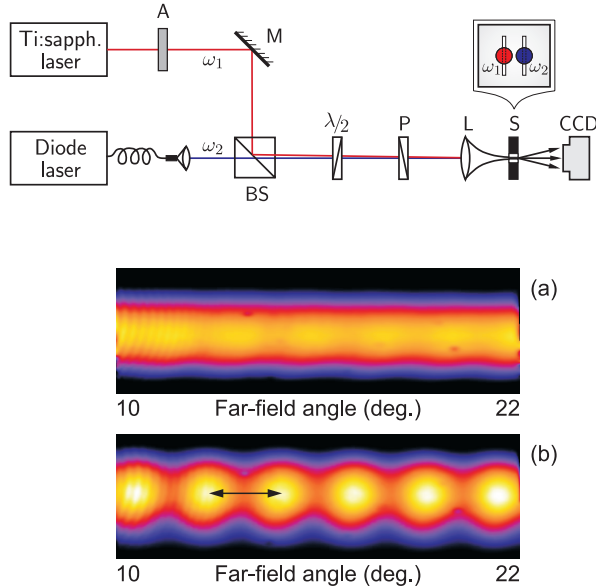


Рис. 8. Схема экспериментальной установки и распределения интенсивностей интерференционных картин в дальнем поле для различных частот падающего излучения ($\omega_{1,2}$). В случае а) модуляция интенсивности поля равна нулю, в случае б) она максимальна.

ление интенсивности света, прошедшего через щели, на достаточном от них удалении (~ 10 см), то есть в дальнем поле. Для возбуждения ПП использовались два взаимно-некогерентных лазера¹ с немного отличающимися длинами волн, пучки которых освещали только одну щель каждый: пучок первого лазера освещал левую щель, а пучок второго лазера — правую щель (Рис.8). При этом на экране наблюдалась стабильная интерференционная картинка с синусоидальным распределением интенсивности, модуляция которой зависела от длин волн лазеров, один из которых можно было перестраивать. Наблюдаемый эффект, таким образом, заключался в том, что, будучи освещенными некогерентными полями, щели излучали поля когерентные и степень когерентности зависела от длин волн этих полей. Более того, при изменении поляризации лазерного света, освещающего обе щели, с перпендикулярной щелям на параллельную, при которой возбуждения ПП не происходило, модуляция в интерференционной картинке становилась равной нулю.

¹) Пучки таких лазеров не будут давать стабильной интерференционной картинки, так как разность фаз их световых полей непостоянна во времени.

Данный эффект также объясняется наличием ПП между щелями. Суть его заключается в том, что плазмон, распространяющийся от освещенной щели, доставляет часть световой энергии “темной щели” без потери фазы. Темная щель переизлучает этот плазмон на выходной стороне. Таким образом, пучок каждого лазера расщепляется на два источника света: первый, определяемый прямым пропусканием через щель-источник и второй — плазмонный, излучаемый щелью-приемником. Так как процесс рассеяния света в плазмон и обратно происходит с сохранением фазы света, то эти два источника могут давать интерференционную картинку, что и наблюдается в эксперименте. Таким образом, если осветить только одну щель, то на выходе будет наблюдаться интерференционная картина. Когда же освещены две щели, на экране наблюдаются две наложенные друг на друга интерференционные картины. Их поля взаимно-некогерентны и поэтому происходит сложение интенсивностей, а не амплитуд, этих полей. В отличие от классической интерференции Юнга, “плазмонная” интерференционная картинка при перестройке длины волны света перемещается как целое вправо или влево, в зависимости от того, какая щель освещена и от того, увеличивается или уменьшается длина волны света. В случае юнговской интерференции нулевой порядок (максимум) находится в центре интерференционной картины и при перестройке длины волны остается на месте. В случае интерференции с ПП нулевого порядка *не существует*. Это происходит из-за того, что скорость распространения плазмона по поверхности металла (Гл.4) меньше скорости света и нет такого места на экране (угла наблюдения), в котором оптические пути света, излученного “освещенной” и “темной” (плазмонной) щелями, были бы равны. Перестраивая длину волны одного из лазеров можно пространственно сдвигать одну интерференционную картинку относительно другой и наблюдать перечисленные эффекты.

Отклик системы на импульсное воздействие (Глава 4)

В основе данной главы стоит предположение о том, что каждая щель является не только источником и приемником поверхностных плазмонов, преобразуя падающий свет в ПП и обратно, но и плазмонным *зеркалом*. Таким образом, двущелевая система является резонатором типа Фабри-Перо для поверхностных плазмонов, испытывающих множественные отражения от щелей и постепенно затухающих (Рис.9). Множественные отражения влияют как на спектр пропускания такой системы, делая максимумы пропускания более резкими (Рис.4б), так и на временную эволюцию ультракороткого импульса, проходящего через систему двух щелей. От-

кликом системы на импульсное воздействие будет, таким образом, серия затухающих импульсов. Исходя из ранее полученных спектров пропускания (Рис.4б) можно было судить, что возможное количество плазмонных отражений очень невелико, так как ширина максимумов в спектре лишь немного ширины минимумов. Иными словами, коэффициент отражения щели для ПП являлся небольшой величиной. Поэтому, чтобы экспериментально выявить наличие плазмонных отражений, был использован метод импульсного автокорреляционного анализа.

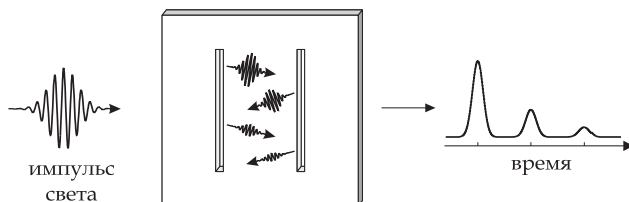


Рис. 9. Множественные отражения плазмонного импульса между щелями и зависимость интенсивности света на выходе из щелей от времени.

Время жизни ПП на границе раздела “воздух-золото” при длине волны возбуждающего света порядка 800 нм составляет несколько сотен фемтосекунд¹. За это характерное время напряженность поля поверхностного плазмона падает в $e \simeq 2.7182$ раз. Таким образом, чтобы “увидеть” поверхностный плазмон во времени, удобно использовать лазер, излучающий ультракороткие импульсы света, длительностью меньше времени жизни ПП. В эксперименте двущелевая система освещалась лазерными импульсами длительностью около 50 фс с перестраиваемой центральной длиной волны 770–805 нм. Свет, прошедший через щели собирался системой линз на фотодиодный детектор. Малое время жизни ПП определяло и систему детектирования, использованную для наблюдения плазмонных отражений. Так как временное разрешение любого детектора много больше времени жизни ПП, то прямое детектирование плазмонных импульсов невозможно. Поэтому, в данном эксперименте был использован корреляционный метод: система освещалась двумя идентичными импульсами — импульсом накачки и сканирующим импульсом, разнесенными во времени. При этом в системе двух щелей возбуждались две серии плазмонных отражений, которые в зависимости от времени задержки интерферировали.

¹) 1 секунда = 1,000 миллисекунд (мс) = 1,000,000 микросекунд (мкс) = 1,000,000,000 наносекунд (нс) = 1,000,000,000,000 пикосекунд (пс) = 1,000,000,000,000,000 фемтосекунд (фс)

Результат их интерференции — свет, прошедший через щели, регистрировался детектором как функция времени задержки, давая сигнал, называемый *интерферограммой*. Интерферограмма состояла из серии равноотстоящих максимумов одинаковой формы и экспоненциально уменьшающейся амплитуды. Расстояние между максимумами равнялось времени, которое было необходимо плазмонному импульсу, чтобы пройти расстояние от одной щели к другой. Это время, порядка нескольких сотен фемтосекунд, в совокупности с известным расстоянием между щелями (50–90 микрон), позволяло непосредственно вычислить групповую скорость ПП, которая составила порядка 90% от скорости света. Как было показано в Гл.7, для коротковолновых плазмонов в синей области видимого диапазона, групповая скорость может составлять всего 30% скорости света.

По амплитудам пиков в интерферограммах были определены амплитудные коэффициенты преобразования “свет→плазмон→свет” (~ 0.20), а так же коэффициент плазмонного отражения от щели, который так же составил порядка 0.20. Это означало, что щель отражает лишь 4% интенсивности падающего на него плазмона обратно в плазмон. Таким небольшим коэффициентом отражения обладает, например, обычное оконное стекло. В практических целях для создания эффективных плазмонных зеркал используются несколько (5–10) равноотстоящих канавок в металлических пленках, глубиной около 50–100 нанометров и периодом, равным половине длины волны ПП. Каждая такая канавка отражает падающий на нее ПП, и отражения ото всех канавок конструктивно интерферируют, давая суммарный коэффициент отражения порядка 80–90%.

Более того, интерферограммы позволили определить разность фаз коэффициента преобразования “свет→плазмон→свет” и коэффициента отражения. Она оказалась равной нулю. Таким образом, как при первом, так и при втором преобразовании, свет испытывал одинаковый скачок фазы. Далее, в одном из экспериментов Главы 6, измеряется абсолютное значение этого скачка.

Распределение интенсивности поля вдоль щелей (Глава 5, 6)

В данных главах исследуются системы, состоящие, в отличие от предыдущих, из одной (Глава 6) и трех щелей (Глава 5). Экспериментальная методика одинакова для обоих экспериментов: исследуемая щелевая система освещаются пучком лазера с однородным распределением интенсивности и фазы по сечению. Длина волны излучения может плавно изменяться в пределах от 740 до 830 нм. Поляризация излучения так же может устанавливаться параллельно, перпендикулярно или под произвольным углом

по отношению к щелям. Изображение системы проецируется с помощью объектива на ПЗС¹ матрицу. Изображение с матрицы передается на компьютер, где оно анализируется. По распределению интенсивности вдоль щелей исследуется амплитуда и фаза света, прошедшего напрямую через щели, а так же вклад поверхностных плазмонов.

Глава 5. Изучаемая система состоит из двух параллельных щелей, пересеченных третьей. Длина щелей составляет 100 мкм, расстояние между ними 10 мкм и наклонная щель пересекает их под углом около 10 градусов (Рис.10). Наклонная щель используется в данном эксперименте как сенсор для стоячей волны, образованной поверхностными плазмонами, распространяющимися друг навстречу друга от параллельных щелей-источников. Подобная стоячая волна образуется и в классическом оптическом резонаторе. Анализ распределения интенсивности светового поля вдоль наклонной щели для различных длин волн в сравнении с амплитудой пропускания через параллельные щели позволял рассчитать абсолютное значение фазы преобразования "свет→плазмон→свет", равное π .

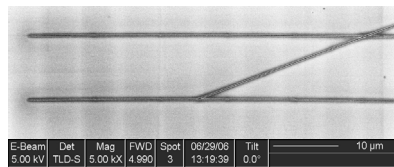


Рис. 10. Изображение трехщелевой системы, полученное с помощью электронного сканирующего микроскопа.

Глава 6. Вопрос, поставленный в данной главе, возник еще в самом начале данного проекта. Как уже было сказано, в Главе 2 изучалась двущелевая система, где рассматривалось "сообщение" между щелями, посредством поверхностных плазмонов.

Для возбуждения ПП поляризация падающего света выбиралась перпендикулярной щели. В случае же, когда поляризация падающего света была параллельна щели, возбуждение ПП не наблюдалось. Физика процесса возбуждения ПП понятна. Электрическое и магнитное поля, составляющие свободно распространяющуюся электромагнитную волну, ориентиро-

¹) ПЗС-матрица — аналоговая интегральная микросхема, состоящая из светочувствительных фотодиодов, выполненная на основе кремния, и на базе ПЗС — приборов с зарядовой связью.

ваны перпендикулярно друг другу и направлению распространения волны. Щели, исследованные в экспериментах, являются одномерными объектами: длина щели много больше ее ширины и может считаться практически бесконечной. Таким образом, при нормальном падении световой волны на щель, можно рассмотреть два основных случая взаимных ориентаций поля и оси щели: 1) электрическая компонента поля перпендикулярна оси щели (поперечная магнитная волна, ТМ); 2) магнитная компонента поля перпендикулярна оси щели (поперечная электрическая волна, ТЕ). Только в случае ТМ волны в ней и в поле ПП имеются однонаправленные компоненты магнитных полей, и может происходить переход энергии от светового поля в поверхностный плазмон.

Одновременно с процессом возбуждения ПП, каждая щель напрямую пропускала падающий на нее свет. Результаты эксперимента Главы 2 показывали, что ТМ и ТЕ поляризованный свет одинаково проходил через щели. Другими словами, коэффициент пропускания щели для ТМ и ТЕ поляризованных волн был практически одинаковым. С точки зрения волноводной теории щель в металлической пленке можно рассматривать как волновод для оптического излучения. Ширина рассматриваемой в эксперименте щели была в четыре раза меньше длины волны падающего света. Граничные условия для электрического и магнитного полей ТЕ волны на границах такой щели-волновода приводят к ее чисто затухающему характеру. При этом ТМ волна остается распространяющейся для любой ширины щели-волновода и ее затухание невелико. Таким образом, в эксперименте наблюдалось аномально большое пропускание ТЕ волны и данный факт не объяснялся простыми представлениями волноводной теории. Более того, линейно-поляризованная волна с направлением поляризации под углом 45° к оси щели, проходя через щель, становилась поляризованной по кругу. Щель, таким образом, работала как четверть-волновая пластинка. Компоненты электрического поля, ориентированные параллельно и перпендикулярно оси пластинки, пройдя через нее, испытывают относительную фазовую задержку, равную $\pi/2$. При этом линейно поляризованный свет с произвольным направлением поляризации относительно оси пластинки, преобразуется ей в свет, поляризованный эллиптически.

С целью объяснения первоначально полученных экспериментальных данных был проделан эксперимент Главы 6, в котором исследовалась ступенчатая щель, ширина элементов которой изменялась от 50 до 500 нм, а длина составляла 10 мкм. Анализ интенсивности и поляризации света, прошедшего через нее показал, что действительно при ширине щели порядка 250 нм ТМ и ТЕ поля обладают одинаковыми коэффициентами

пропускания и их фазовая задержка составляет около $\pi/2$. Для больших ширин щели разность между пропусканием ТЕ и ТМ полей становилась неразличимой, а для меньших ширин затухание ТЕ волны значительно увеличивалось.

Теоретическое объяснение данного эффекта, подтвержденное моделированием, состояло в том, что глубина щели-волновода, или другими словами, толщина золотой пленки, в которой была проделана щель, составляла 200 нанометров, то есть четверть длины волны падающего излучения. Это имело двойное влияние на ТМ/ТЕ пропускание. Во-первых, затухание ТЕ волны было небольшим — волна не успевала испытать значительное затухание на такой небольшой длине волновода. При выходе из щели эта волна снова превращалась в свободно распространяющийся свет. Фаза ТЕ волны при таком распространении не меняется, ввиду ее затухающего характера. Во-вторых, ТМ волна может распространяться через щель-волновод и ее фаза увеличивается как раз на $\pi/2$. Если бы толщина золотой пленки была бы, например, равна 400 нм, это значение составило бы π . Таким образом, щель являлась дихроическим двулучепреломляющим устройством: в ней могли распространяться две волны с ортогональными поляризациями и различным затуханием. Фазы и амплитуды волн, прошедших через щель, зависели от ее ширины и глубины (толщины пленки). Подбирая параметры щели можно было варьировать поляризацию поля, которое проходит через нее.

Заключение

В данной диссертации показана роль поверхностных плазмонов при распространении световых полей через субдлинноволновые щели, измерены эффективности возбуждения и взаимодействия плазмонов со щелями, а так же фазовые портреты данных процессов. Результаты данной работы позволяют более глубоко понять физику взаимодействия поверхностных плазмонов не только со щелями, но и их роль в системах отверстий в металлических пленках. По итогам диссертации опубликовано 3 и планируется к публикации еще 4 статьи. Понимание элементарных процессов взаимодействия света с поверхностными плазмонами в таких системах позволит в дальнейшем конструировать устройства, использующие ПП, например, в качестве эффективных информационных носителей в интегрированных оптических цепях, а так же в качестве усилителей локальных электромагнитных полей в различных нано-системах.

Curriculum Vitae

Nikolay Victorovich Kuzmin

Born on the 28th of January 1980 in the city of Troitsk, Moscow region, Russia, I completed my secondary education in 1997 (Troitsk lyceum) and entered the Physics Faculty of Moscow State University (MSU). After acquiring the bachelor degree, I entered the Optics and Spectroscopy department of the MSU and started my Master project on the optical properties of novel nonlinear crystals for the near infrared range. My Master research has been carried out at the Institute of Spectroscopy of the Russian Academy of Sciences (Troitsk) under supervision of Prof. E.A. Ryabov and Dr. V.B. Laptev.

Starting February 2003, I joined the Quantum Optics and Quantum Information Group at Leiden University (The Netherlands) for a PhD project directed by Prof. G.W.'t Hooft and Dr. E.R. Eliel. I presented some of the results of the project both at the annual conferences in Lunteren and Veldhoven (The Netherlands) and at the international conference in Graz ("Surface Plasmon Photonics 2", Austria, 2005) and Keene (Gordon Research Conference on Plasmonics, NH, USA, 2006). During my stay at Leiden University I taught the lab classes of the LabVIEW course for the second-year bachelor students.

Acknowledgements

At the end of my thesis I want to say a word of thanks to those who contributed to this work and to the nice people who were around during my long and amusing years in the Netherlands.

It has been a great pleasure to work in the Quantum Optics group and I want to express my deep gratitude to the people I've been working with: Guilhem, Anna, Jelmer, Sanli, Barry and Paul; and to the group members: Andrea, Cyriaque, Hayk, Jos, Sumant, Dirk, Javier, Jorrit, Erwin, Thijs, Peter, Graciana, Eduard, Steven, Bart-Jan, Wouter, Ljubisa, Michele and Jörg.

I'm very grateful to Dr. Paul Alkemade (Kavli Institute for Nanoscience, Delft) for helping me with sample production. I want to thank Arno van Amersfoort and René Overgaww for their excellent computer & electronic support and Koos Benning and Jos Disselhorst for high-end machining. I would like to commemorate Anneke Aschoff and I want to thank Daniëlle van Raaij and Henriette van Leeuwen for their help with various papers, forms and other types of bureaucracy.

I am deeply grateful to my parents and my family members for their love and support, and I want to thank my friends and neighbors for the chats and fun we had together.

Мне хотелось бы от всего сердца поблагодарить моих родителей и родных за любовь и моральную поддержку в течение всех моих лет в Голландии. Также, я хотел бы сказать спасибо и передать привет моим милым друзьям: Александру Русанову, Хайку Арутюняну, Михаилу и Елене Кольченко, Алексею Занину, Анне Чеботаревой и Михилу де Дооду, Ивану Комиссарову, Александре Кадет и Светлане Бугаевой, Катерине Орловой и Марии Переваловой, Катерине Кремлевой, Василию Сению и Владиславу Коптелову, а так же Олесе Никольской.

List of publications

- V.V. Badikov, N.V. Kuzmin, V.B. Laptev, A.L. Malinovsky, K.V. Mitin, G.S. Nazarov, E.A. Ryabov, A.M. Seryogin and N.I. Schebetova, *A study of the optical and thermal properties of nonlinear mercury thiogallate crystals*, Quantum Electronics, **34**, p. 451 (2004).
- H.F. Schouten, N.V. Kuzmin, G. Dubois, T.D. Visser, G. Gbur, P.F.A. Alkemade, H. Blok, G.W. 't Hooft, D. Lenstra and E.R. Eliel, *Plasmon-assisted two-slit transmission: Young's experiment revisited*, Phys. Rev. Lett., **94**, p. 053901 (2005).
- N.V. Kuzmin, H.F. Schouten, G. Gbur, G.W. 't Hooft, E.R. Eliel and T.D. Visser, *Enhancement of spatial coherence by surface plasmons*, Opt. Lett., **32**, p. 445 (2007).
- N.V. Kuzmin, P.F.A. Alkemade, G.W. 't Hooft and E.R. Eliel, *Bouncing surface plasmons*, Opt. Express **15**, p. 13757 (2007).
- N.V. Kuzmin, P.F.A. Alkemade, G.W. 't Hooft and E.R. Eliel, *Phase factors in light-plasmon scattering*, in preparation.
- N.V. Kuzmin, G.W. 't Hooft and E.R. Eliel, *Sub-wavelength slit as a quarter-wave plate*, in preparation.
- N.V. Kuzmin, O.T.A. Janssen, P.F.A. Alkemade, H.P. Urbach, G.W. 't Hooft and E.R. Eliel, *Retardation effects in sub-wavelength slits in thin metal films near cut-off*, in preparation.
- N.V. Kuzmin, A.L. Tchegotareva, J.J. Renema, B.J.G. van der Meer, P.F.A. Alkemade, G.W. 't Hooft and E.R. Eliel, *Short-wavelength surface plasmons*, in preparation.

